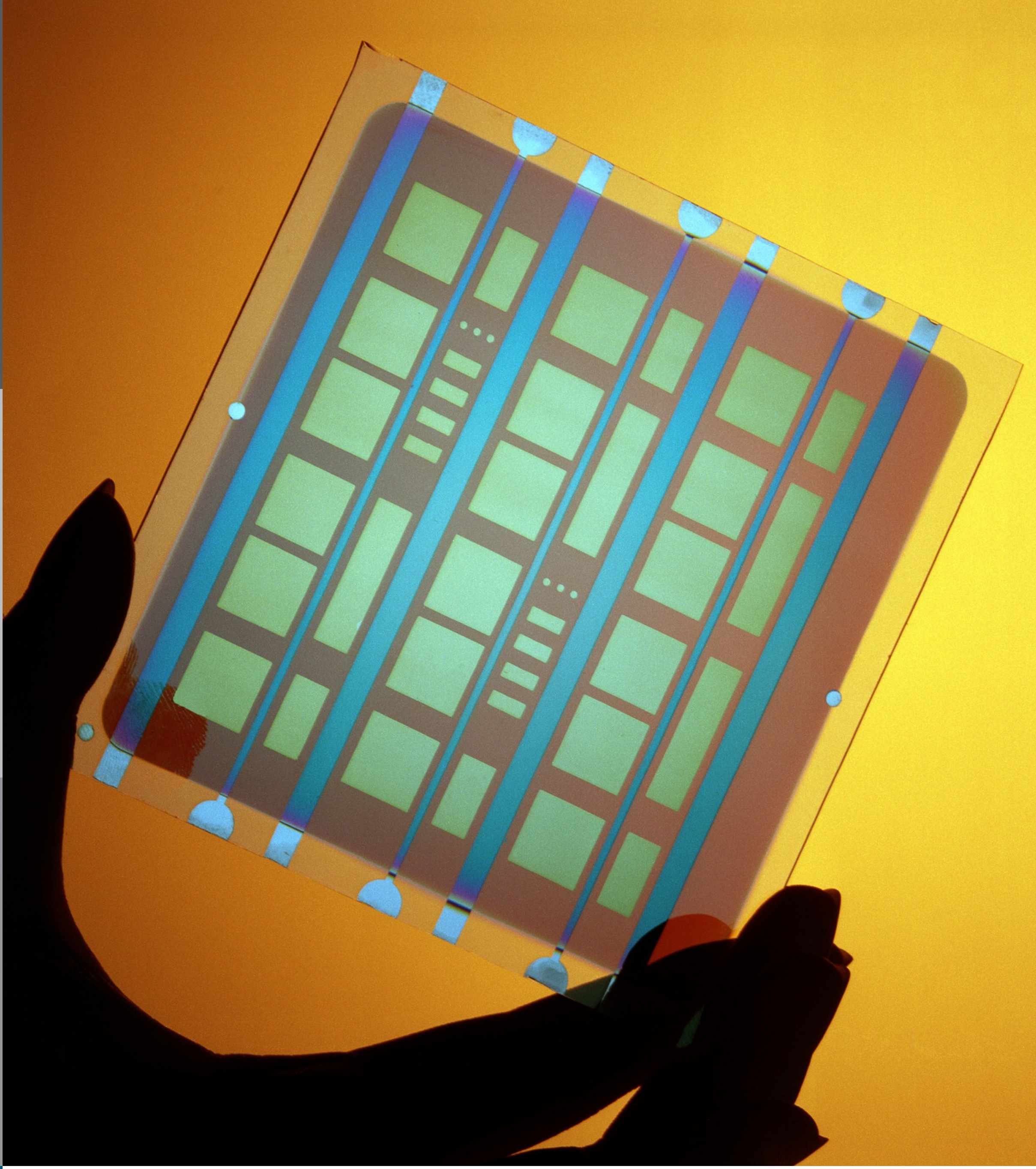

Electron Spin Resonance Investigation of Semiconductor Materials for Application in Thin-Film Silicon Solar Cells

Lihong Xiao

Mitglied der Helmholtz-Gemeinschaft

JÜLICH
FORSCHUNGSZENTRUM

Schriften des Forschungszentrums Jülich
Reihe Energie & Umwelt / Energy & Environment Band / Volume 146

Forschungszentrum Jülich GmbH
Institute for Energy and Climate Research (IEK)
Photovoltaics (IEK-5)

Electron Spin Resonance Investigation of Semiconductor Materials for Application in Thin-Film Silicon Solar Cells

Lihong Xiao

Schriften des Forschungszentrums Jülich
Reihe Energie & Umwelt / Energy & Environment Band / Volume 146

ISSN 1866-1793 ISBN 978-3-89336-805-1

Bibliographic information published by the Deutsche Nationalbibliothek.
The Deutsche Nationalbibliothek lists this publication in the Deutsche
Nationalbibliografie; detailed bibliographic data are available in the
Internet at http://dnb.d-nb.de.

Publisher and Distributor:	Forschungszentrum Jülich GmbH Zentralbibliothek 52425 Jülich Phone +49 (0) 24 61 61-53 68 · Fax +49 (0) 24 61 61-61 03 e-mail: zb-publikation@fz-juelich.de Internet: http://www.fz-juelich.de/zb
Cover Design:	Grafische Medien, Forschungszentrum Jülich GmbH
Printer:	Grafische Medien, Forschungszentrum Jülich GmbH

Schriften des Forschungszentrums Jülich
Reihe Energie & Umwelt / Energy & Environment Band / Volume 146

D 91 (Diss., TU München, 2012)

ISSN 1866-1793
ISBN 978-3-89336-805-1

CONTENT

Zusammenfassung

In der vorliegenden Arbeit wurde hydrogeniertes Silizium (Si) sowie seine Legierungen Siliziumcarbid (SiC) und Siliziumoxid (SiO$_x$) mit Hilfe der Elektronen Spin Resonanz (ESR) Methode untersucht. Die Untersuchungen umfassen Materialien mit amorpher Mikrostruktur über Mischmaterialien bis hin zu Materialien mit hochkristalliner Mikrostruktur. Die Korrelation zwischen paramagnetischen Defekte, der Mikrostruktur und den optoelektrischen Eigenschaften wurde diskutiert. Die jeweiligen Materialeingenschaften wurden mittels Spindichte (N_S), g-Wert und Linienform der ESR-Spektren, Infrarotspektroskopie (I_C^{IR}) und/oder Ramanspektrsoskopie (I_C^{RS}) sowie optischer Absorption und elektrischer Dunkelleitfähigkeit (σ_D) bestimmt.

1. Als Lichtabsorbierendes Material sollte hydrogenierten Silizium grundsätzlich eine niedrige Defektdichte und eine hohe Beständigkeit gegenüber optischer Strahlung besitzen. Die mittels ESR gemessene Spindichte (N_S) wird häufig als ein Maß für die paramagnetische Defektdichte (N_D) in einem Material verwendet. Allerdings kann die ESR – Probenvorbereitung möglicherweise Diskrepanzen zwischen N_S und N_D hervorrufen. Die hydrogenierten Siliziumschichten wurden mittels Plasma – unterstützte Gasphasenabscheidung (PECVD) hergestellt. Für die Abscheidung von dünnen Filmen hydrierten Silizium, Molybdän-Folie, Aluminiumfolie oder Aluminium-dotiertes Zinkoxid (ZnO: Al) Gläser wurden als Opfersubstraten verwendet. Die Herstellung der ESR Pulverproben wurde mit den hierfür notwendigen Verfahren durchgeführt. Die metastabilen und instabilen Effekte der Probenvorbereitung wurden hinsichtlich der Abhängigkeit vom verwendeten Substrattyp, des Einflusses des HCl-Ätzens und des atmosphärenbedingten Materialänderungen untersucht.

Die metastabilen und instabilen Effekte wurden untersucht, indem die Proben eine definierten Folge von Prozessschritten – Herstellen, Tempern, Lagerung an Atmosphäre,

Tempern – durchliefen. Es hat sich gezeigt, dass N_S nach der Atmosphärenlagerung höher ist als nach dem Tempern, insbesondere für das hochkristalline µc-Si:H Material beträgt der Unterschied ca. eine Größenordnung. Niedertemperatur ESR – Messungen bei 40 K zeigten, dass die Atmosphärenlagerung zu einen Umverteilung der Defektzustände führt. Hierdurch wurde die Bestimmung von N_S beeinflusst. Im annealten Zustand besitzen die Proben tendenziell ein niedrigeres N_S, vermutlich aufgrund des leichten *n*-Typ-Charakters undotierter a-Si:H- und µc-Si:H-Schichten. Aufgund dessen führt die ESR-Auswertung zu einer Unterbewertung der Defektdichte in hochkristallinem µc-Si:H nach Tempern. Zusammenfassend kann festgehalten werden, N_S im exponiern Zustand N_D deutlich besser wiedergibt als dass im getemperten Zustand.

2. Nominell undotierte sowie Al-dotierte µc-SiC:H Schichten wurden als transparente, leitfähige Fensterschichten mit Heißdraht-chemischer Gasphasenabscheidung (HWCVD) hergetellt. Proben mit unterschiedlichen Kritallinitäten von hochkristallin (I_C^{IR} > 90%) bis hin zu amorph (I_C^{IR} = 0%) wurden hergestellt. Hierbei wurde die Konzentration des Monomethylsilans (c_{MMS}), die Substrat – und Filament – Temperatur (T_S, T_F), der Gasdruck (p) und die Al – Dotierung (p_{TMAl}/p_{MMS}) variiert.

In dem nominell undotierten µc-SiC:H – Material wurde ein hohes N_S über einen weiten Bereich der Kristallinität beobachtet, während sich σ_D um 10 Größenordnungen bis hin zu 10^{-2} S/cm erhöht, weil das Material kristalliner wird. Die drastische Zunahme von σ_D wurde der höheren Kristallinität und einer ungewollten Donatordotierung zugeschrieben. Das ESR-Spektrum ändert sich von einer breiten merkmalslosen Resonanz bei geringen Kristallinitäten zu einer scharfen Linie mit einem Paar von ausgeprägten Satelliten in hochkristallinem *n* – Typ – µc-SiC:H. Die zentrale Resonanz liegt fest bei g = 2.003. Die zentrale Resonanz ist eng verbunden mit den paramagnetischen Zuständen von Si – und/oder C – Leerstellen (V_{Si}, V_C) bei unterschiedlichen Ladungszuständen sowie offenen Bindungen in der ungeordneten Phase des Materials. Die Hyperfeinstruktur steht verspekulieren in Verbindung mit der ungewollten Nitrogen – Dotierung.

Al – Dotierung führt zu einer Kompensation von Donatoren. Zunächst fällt σ_D auf ein Minimum bei 10^{-11} S/cm mit zunehmender Al – Dotierung bevor σ_D auf Werte bis zu 4×10^{-4} S/cm steigt. Gleichläufig sinkt N_S zunächst auf 5×10^{17} cm^{-3} bevor es auf bis zu 2×10^{19} cm^{-3} steigt. Des Weiteren führt die Al – Dotierung ebenfalls zu einer Reduzierung der Kristallinität (I_C^{IR}) des µc-SiC:H – Materials. Effektive *p* – Dotierung tritt in µc-SiC:H – Material bei höheren Al – Dotierung auf. Der Charakter und das Verhalten der ESR-Spektren in verschiedenen Arten von µc-SiC:H wurden in Bezug auf die Position des Fermi – Niveaus und der Kristallinität untersucht. Zum Beispiel zeigen die ESR-Spektren für Proben mit $I_C^{IR} \leq 20\%$ eine breite (die Peak-zu-Peak Linienbreite ist $H_{PP} \approx 30$ G), merkmallose, leicht asymmetrische Linie bei $g \approx 2.01$. Diese kann spekulativ auf einen Löcher – Einfang in den Valenzbandausläufern zurückgeführt werden. Für höher und hoch kristalline *p* – Typ – µc-SiC:H Proben, das ESR-Signal ist im Bereich $g \approx 2.003$ mit $H_{PP} \approx 6 – 10$ G, dies wird paramagnetischen Si – und freien C – Bindungen zu geschrieben.

3. Dotiertes mikrokristallines Siliziumoxid (µc-SiO$_x$:H) wurde zur Anwendung als Zwischenreflektor und als Fensterschicht entwickelt. Diese Untersuchungen haben gezeigt, dass es sich hierbei um ein Mischphasenmaterial handelt. Die eine Phase besteht aus mikrokristallinem Silizium und die andere aus amorphen Siliziumoxid (a-SiO$_x$:H). Durch Variation der PH$_3$ – Dotierung, des Kohlendioxidfusses, des Wasserstoffflusses, des Silanflusses und der Saatschicht wurde die Struktur und die Legierungszusammensetzung im Bereich zwischen hochkristallinem µc-Si:H und amorphem a-SiO$_x$:H gevariiert.

In intrinsischem µc-SiO$_x$:H – Material wurde eine starke Reduzierung von σ_D im Bereich 10^{-3} S/cm bis 10^{-12} S/cm und eine Steigerung von N_S von 10^{17} cm^{-3} bis 3×10^{19} cm^{-3} mit einer Verringerung der Kristallinität beobachtet. Für Phosphin-dotierte Proben ändert sich σ_D von 10^1 S/cm auf 10^{-12} S/ cm, wenn I_C^{RS} abnimmt. Die ESR – Spektren von intrinsischem Material bestehen aus einer einzigen Linie ohne besondere Merkmale, mit *g*-Werten im Bereich von 2.0043 bis 2.005 je nach Struktur und Phasenzusammensetzung. Die vorherrschenden Defekte werden freien Silizium-Bindungen (Si-dbs) in unterschiedlichen Umgebungen zugewiesen. Die ESR – Spektren von *n*-dotiertem Material haben ein breiteres Spektrum von *g*-Werten von 1.998 bis 2.0043. Diese starke Variation liegt an der starken Schwankungen des Fermi-Niveaus über dem gesamten Kristallinitätsbereich. In µc-Si:H, die dominante Resonanz ändert sich von der Elektronen (CE)-Resonanz, aber in a-SiO$_x$:H, die dominante Resonanz ist von Si-dbs-Resonanz in der amorph Matrix.

Abstract

In the present work, hydrogenated silicon (Si) and its alloys silicon carbide (SiC) and silicon oxide (SiO_x) have been investigated using electron spin resonance (ESR). The microstructure of these materials ranges from highly crystalline to amorphous. The correlation between the paramagnetic defects, microstructure, optical and electrical properties has been discussed. Correspondingly, these properties were characterized by the spin density (N_S), *g*-value and the lineshape of ESR spectra, Infrared (I_C^{IR}) and/or Raman crystallinity (I_C^{RS}) as well as optical absorption and electrical dark conductivity (σ_D).

1. As the light absorber, Si layers essentially should have low defect density and good stability against light exposure. The spin density (N_S) measured by ESR is often used as a measure for the paramagnetic defect density (N_D) in the material. However, ESR sample preparation procedures can potentially cause discrepancy between N_S and N_D. Using Mo – foil, Al – foil and ZnO:Al – covered glass as sacrificial substrates, µc-Si:H and a-Si:H films were deposited by plasma-enhanced chemical vapor deposition (PECVD), and ESR powder samples have been prepared with corresponding procedures. Possible preparation – related metastability and instability effects have been investigated in terms of substrate dependence, HCl – etching and atmosphere exposure.

A sequence of 'preparation – annealing – air-exposure – annealing' has been designed to investigate the metastability and instability effects. N_S after post-preparation air exposure is higher than in the annealed states, especially for the highly crystalline µc-Si:H material the discrepancy reached one order of magnitude. Low temperature ESR measurements at 40 K indicated that atmospheric exposure leads to a redistribution of the defect states which in turn influence the evaluated N_S. In annealed conditions the samples tend to have lower N_S presumably due to slight *n*-type character of undoped a-Si:H and µc-Si:H. Therefore ESR evaluation leads to an underestimation of N_D in the annealed states of highly crystalline µc-Si:H. It has been concluded that N_S in the exposed states represents N_D more adequately than in the annealed states.

2. As the transparent conductive window layer, nominally undoped and Al-doped µc-SiC:H thin films were prepared by hot-wire chemical vapor deposition (HWCVD). Samples with a wide range of crystallinity from highly crystalline ($I_C^{IR} > 90\%$) to amorphous ($I_C^{IR} = 0\%$) have been prepared with variation of the Monomethylsilane concentration (c_{MMS}), the substrate and filament temperature (T_S, T_F), the gas pressure (p) and the Al-doping concentration (p_{TMAl}/p_{MMS}).

In the nominally undoped µc-SiC:H material, a high N_S is observed over a wide range of crystallinity, whereas σ_D increases by 10 orders of magnitude up to 10^{-2} S/cm as the material becomes more crystalline. The dramatic increase of σ_D has been attributed to both the higher material crystallinity and unintentional donor doping. The ESR spectrum changes from a broad featureless resonance in the low crystallinity material to a sharp line with a pair of distinct satellites in highly crystalline *n*-type µc-SiC:H. The resonance center is constant at $g = 2.003$. The central resonance is associated with the paramagnetic states of Si – and/or C – vacancies (V_{Si}, V_C) at different charge states and dangling bonds (dbs) in disordered phases, and the observed hyperfine structure is speculated to be related to the unintentionally doped nitrogen.

Al-doping leads to a compensation of donors. σ_D firstly dropped to the minimum of 10^{-11} S/cm before increasing up to 4×10^{-4} S/cm, while N_S decreased to 5×10^{17} cm^{-3} and then increased up to 2×10^{19} cm^{-3}. Meanwhile, Al-doping also results in a loss of crystallinity (I_C^{IR}) of µc-SiC:H material. Effective *p*-type doping occurs in µc-SiC:H material at higher Al-doping. The nature and behavior of the ESR spectra in different types of µc-SiC:H are investigated with respect to the Fermi level position and crystallinity. For $I_C^{IR} \leq 20\%$ the ESR spectrum is a broad (peak-to-peak linewidth $H_{PP} \approx 30$ G) featureless slightly asymmetric line at $g \approx 2.01$, and by analogy it is speculatively associated with holes trapped in the valence band tail. For moderately and highly crystalline *p*-type µc-SiC:H, the ESR signal is in the region of $g \approx 2.003$ with $H_{PP} \approx$ 6 - 10 G, and it is attributed to the paramagnetic Si – and C – dangling bonds.

3. As both the window and the intermediate reflector layer, µc-SiO$_x$:H, which is found to be a phase mixture of µc-Si:H and a-SiO$_x$:H, has been prepared by PECVD. With variation of the

PH_3-doping, gas flow of CO_2, H_2 and SiH_4, and the seed layers, the structure and alloy composition of the material were varied in the range of highly crystalline μc-Si:H to a-SiO_x:H.

In intrinsic μc-SiO_x:H material, a strong reduction of σ_D from 10^{-3} S/cm to 10^{-12} S/cm and an increase of N_S from 10^{17} cm^{-3} to 3×10^{19} cm^{-3} is observed as the film crystallinity (I_C^{RS}) decreases. In PH_3-doped samples, σ_D changes from 10^{1} S/cm to 10^{-12} S/cm as I_C^{RS} decreases. ESR spectra of intrinsic material consist of a single featureless line with g-values in the range of 2.0043…2.005 depending on the structure and alloying, and the dominant defects are assigned to silicon dangling bonds (Si-dbs) in different environment. ESR spectra of n-type material exhibit a broader range of g-values of 1.998…2.0043 due to strong variations of the Fermi level over the entire crystallinity range, and the dominant resonance changes from the conduction electron (CE) – resonance in μc-Si:H to Si-dbs in a-SiO_x:H matrix.

Chapter 1: Introduction

Solar cells, which convert sunlight into electricity, are increasingly applied for power supply. The first modern cell was developed by Daryl Chapin and his co-workers from Bell Labs by using a diffused crystalline silicon (c-Si) $p - n$ junction [Chapin1954]. It had a considerable conversion efficiency of η = 6%. The predicted maximum solar conversion efficiency (η_{max}) – the 'Shockley – Queisser – Limit' [Shockley1961] is around 33.7% assuming a single $p - n$ junction with a band gap of E_g = 1.1 eV (e.g. c-Si). Nowadays, the efficiency for c-Si cells in production has been improved to the state-of-the-art level of $\eta_{max} = 24.2\%$ by Sunpower [Cousins2010], and close to $\eta_{max} = 25.0 \pm 0.5\%$ in the laboratory [Green2011].

One of the main drawbacks of c-Si cells is the too high consumption of the Si raw material. It has been reported that a-Si:H and µc-Si:H have a larger optical absorption coefficient than c-Si in the blue region, and µc-Si:H has comparable absorption coefficient to c-Si in the red and infrared region. Combining the use of thin-film hydrogenated amorphous and microcrystalline silicon (a-Si:H and µc-Si:H) solar cells offer more efficient use of the Si raw material with a reduction of the cell thickness. The technology has been developed to improve the light trapping, to reduce process temperatures for the use of low-cost substrates, to build up multi-junction structures for better use of the solar spectrum, and to develop large-area fabrication and integration into modules.

One of the key research topics of thin-film Si is the understanding of their electronic properties. Defects and impurities which have localized electronic states within the band gap are critical limiting factors. These electronic defects act as recombination centers for photo – generated charge carriers, suppress doping by acting as traps and generally lower the performance of optoelectronic devices. Therefore, the nature of defects, their formation mechanisms and their influences on the electronic transport in a-Si:H, µc-Si:H and Si alloys are of importance for thin-film Si photovoltaics.

For the investigation of electronic defect, electron spin resonance (ESR) is one of the powerful tools. Since the first observation of ESR signal in 1945 in a $CuCl_2 \cdot 2H_2O$ sample [Zavoisky1945], the ESR technique has been continuously developed and widely used to characterize paramagnetic defects in semiconductors. Conventional ESR, which uses a continuous microwave source, measures the net absorption of electromagnetic waves by electrons in paramagnetic states in the microwave frequency domain. In combination with other supplementary experimental techniques (e.g. electrical, optical and structural measurements), more and more advanced ESR techniques have been developed.

ESR was first used to investigate the paramagnetic defects in Si/SiO_x systems like silica glasses since the 1950s [Combrisson1954]. From then on, several ESR – active centers, like E' centers [Weeks1956; Carlos1984; Takahashi1987; Awazu1993; Lenahan1998; Barklie2001; Buscarino2007; Jivănescu2010], P_b centers [Nishi1971; Caplan1979; Lenahan1982; Stesmans1990; Stathis1991; Cartier1995; Stesmans1998; Stesmans2008; Jivănescu2010; Keunen2011], *S* centers [Stesmans1996; Mizuguchi1998; Karna1999; Stesmans2002] and so on, were described as Si-dangling-bond-like (Si-db-like) defects with different environments.

The ESR investigation of SiC started with the investigation of N-, P-, B- and Al-doped SiC single crystals [Wieringen1958]. Three paramagnetic resonances were observed and attributed to the hyperfine structure caused by a nucleus with nuclear spin $I = 1$. In *n*- and *p*-type SiC, the central resonance was found at $g = 2.003 \pm 0.001$ and $g = 2.004 \pm 0.001$, respectively. Referring to extensive ESR investigations of 3C-, 4H- and 6H-SiC cystals, the dominant paramagnetic defects are believed to be dangling bonds that are related to Si- and C-vacancies [Itoh1990; Schneider1993; Sörman2000; Son2010].

In the 1980s, ESR was first applied to hydrogenated silicon, since then various ESR signals have been identified in a-Si:H [Street1981; Stutzmann1983; Joannopoulos1984; Fehr2011] and μc-Si:H [Hasegawa1983; Finger1994; Lips2003]. For intrinsic, *n*- and *p*-type doped a-Si:H, signals at $g = 2.0055$, 2.0043 and 2.0100 – 2.0138 have been observed and attributed to dangling bonds (dbs), electrons localized at the conduction band tail and holes localized at the valence band tail, respectively. Intrinsic μc-Si:H shows an asymmetric signal with contributions at $g = 2.0043$ (db1) and $g = 2.0052$ (db2), which are suggested to originate from two independent states located in different microscopic environments [Lips2003]. For *n*-type μc-Si:H, a third resonance at $g = 1.996 - 1.998$ was observed. It is often referred to as conduction electron (CE) – resonance and is arguably attributed to electrons in the conduction band [Hasegawa1983; Finger1994] and/or shallow localized states in the conduction band tail [Müller1999; Kanschat2000].

This work provides a comprehensive ESR study of a-Si:H and μc-Si:H, and the two Si alloys – microcrystalline silicon carbide (μc-SiC:H) and silicon oxide (μc-SiO$_x$:H) thin films developed for application in thin-film Si solar cells. The thesis is organized as follows:

- Chapter 1: Introduction of the ESR research background relevant to a-Si:H, μc-Si:H, μc-SiC:H and μc-SiO$_x$:H.
- Chapter 2: Introduction of background knowledge. Starting with an introduction into the working principles of thin-film Si solar cells, the motivation for the application of a-Si:H and μc-Si:H as absorber layers, μc-SiC:H as window layer, μc-SiO$_x$:H as both the window layer and intermediate reflector layer for is presented. The principles of the ESR technique are introduced.
- Chapter 3: All characterization methods involved in this thesis are described.
- Chapter 4: Results about the influences of glass substrates on the ESR measurements of film samples are presented – Primary exposure to an H-plasma induces ESR signals on the glass surface and influences the interpretation of ESR signal from the film material, especially for very thin films with thickness below 100 nm, which were deposited on these glass substrates.
- Chapter 5: Results and discussion about the ESR investigation of intrinsic a-Si:H and μc-Si:H powder samples – Preparation-related metastability and instability effects are investigated. Samples of different structural composition from highly crystalline μc-Si:H to a-Si:H deposited by PECVD on Mo-foil, Al-foil and ZnO-covered glass substrates are studied by a preparation – annealing – air exposure – annealing sequence.
- Chapter 6: Results and discussion about the ESR investigation of μc-SiC:H powder and films – Samples were prepared by HWCVD, deposition parameters like the monomethylsilane concentration (c_{MMS}), substrate and filament temperature (T_S, T_F), process pressure (p) and the Al-doping ratio (p_{TMAl}/p_{MMS}) are varied. Correlations between structural, electrical, optical and ESR properties are discussed in both *n*- and *p*-type μc-SiC:H films.

- Chapter 7: Results and discussion about the ESR investigation of μc-SiO_x:H powder and films – Influence of the oxygen incorporation, PH_3-doping, H_2 – dilution ratio and seed layer on the structural, electrical, optical and ESR properties are investigated.

At the end of each chapter, a summary and conclusions are given.

Chapter 2: Fundamentals

This chapter starts with a brief introduction of thin-film Si solar cells, followed by a motivation of the material selection for each layer (e.g. a-Si:H and μc-Si:H as absorber layers, μc-SiC:H as the window layer, and μc-SiO$_x$:H as both the window and intermediate reflector layer). Then, some essential theoretical background e.g. the electronic density of states, the nature of bands and band tails, the conduction mechanism, and the charge states of defects, is addressed. Finally, the basics of continuous wave (cw-) ESR are introduced.

2.1 Thin-film Si for solar cell applications

A thin-film Si solar cell is made by growing Si and some other photovoltaic materials in the form of films onto a given substrate. The layer thickness ranges from a few nm to a few μm. In this section, the configuration and some basics of thin-film Si solar cells are briefly described. More details are available in the literature, e.g. [Nelson2003; Poortmans2006].

2.1.1 Thin-film Si solar cell configuration

For a single junction solar cell, two types of device structures are commonly used. According to the layer deposition sequence (as indicated by the black filled arrows in Fig. 2.1(a) and (b)), they are called (a) *p-i-n* and (b) *n-i-p* solar cells, also named as "superstrate" and "substrate" type cells. The term "superstrate" refers to a solar cell configuration where the glass substrate is not only used as supporting structure but also as window for the illumination and as part of the encapsulation. During operation the glass is "above" the actual solar cell.

As the intrinsic layer (*i*-layer, it is used to absorb the incoming sunlight and supply photo-generated charge carriers of electrons and holes), both a-Si:H and μc-Si:H can be used. In thin-film Si single junction solar cells, typical thicknesses of the intrinsic a-Si:H and μc-Si:H layers are ~ 300 nm and 1 – 1.5 μm, respectively.

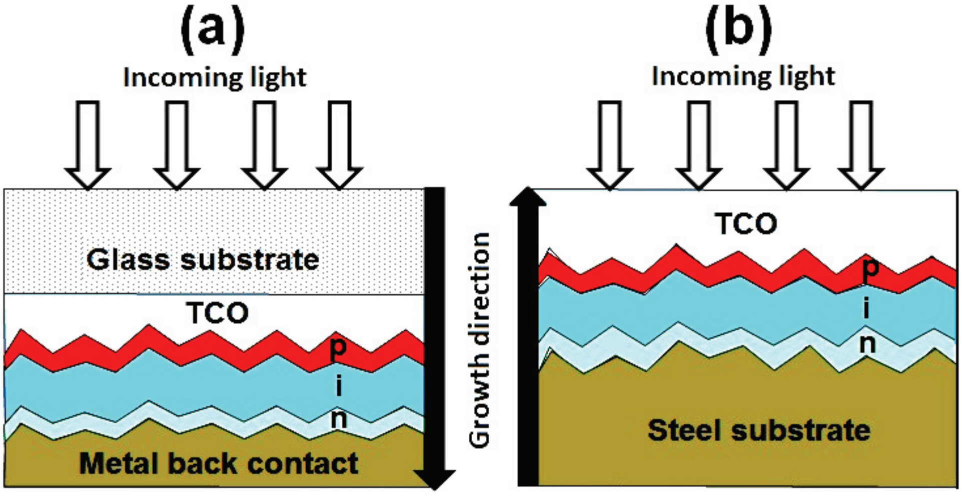

Figure 2.1 *Single junction solar cell in p-i-n (a) and n-i-p (b) configuration.*

Si atom has 4 relatively weakly bound (valence) electrons which bond to adjacent atoms, therefore replacing a Si atom with an atom that has either 3 or 5 valence electrons will then produce electron deficiency (a hole) or one excess electron. These excess electrons or holes are easily activated and at room temperature provide majority of free charge carriers in *n*- or *p*-type semiconductors respectively. The *n*-layer is an *n*-type doped layer, for which atoms with 5 valence electrons (e.g. phosphorus) are incorporated into the material and excess electrons are achieved. And the *p*-layer is a *p*-type doped layer, for which atoms with 3 valence electrons (e.g. boron) are incorporated into the material and excess holes are achieved. The *n*- and *p*- layers set up an internal electric field for collecting the photogenerated charge carriers in the *i*-layer.

Two electrodes to the cell are required to transfer the generated current to an external circuit. Being used as front electrode, material is required for high light transparency to let light go to the absorber layer and high conductivity to transfer electrical current to the external circuit. Transparent conductive films (most often oxide, therefore shortly named as TCO), such as aluminum doped zinc oxide (ZnO:Al), satisfies both the optical and electrical requirements. Metals, such as silver or steel, are used as back electrode. In order to increase the sunlight trapping without increasing the thickness of the *i*-layer, both the front and back contacts are textured in the way as is shown in Fig. 2.1. Further information about the design, preparation and optimization of metallic contacts can be found elsewhere [Morris1990; Kluth2001; Owen2011].

Different band gaps of absorber materials can be used for multijunction-structured cells. Typically, a-Si:H and µc-Si:H can advantageously be stacked, creating a *tandem cell* as shown in Fig. 2.2, which enhances utilization of the solar spectrum and reduces the losses by thermalization. Meanwhile, the stability against light soaking is improved by reducing the thickness of a-Si:H layer comparing with that of a-Si:H single junction cell for the same energy output. The most serious drawback of a-Si:H regarding its use in solar cells is the light-induced degradation – the "Staebler-Wronski-Effect" (SWE, [Staebler1977]), which is the light-induced increase of the density of dangling bonds and therefore a metastable decrease in the dark conductivity and photoconductivity of intrinsic a-Si:H. The solar cell output performance deteriorates with the light-soaking time.

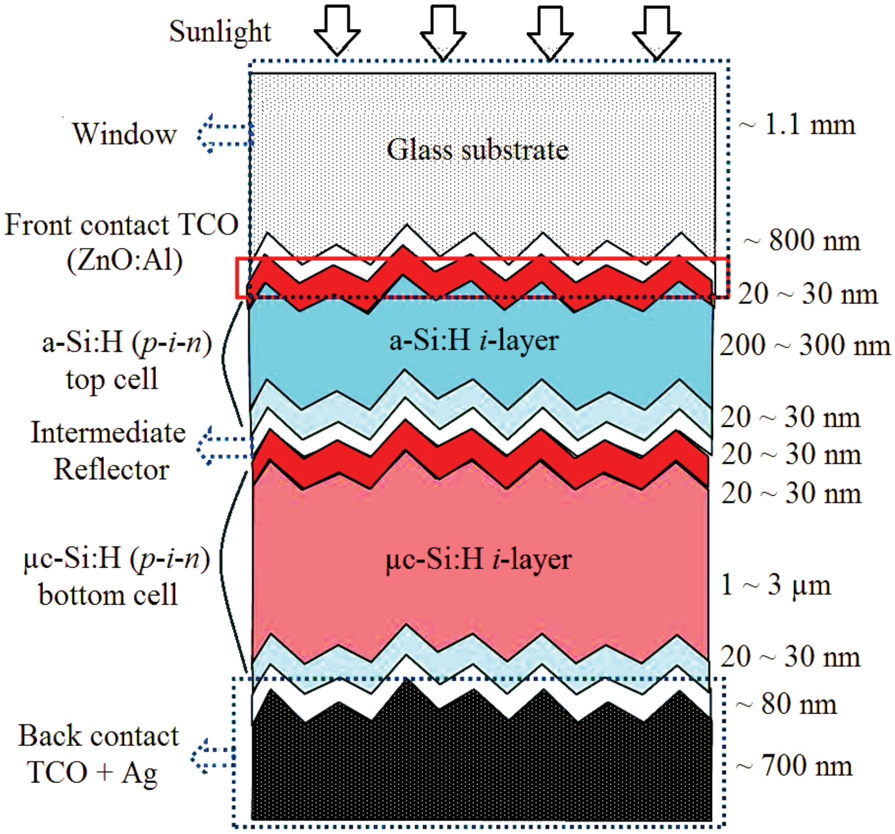

Figure 2.2 *Schematic diagram of an a-Si:H/µc-Si:H tandem cell on a glass substrate. The materials for each layer are noted on the left, and the corresponding thicknesses on the right.*

2.1.2 Operation principles of thin-film Si solar cells

The working principle of thin-film Si solar cells is essentially the same as the traditional c-Si solar cells; it is based on the *photovoltaic effect*. The basic processes are:

1) Sunlight falls on the cell and charge carriers (electrons and holes) are generated due to the absorption of photons in the absorber layer;

2) Photo-generated charge carriers are subsequently separated by the internal electric field in the junction, collected at the terminals and transported out to the external circuit.

Fig. 2.3 shows the schematic band diagrams of a *p*-*n* junction for conventional c-Si diffusion cells (Fig. 2.3(a)) and a *p*-*i*-*n* junction for thin-film Si drift cells (Fig. 2.3(b)).

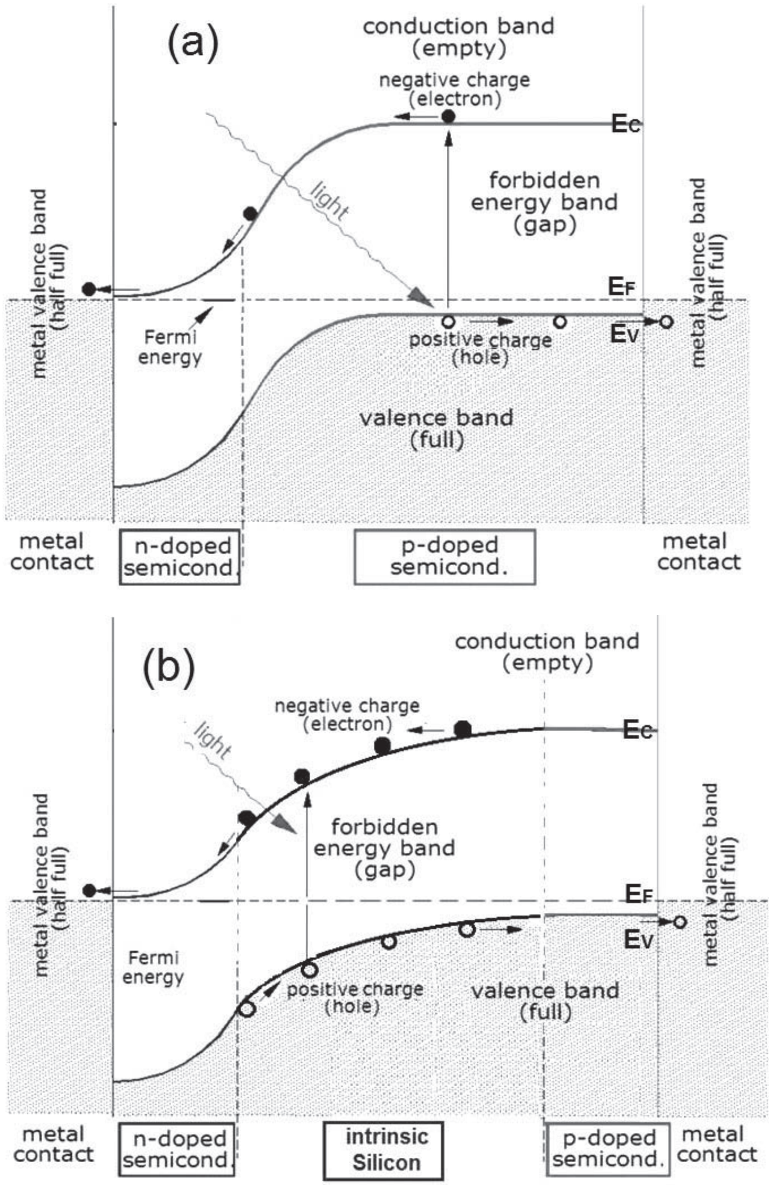

Figure 2.3 *Energy band diagrams of a p-n junction for c-Si cells (a) and a p-i-n junction for thin-film Si cells (b).* E_F, E_C *and* E_V *denote the Fermi level, the bottom of the conduction band and the top of the valence band (Diagram courtesy of GianniG46, Free Software Foundation).*

The tranditional c-Si solar cell is a homojunction device. A lightly-doped *p*-type c-Si wafer with an acceptor (typically B or Al) concentration of $N_A = 10^{15} – 10^{16}$ cm^{-3} is used as both the sunlight absorber layer and substrate. A heavily-doped *n*-type window/emitter layer with a donor (typically P) concentration of $N_D = 10^{19} – 10^{20}$ cm^{-3} is diffused on the *p*-type c-Si wafer base. The Fermi level of the *n*-type (*p*-type) side locates near the conduction (valence) band edge so that donor-released electrons will diffuse into the *p*-type side to occupy lower energy states there, until the exposed space charge (ionized donors in the *n*-type region, and ionized acceptors in the *p*-type) produces an electric field ($E_{internal}$) at the metallurgical interface between the *n*- and *p*-type regions, and $E_{internal}$ is large enough to prevent further diffusion.

Often few carriers are collected from the heavily doped *n*-type region. For those charge carriers that are not separated from each other in a relatively short time, they will be annihilated in an electronic process which is called *recombination* and thus will not contribute to the photovoltaic conversion. Therefore, the *n*-type emitter layer is usually kept very thin. The long diffusion length of electrons in the *p*-type region is a consequence of the long electron lifetime due to low doping and of the higher mobility of electrons compared with holes.

When electrons and holes carriers are generated by photon absorption in the depletion region, which lies mostly in the lightly doped *p*-type region, $E_{internal}$ is extremely effective at separating the photogenerated electron-hole pairs. Through the electric field – assisted drift, electrons and holes transport through the *n*- and *p*-layers, and then are collected by electrodes.

However, due to the high defect density and thus the short diffusion length of charge carriers in the doped a-Si:H and µc-Si:H films, the *p*-*n* structure used in c-Si solar cells is not applicable in disordered thin-film Si solar cells. Extrinsic charge carriers introduced by *p*- and *n*-type doping are always accompanied by two or three orders of magnitude larger concentrations of charged defects in doped a-Si:H compared to intrinsic a-Si:H. The cumulative effect of defect-induced short carrier lifetime and a low carrier mobility (e.g. electron mobility: $\mu_e \approx 1000$ cm^2/V·s in c-Si, $\mu_e \approx 0.1–1$ cm^2/V·s in a-Si:H) due to structural disorder reduces the diffusion length (*l*, the average length a carrier moves between generation and recombination) of the photo-generated carriers (e.g. $l = 100 – 300$ µm in c-Si, $l = 0.1 – 0.3$ µm in intrinsic a-Si:H, and even lower in doped a-Si:H.). Meanwhile, the band bending introduced by the rather different Fermi-level position of the *n*- and *p*-type doped layers provides a built-in field in the a-Si:H *i*-layer, which promotes drift and extraction of the charge carriers.

In the *p-i-n* junctions, as is shown in Fig. 2.3(b), the region of $E_{internal}$ is extended by inserting an intrinsic silicon layer (*i*-layer) between the *p*-type and the *n*-type layers. The *i*-layer behaves like a capacitor and it stretches the electric field formed by the *p-n* junction. Under $E_{internal}$, holes will drift to the *p*-layer and electrons to the *n*-layer in order to reduce their electrostatic potential energy. This separation of charge carriers builds up a voltage between the *p*- and *n*-layers. This voltage is called photovoltage under illumination. If the *p*- and *n*-layers are connected through the electrodes by an external circuit, a photocurrent (also called 'drift current') is generated.

2.2 Material selection for thin-film Si solar cells

Based on the configuration of an a-Si:H/μc-Si:H tandem cell (as it is shown in Fig. 2.2), in this section, requirements and the material selection for the absorber layer, the window layer and intermediate layer are discussed in detail.

2.2.1 a-Si:H and μc-Si:H as the absorber layers in thin-film Si solar cells

Fig. 2.4(a) and (b) illustrate the atomic structure of c-Si and a-Si:H. In c-Si, each Si atom is covalently bound to four neighboring Si atoms with the same bond-length and bond-angle. The crystal lattice can be produced periodically by duplicating the fourfold coordinated unit and stacking the duplicates next to each other.

In a-Si:H, there is a similarity in atomic configuration on a local atomic scale, where most Si atoms have covalent bonds with four neighbors. The large deviations in bond-angles and bond-lengths between the neighboring atoms in a-Si:H result in the so-called weak or strained bonds, which can easily break and form defects in the atomic network. Hydrogen passivation reduces the dangling bond density from the magnitude of 10^{20} cm^{-3} in unhydrogenated amorphous silicon (a-Si) [Thomas1978] to 10^{15} – 10^{17} cm^{-3} in hydrogenated amorphous silicon (a-Si:H) [Knights1979; Astakhov2009]. The decrease of defect density favors the excess carrier transport by decreasing recombination. Meanwhile, the H-incorporation allows the material to be doped with donors and/or acceptors.

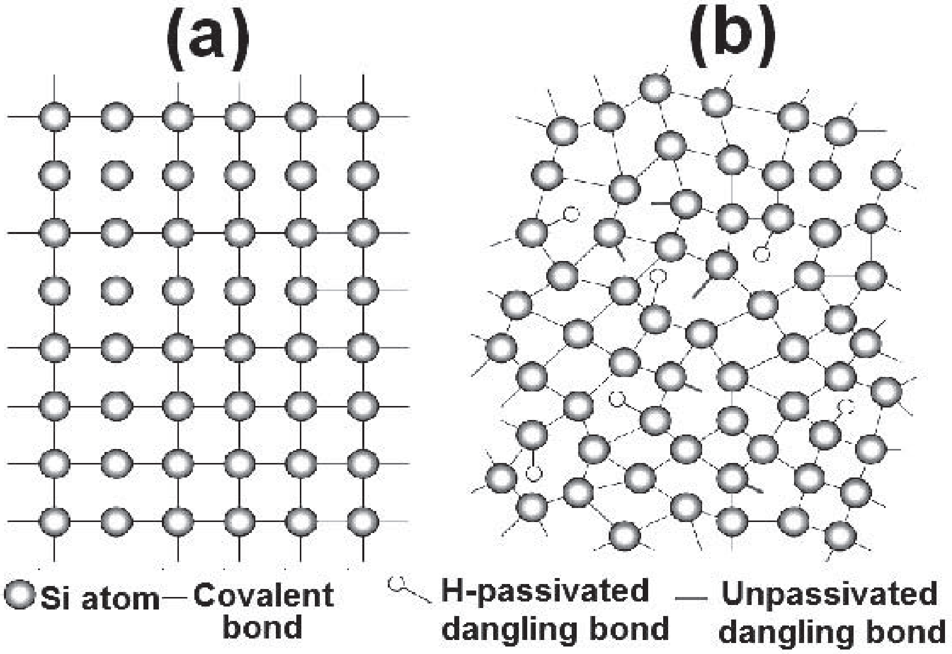

Figure 2.4 *Schematic representation for the atomic structure of c-Si (a) and a-Si:H (b).*

Since a-Si:H has an optical bandgap of about 1.6 ~ 1.9 eV, it sufficiently absorbs light with high photon energies, while the absorption for light in the near-infrared region is weak. The most serious drawback of a-Si:H regarding its use in solar cells is the Staebler-Wronski-Effect, which has been correlated with the creation of dangling bond defects under illumination. These light-induced defects in a-Si:H lead to an increase of the carrier recombination and therefore result in the reduction of the sunlight-to-electricity conversion efficiency. Depending on the material quality and device design, the cell efficiency drops by 10 – 30% after illumination under AM1.5 for 1000 h [Nelson2003].

Microcrystalline silicon which can be manufactured by the same technology (PECVD, HWCVD etc.) as a-Si:H shows higher sensitivity in the red and infrared part of the solar spectrum. The combined use of a-Si:H and μc-Si:H in a tandem solar cell results in better utilization of sunlight radiation and therefore higher energy conversion efficiency than an a-Si:H or μc-Si:H single junctions alone.

However it should be noted that µc-Si:H is more sensitive to post-deposition atmospheric effects than a-Si:H, such as the atmospheric gas adsorption and oxidation [Tanielian1980; Tanielian1982; Vepřek1983; Smirnov2004; Yilmaz2010]. It was reported that the reversible adsorption process results in a decrease of dark conductivity by up to five orders of magnitude, an increase of the activation energy, as well as an increase of the electron spin density. The irreversible oxidation effect was associated with the oxidation process mainly at the grain boundaries.

2.2.2 µc-SiC:H as the window layer in thin-film Si solar cells

Before reaching the absorber layer, light goes through the transparent glass substrate, the front TCO (transparent conductive oxides) layer and one doped layer, which together make the *window layer*. The following requirements should be met for window layer materials:

- High transparency, which means a wide optical bandgap;
- Sufficient electrical conductivity for reduced series resistance;
- High crystallinity to favor the subsequent film growth for application in µc-Si:H solar cells;
- Good anti-reflection and light scattering properties.

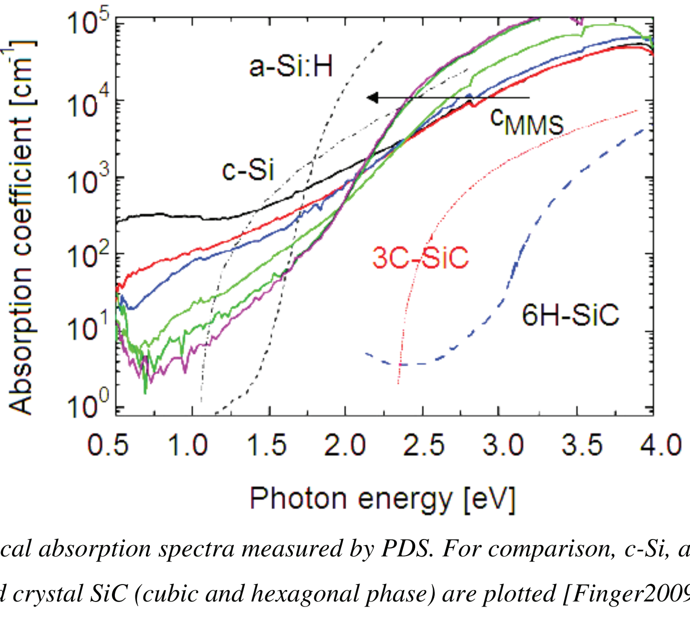

Figure 2.5 *Optical absorption spectra measured by PDS. For comparison, c-Si, a-Si:H, a series of µc-SiC:H and crystal SiC (cubic and hexagonal phase) are plotted [Finger2009].*

In Fig. 2.5, one can see that compared to c-Si and a-Si:H, SiC has a much wider optical bandgap. For crystals, the optical bandgap for c-Si, 6H(α) – SiC, and 3C(β) – SiC are 1.05, 3.05 and 2.36 eV, respectively. For a-Si:H and μc-SiC:H material, due to the disordered structure, the bandgap could not be extracted directly. Instead, E_{04} (the photon energy at which the absorption coefficient is 10^4 cm^{-1}) is used as the optical bandgap. For μc-SiC:H, E_{04} varies between 2.2 to 3.2 eV, which obviously is larger than that of a-Si:H.

Moreover, for μc-SiC:H, a high electrical conductivity could be obtained by *n*- and *p*-type doping. μc-SiC:H prepared by the Hot-wire CVD technique was unintentionally *n*-type doped. Also a high content of oxygen (10^{19} – 10^{20} cm^{-3}) and nitrogen (10^{19} cm^{-3}) were found. The dark conductivity (σ_D) covers a wide range of 10^{-12} – 10^{-1} S/cm as the material varies from amorphous to highly crystalline [Finger2009]. Material with high crystallinity and high conductivity has successfully been applied in *n-i-p* μc-Si:H solar cell with a solar cell efficiency $\eta = 9.1\%$ [Huang2007; Huang2008].

For the application in a-Si:H *p-i-n* single junction solar cells, or in a-Si:H/μc-Si:H tandem cells, SiC is desired to be *p*-type doped, such as with Al. Material preparation and optimization have been achieved by a few groups [Miyajima2006; Chen2010(1)]. Application of *p*-type μc-SiC:H in solar cells is quite promising.

2.2.3 μc-SiO$_x$:H as both the window and intermediate reflector layer in thin-film Si solar cells

The concept of thin-film Si tandem cells, which combines an a-Si:H top and a μc-Si:H bottom cell, offers both the potential for high efficiency and low fabrication costs. To reduce the effect of light-induced degradation on the cell performance and, therefore, to further improve the cell stability, it is very important to keep the thickness of the a-Si:H top cell as low as possible. One of the widely used approaches is the introduction of an intermediate reflector layer (IRL) between top and bottom cells.

The intermediate reflector has to fulfill the following requirements:

- To reflect the shorter wavelength light back to the top a-Si:H cell, and thus to increase its photocurrent for a reduced thickness – This requires the IRL material to have a large difference of the refractive index (n) compared to the cell material;

- To let longer wavelength light go through and reach the bottom μc-Si:H cell, and thus to use a broader solar spectrum – This requires the IRL material to have a big optical bandgap;
- To conduct the electrical current between the top and bottom cells – This requires the IRL material to have sufficient electrical conductivity (σ);
- To serve as the nucleation layer for the subsequent growth especially in case of microcrystalline layers– This requires the IRL material to have high crystallinity;
- Low defect density would be desirable for the electronic transport processes.

Microcrystalline silicon suboxide (μc-SiO$_x$:H), which is a phase mixture of μc-Si:H crystallites in a-SiO$_x$:H ($x = 0 – 2$), has been chosen as IRL with the following advantages:

- Tunable refractive index from $n_{\mu\text{c-Si:H}} = 3.8$ to $n_{\text{SiO2}} = 1.5$. When the light comes through the top cell to the μc-SiO$_x$:H layer, the reflection coefficient can be approximated by:

$$R = (\frac{n_{Si} - n_{SiOx}}{n_{Si} + n_{SiOx}})^2$$

For higher reflection, lower $n_{\text{SiO}x}$ is required, which means higher oxygen content.

- Tunable optical band gap from $E_{\mu\text{c-Si:H}} \approx 1.1$ eV to $E_{\text{SiO2}}.= 8.9$ eV. The μc-SiO$_x$:H material prepared in the course of this thesis has an optical bandgap between 1.9 – 3.2 eV.
- Tunable microstructure between highly crystalline μc-Si:H and a-SiO$_x$:H.
- The electrical conductivity for the undoped μc-SiO$_x$:H could be varied between that of highly crystalline μc-Si:H (10^{-3} S/cm) and a-SiO$_x$:H ($10^{-12} – 10^{-6}$ S/cm).
- The deposition of μc-SiO$_x$:H layer by PECVD is compatible to thin-film Si solar cells.

Moreover, μc-SiO$_x$:H is also a potential candidate for the use as a window layer due to its combination of high electrical conductivity, tunable crystallinity, and a wide optical bandgap [Sritharathikhun2009; Smirnov2010].

2.3 Fundamental electronic properties of disordered Si

This section starts with a brief description of the density of electronic states in disordered semiconductors. Then features of the extended and localized states and relevant electronic conduction mechanisms are addressed. At last, the substitutional *n*- and *p*-type doping mechanism is introduced.

2.3.1 The electronic density of states (DOS) in disordered semiconductors

DOS, which is denoted as $N(E)$ with the unit of eV^{-1}•cm^{-3}, describes the number of states that are available to be occupied by electrons or holes per unit volume and per unit energy. Then the total number ($N_{total}(E)$) of electronic states per unit volume in an energy band with energies E_1 (bottom of band) and E_2 (top of band) can be determined as follows:

$$N_{total}(E) = \int_{E_1}^{E_2} N(E)dE$$

The fundamental difference between an insulator and a conductor, for example, is that in insulator the DOS at the Fermi energy is zero, in conductor it is non – zero. For semiconductors, at zero temperature, Fermi energy is the boundary of the electron-occupied and unoccupied states.

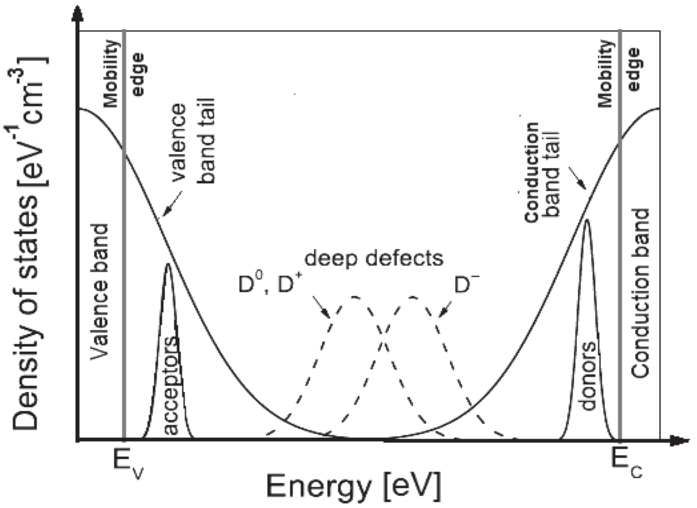

Figure 2.6 *Schematic density of states distribution for an amorphous semiconductor showing the bands, the band tails, and the deep defect states at different charge states (D^-, D^0 and D^+) within the band gap. The red lines indicate the mobility edges [Street1991].*

In disordered semiconductors, the bonding disorder of bond length and bond angle [Biswas1987] leads to some phenomena in the density of states that cannot be found in periodically ordered crystals. The short range order replaces the long range order in crystals, and the abrupt band edges of a crystal turn to band tails extending into the forbidden gap. The electronic structure illustrated in Fig. 2.6 [Mott1979].

In a semiconductor there is a forbidden energy region in which no electron states can exist, it is called an *energy gap* or *bandgap* (E_g). Energy bands are permitted above and below this energy gap. The upper band is called the *conduction band* (E_C), and the lower band is called the *valence band* (E_V). At absolute zero temperature, the valence band is fully occupied by electrons and the conduction band is empty.

It is commonly accepted that the energy-dependent DOS in disordered semiconductors is divided into three different energy ranges: The extended states in the conduction and valence bands, the localized states in the band tail region close to the band edges, and the deep defect states around midgap. The extended and localized states are separated by mobility edges at energy E_C and E_V. These derive their name from the fact that at zero temperature, only electrons above E_C and holes below E_V are mobile and contribute to the electrical conduction.

Extended states

The 'extended states' refer to the electronic states in both the conduction and the valence bands. At a temperature above zero, some electrons in the valence band are thermally excited into the conduction band, leaving holes in the valence band. These electrons in conduction band and holes in valence band are free to move within the atomic lattice of the solids and thereby can carry electrical current.

The extended state conduction is calculated as follows [Street1991]:

$$\sigma_{ext} = \sigma_{0e} \exp(-\frac{E_C - E_F}{\kappa_B T})$$

Here, σ_{0e} is the conductivity prefactor, E_C is the mobility edge of the conduction band, and E_F is the Fermi level, κ_B is the Boltzmann constant, and T is the absolute temperature.

Localized states

The 'localized states' refer to the electronic states in both the conduction and the valence band tails. The energy level of the states in the band gap determines whether it behaves as a trapping center or as a recombination center. Little energy is needed to set free the electrons trapped at shallow band tail states. Charge carriers (electrons or holes) collide with the traps and become immobilized. States near the midgap tend to be recombination centers.

Although there is no macroscopic conduction in localized states at T = 0 K, at elevated temperature, the motion of the charge carriers is also described by *hopping transport*, which occurs through tunneling transitions between localized states [Street1991]. There are two kinds of hopping conduction mechanisms:

① When the temperature is not too low and the average distance (r_D) to the nearest impurity site is much bigger than the fall-off radius of the impurity wave function (a_0), hopping conduction can take place in the band tails where the density of states is large but the carrier concentration is low. Hopping conductivity (σ_{hop}) depends both on the measurement temperature T (with an activation energy ΔE_{hop} between hopping states) and on the average distance r_D between the hopping sites (e.g. the nearest donors, or acceptors for *p*-type material.) as the following equation describes [Böer1990]:

$$\sigma_{hop} = \sigma_{0,hop} \cdot \exp(-\frac{\Delta E_{hop}}{\kappa_B T}) = \sigma_{00} \cdot \exp(-\frac{2r_c}{a_0}) \cdot \exp(-\frac{\Delta E_{hop}}{\kappa_B T})$$

r_c can be estimated as: $r_c \approx (0.865 \pm 0.015) \cdot N_{Donor}^{-\frac{1}{3}}$ (N_{Donor} is the donor density) [Mcinnes1979]. At low temperature, for low compensation, ΔE_{hop} can be estimated as [Efros1972]:

$$\Delta E_{hop} \approx 0.61 \frac{e^2}{4\pi\varepsilon_r\varepsilon_0} \cdot (\frac{4\pi}{3} N_{Donor})^{\frac{1}{3}}$$

For higher compensation, this equation is modified by a compensation ratio $K = N_{Acceptor}/N_{Donor}$.

② Hopping transport can also take place in the midgap between deep defect states when the defect density is very high (e.g. > 10^{18} cm^{-3}). In this case, σ_{hop} can be written as [Mott1968]:

$$\sigma_{hop} = \sigma_{0,hop} \cdot \exp\left[-(\frac{T_0}{T})^{\frac{1}{4}}\right] \text{ with } T_0 = \frac{C}{\kappa_B N(E_F) a_0^3}$$

Here C is a numerical coefficient, a_0 is the localization length of the states near E_F, T is absolute the temperature. $N(E_F)$ is the density of states at E_F.

2.3.2 Charge states of defects

Many localized defects in semiconductors can capture or release electrons or holes and thereby change their charge state. In disordered silicon, the dominant defect is Si-db. When a Si-db is occupied by 0 (unoccupied), 1 or 2 electrons, they are positively charged D^+, neutral D^0 or negatively charged D^-, respectively. The widely-investigated dbs in disordered Si and its alloys are an example for such a defect. They are located within the bandgap of the semiconductor, but their energy position depends on the charge state of the defects, as illustrated in Fig. 2.7.

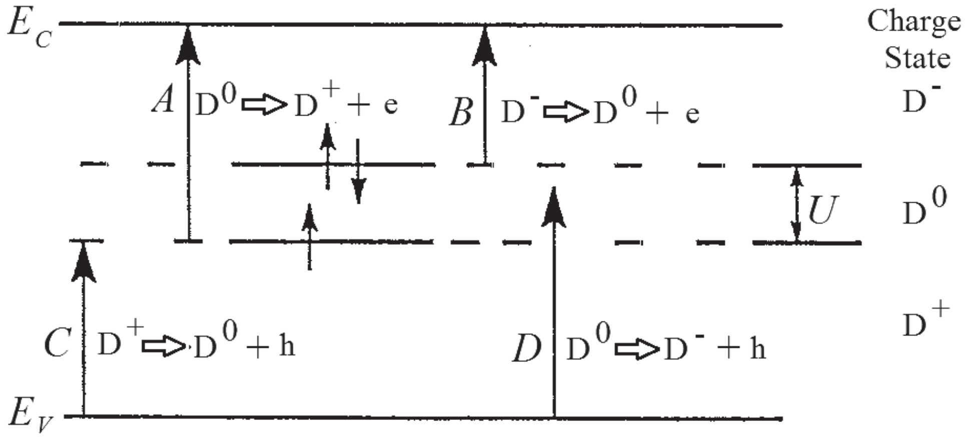

Figure 2.7 *Illustration of the charge states of dangling bonds and the four possible transitions between the conduction and valence bands. U is the correlation energy [Street1991]. A, B, C and D denote four possible electronic transitions.*

Starting from the singly occupied dangling bond state (D^0), the electronic energies of the first and second electrons are not the same because of electron-electron interaction. The addition of an electron to the same orbital influences the total energy of the defect in the following ways:

- Two electrons repel each other with a Coulomb interaction which is absent in the singly occupied state. The energy levels of the D^0 and D^- are split by the Coulomb correlation energy:

$$U_{Coulomb} = \frac{e^2}{4\pi\varepsilon\varepsilon_0 r_0}$$

Here r_0 is the effective separation of the two electrons and roughly the localization length of the defect wavefunction [Street1991].

- Another contribution to the correlation energy arises from the lattice relaxation at the defect which is caused by the addition of the second electron, and lowers the energy of the resulting D^- state by the relaxation energy U_{Relax}. The total effective correlation energy ($U_{effective}$) is a combination of $U_{Coulomb}$ and U_{Relax} as follows:

$$U_{effective} = U_{Coulomb} - U_{\mathrm{Re}lax}$$

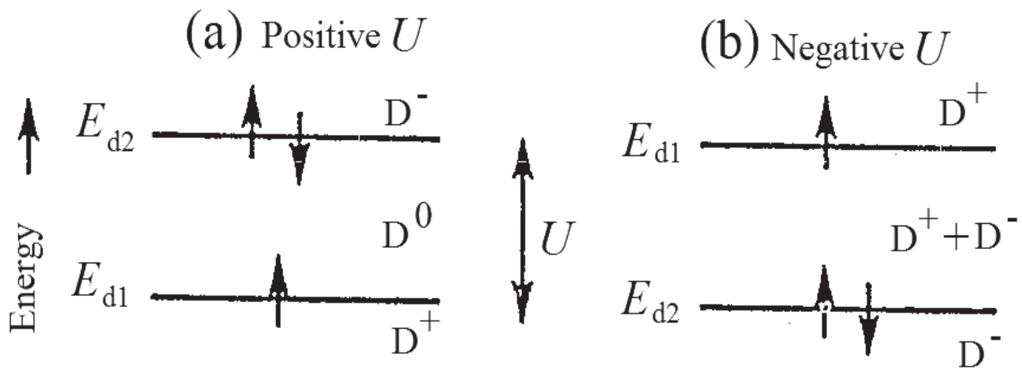

Figure 2.8 *Ordering of the gap states for defects with positive (a) and negative (b) $U_{effective}$. The diagram indicates the charge states D^+, D^0 or D^- when E_F is in the different energy regions.*

Fig. 2.8(a) shows the ordering of the gap states for the positive correlation energy ($U_{effective} > 0$). The energy of the unoccupied or singly occupied defects (D^+, D^0) lies below the doubly occupied (D^-) by an energy of $U_{effective}$. As ESR is only sensitive to the paramagnetic states with an unpaired electron spin, only the singly occupied D^0-defects are detectable.

Fig. 2.8(b) shows the ordering of the gap states for $U_{effective} < 0$. A negative $U_{effective}$ results in an equilibrium state that comprises an equal density of D^+ and D^- defects with no singly occupied states.

2.3.3 Doping mechanism

Intentional incorporation of impurities (e.g. *n*-type doping with N, P, and *p*-type doping with Al, B, Ga.) are typically used to provide additional free charge carriers. This is named *doping*. In c-Si, *n*-type doping shifts E_F away from midgap in the intrinsic material towards the conduction band, while *p*-type doping shifts E_F towards the valence band.

In contrast to c-Si, in disordered a-Si:H and μc-Si:H, the high concentration of intrinsic defects influences the free carrier concentration achieved by doping. Besides, doping may also induce a large amount of deep states in the gap, almost equal to the active donor or acceptor concentration, limiting the resulting shift of E_F [Soukoulis1985; Economou1987]. Deep defect states first have to be compensated before E_F can shift, e.g. donors will be compensated by the defects as they act as acceptors by creating D^- (occupied with two electrons) states.

2.4 Theoretical Background of ESR

The basics of ESR are essential for a clear understanding of the experiments and relevant results in this work. In this section the physical principles of ESR are briefly reviewed.

2.4.1 Spin Hamiltonian

The subject matter of ESR is the interaction of electrons with an external magnetic field, surrounding electrons and nuclei. The energy differences detected by ESR are predominately due to the interaction between unpaired paramagnetic electrons, the external magnetic field produced by a magnet and with nuclear spins. The energy of a paramagnetic center can be generally defined as follows, in terms of the so-called *spin Hamiltonian* [Abragam1951]:

$$H_0 = H_{EZ} + H_{HFI} + H_{EE}$$

Here, H_{EZ} is the electron – magnetic field interaction called "*electron Zeeman effect*", H_{HFI} is the *hyperfine interaction* between the electron spin S and nuclear spin I, and H_{EE} is the interaction between electron spins.

Electron spin – external magnetic field interaction (H_{EZ})

An electron possesses a magnetic moment $\vec{\mu}$ due to its spin $\vec{S}$ (in units of $\hbar$):

$$\vec{\mu} = -g \cdot \mu_B \cdot \vec{S} = -g \cdot \frac{e\hbar}{2m_e} \cdot \vec{S}$$

Here μ_B is the Bohr magneton, which is the natural unit of electronic magnetic moment, $\hbar = h/2\pi$ with the Plank constant h, and g is the g-tensor which is an important fingerprint for identifying electronic states. For free electrons, $g = 2.0023$.

The unpaired electrons of paramagnetic defects studied in the present work are $S = ½$ spin systems. In the absence of an external magnetic field $\vec{B_0}$, the two possible spin states with spin quantum numbers designated as $M_S = -½$ (parallel state) and $M_S = +½$ (antiparallel state) will populate at the same energy level with an equal population probability.

When $\vec{B_0}$ is applied, the degeneracy of the spin states is lifted, the energy state is split (the so-called *Zeeman splitting*) into two states which have an energy difference $\Delta E = g\mu_B B_0$. The interaction between $\vec{S}$ and $\vec{B_0}$ is given by the electron Zeeman term in the spin Hamiltonian:

$$\mathrm{H}_{EZ} = \mu_B \vec{B}_0 \cdot g \cdot \vec{S} / \hbar$$

When the electromagnetic radiation ($\Delta E = h\upsilon$, υ is the frequency of the ratiation) matches the Zeeman splitting that is caused by $\vec{B_0}$, the absorption of energy causes a transition from the lower energy state to the higher energy state, the effective *g*-value can be calculated as follows:

$$\Delta E = h\upsilon = g\mu_B B_0 \Rightarrow g = \frac{h\upsilon}{\mu_B B_0}$$

In conventional ESR spectroscopy, $\vec{B_0}$ is varied or swept and the frequencies at which absorption occurs correspond to the energy differences of the states.

However, in an isolated spin system, due to that the emission and absorption of microwave radiation take place at the same time, the populations of the two energy levels would soon equal to each other, and then no net-absorption would be detected even under resonance conditions. Therefore, a reservoir, which is a medium that the spin system can interact with and to which it can transfer energy, is necessary to maintain a population difference between different energy states. In a solid, the surrounding lattice of the spin system can play the role of reservoir. When an excited electron returns to the ground state, its energy will be transferred to the surrounding lattice within a time constant T_1. This process is called *spin – lattice relaxation*, and it is modulated by the lattice vibrations [Murphy1966]. Additionally, the interaction of the spins with each other, which is called *spin – spin relaxation*, is denoted with a time constant T_2.

Electron spin – nuclear spin interaction (H_{HFI})

Electrons are sensitive to their local magnetic surroundings. The nuclei in a molecule or complex often have a magnetic moment, which produces a local magnetic field at the site of the electron. The hyperfine interaction between the electron and the nuclei is given by

$$\mathrm{H}_{HFI} = \vec{S} \cdot \vec{A} \cdot \vec{I} = \vec{S} \cdot \vec{A}_{iso} \cdot \vec{I} + \vec{S} \cdot \vec{A}_{dip} \cdot \vec{I}$$

Here $\vec{A}$ is the hyperfine interaction tensor, which usually contains two hyperfine terms – The isotropic Fermi contact interaction:

$$A_{iso} = \frac{8\pi}{3} \mu_B g \mu_N g_N \, |\psi(r)|^2$$

and the dipole hyperfine interaction:

$$A_{dip} = \mu_B g \mu_N g_N (1-3\cos^2\theta)/r^3$$

Here, μ_N and g_N are characteristic for a specific isotope. $\Psi(r)$ is the overlap of the electron wave function with the nucleus at a distance r. The Fermi-contact term does not depend on the angle θ between electron spin S and nuclear spin I and is therefore isotropic. In contrast, the dipole term depends on θ and is anisotropic.

Electron spin – spin interaction (H_{EE})

Electron spins would interact with each other mainly through two mechanisms:

Dipole interaction: It is in analogy with the anisotropic hyperfine interaction between an electron and nuclear spin interaction. It is due to the dipolar fileld, which is caused by a spin S in the vicinity and acts as an external field for the spin being observed. This interaction leads to an instantanuous change of the local field and the Larmor frequency of the spin. Since the dipolar field from the nearby spins depends on the distance between spins, this process is dominant for high spin density samples.

Exchange interaction: Consider two-electron states, the total wave function $\varphi(\vec{r})\chi(\vec{s})$ (here, $\varphi(\vec{r})$ is the orbital part, $\chi(\vec{s})$ is the spin part) is antisymmetric due to the Pauli exclusion princilple. The Coulomb interaction between the electrons lifts the degeneracy of the states with different total spin. The exchange interaction takes place through random fluctuations of the interaction of unpaired spins and nuclei in the matrix.

2.4.2 Linewidths

In an ESR spectrum, the analysis of the lineshape and linewidth would give a large amount of information about the spin system. There are two types of broadening mechanisms – "*inhomogeneously broadening*" and "*homogeneously broadening*". A more detailed description about the mechanisms of broadening can be found elsewhere [Poole1971; Weil2007].

Inhomogeneous Broadening

The overall ESR line is regarded to be composed of a number of narrower individual lines due to the so-called *spin packet*, which is a system of spins precessing with the same frequency around their individual magnetic field vectors $\overrightarrow{B_1}$ (given by the superposition of the external field and the local fields). This means that the lineshape (e.g. the transition probability as a function of magnetic field) is the same for each spin packet. Inhomogeneous line broadening occurs if the observed line is a superposition of a large number of individual inequivalent spin packets, each slightly shifted from the others (different *g*-values).

The following are some causes of inhomogeneous broadening for a given spin species:

- The disorder of the atomic structure, e.g. bond length and bond angles;
- An inhomogeneous external magnetic field;
- Unresolved fine and hyperfine interaction;
- Crystal irregularities lead to anisotropic interactions. Here the distribution of local magnetic fields resulting from the anisotropic *g* and hyperfine interaction gives rise to the inhomogeneity. In this case, the lineshape may be highly asymmetric.
- Dipolar interactions between unlike spins. These may impose a random local field at a given unpaired electron, arising from dipolar fields from other electron spins.

Homogeneous Broadening

Homogeneous broadening is an increase of the width of an ESR line originating from the "Natural broadening" (lifetime broadening) – Any transition which has a finite lifetime Δt has an energy uncertainty given by:

$$\Delta E = \hbar / \Delta t$$

If an ESR line shows homogeneous broadening, its spectral linewidth is its natural linewidth, with a lorentzian profile.

For a set of spins, they all see the same net magnetic field (More accurately, the local fields give the same time-averaged field over sufficiently short intervals) and have the same spin-hamiltonian parameters. This means that the lineshape (e.g. the transition probability as function of magnetic field) is the same for each dipole, all with a full width at half maximum (FWHM) in frequency units of $1/T_2$ in the absence of microwave power saturation.

Powder pattern

For paramagnetic centers with certain symmetry, principally one can determine the components of *g*-tensor by changing the sample orientation with respect to the external magnetic field, e.g. dangling bond defects in crystalline environments which possess axial symmetry with respect to the direction of the unsaturated sp^3-hybrid.

However, in isotropic materials (e.g. a-Si:H or µc-Si:H and disordered Si alloys) in the sense that all possible orientations of a symmetric defect wave function are present, thus all orientations of spins can be observed at the same time and the angular dependence of ESR spectra is smeared out by the inhomogeneous broadening mechanism. The obtained spectra are called "*powder pattern*" [Atherton1993]. Therefore, in the disordered material, no angular dependence of ESR spectra can be extracted from the powder pattern.

2.4.3 Signal intensity

For a system of ideal non-interacting paramagnets (non-degenerate, Maxwell-Boltzmann distribution) with spin angular momentum S and spin number N_{spin}, the temperature dependence of the magnetic susceptibility χ_0 is given as follows [Atherton1993]:

$$\chi_0 = \frac{N_{spin}\mu_0\mu_B^2 g^2 S(S+1)}{3\kappa_B T}$$

In the absence of microwave power saturation, the ESR signal intensity (determined as the integration area under an absorption curve) is proportional to χ_0 and to N_{spin}, but inversely proportional to the temperature. This kind of electronic paramagnetism is referred to as *Curie-like*. For electrons with spin $S = ½$ and $g \approx 2$, χ_0 is expressed as:

$$\chi_0 = \chi^{Curie} = \frac{N_S\mu_0\mu_B^2}{\kappa_B T} \propto \frac{1}{T}$$

On the other hand, when the electron gas is degenerate, the statistics of ideally non-interacting paramagnetic centers are governed by the Fermi-Dirac-distribution. This kind of electronic paramagnetism is referred to as *Pauli-like*. The resulting paramagnetic susceptibility is calculated as [Pauli1927]:

$$\chi_0 = \chi^{Pauli} = \frac{N_{spin}\mu_0\mu_B^2}{E_F} \propto N_S$$

A study of the temperature behavior of the spin number, which is equal to the signal intensity, should therefore enable one to distinguish between the degenerate and the non-degenerate case.

In this work, temperature-dependence ESR measurements show that the electronic paramagnetism of Si (a-Si:H and µc-Si:H) and its alloys µc-SiC:H and µc-SiO$_x$:H follow the *Curie-like* behavior. Therefore, ESR measurements at different temperatures will not lead to differences of spin densities.

Chapter 3: Characterization methods

In this chapter, all the characterization methods employed in this work will be introduced, including the Electron Spin Resonance (ESR) technique, Raman scattering and Fourier Transformed Infra-Red (FTIR) spectroscopy for microstructure analysis, Secondary Ion Mass Spectroscopy (SIMS) and Rutherford Backscattering Spectroscopy (RBS) for chemical composition analysis, electrical conductivity (σ_D) for electrical properties and Photo-thermal Deflection Spectroscopy (PDS) for optical properties, and thin film thickness measurement.

3.1 Electron Spin Resonance

3.1.1 ESR experimental set-up

Fig. 3.1 shows the schematic diagram of the commercial X-band spectrometer BRUKER ESP E580. In Fig. 3.1(a), from left to right, one can see three main parts: A computer which runs the control software; the console which contains the data acquisition server,the bridge controller, digitizer and pulse programmer; the main working body that consists of the microwave bridge, travelling-wave tube amplifier, magnet, resonator and power supply. A Gunn diode (microwave frequency $\upsilon \approx 9.3$ GHz) with an optimum power output of 200 mW was used as the microwave source. Fig. 3.1(b) and (c) show the block diagram of the whole ESR spectrometer and the microwave bridge. Detailed operation principles are available in the Bruker manual [Weber2005].

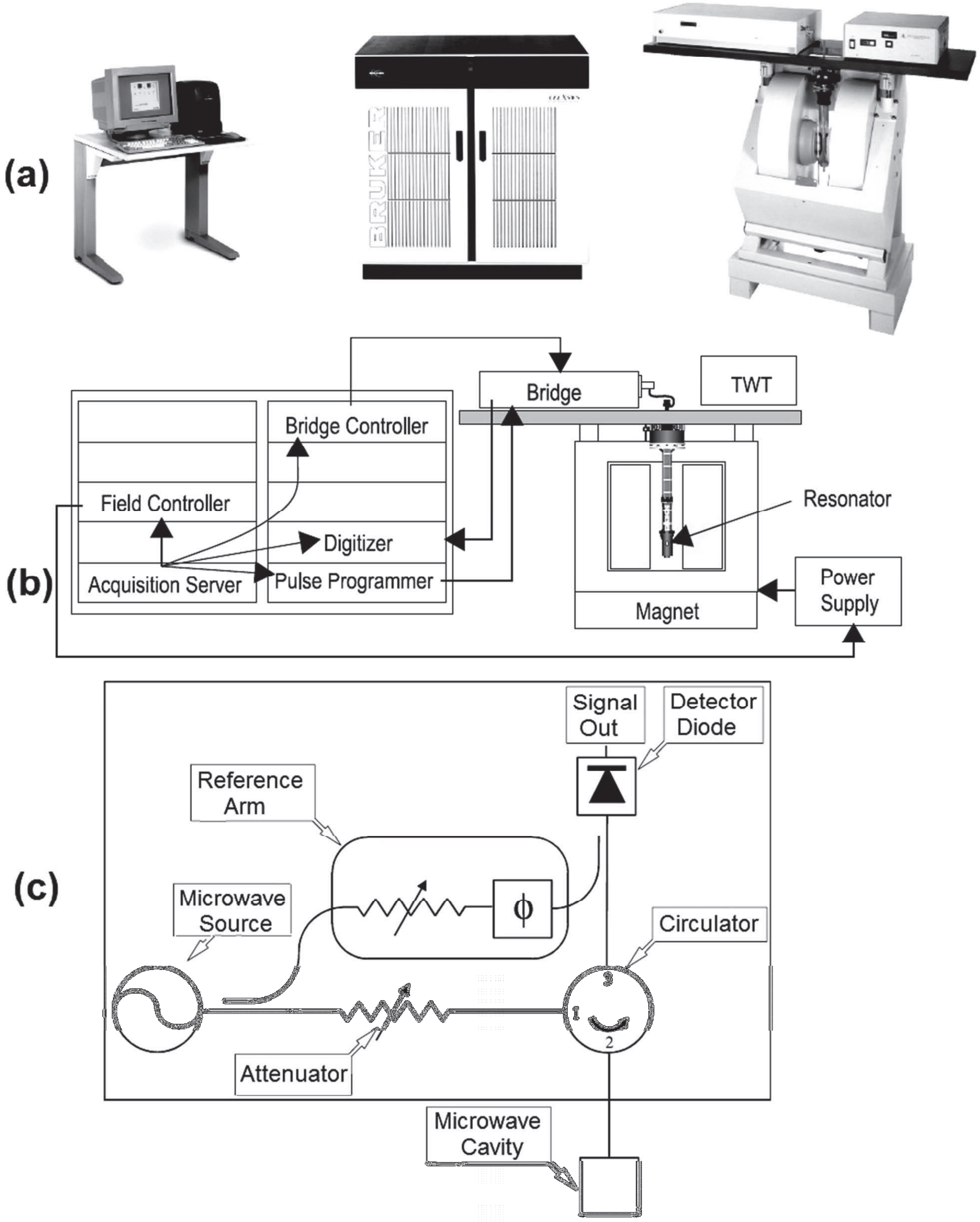

Figure 3.1 *The general layout of an ESR spectrometer (a), block diagram of an ESR spectrometer (b) and of the microwave bridge (c) [Weber2005].*

3.1.2 Spin density, *g*-value and linewidth

A sputtered unhydrogenated amorphous silicon (a-Si) thin-film sample with a known spin number of 2×10^{15} and g = 2.00565 has been used as a secondary standard for spin density and magnetic field calibration. From the traditional continuous wave electron spin resonance (cw-ESR) measurements, the following three data could directly be obtained [Müller1998(1)].

The g-value of the samples can be calculated by

$$g_{sample} = \frac{h\upsilon_{sample}}{\mu_B B_0} = \frac{h\upsilon_{sample}}{\mu_B (B_{sample} + \Delta B)} .$$

Here, υ_{sample} is the microwave frequency of the sample measurements, B_{sample} is the magnetic field at the center of the resonance line (maximum absorption) of the sample, h = 6.626×10^{-34} J·s is the Planck constant, μ_B = 1.381×10^{-23} J/K is the Boltzmann constant, ΔB and is the calibration value of the magnetic field, and it is calculated as follows

$$\Delta B = \frac{h}{\mu_B} \times \frac{\upsilon_{st}}{2.00565} - B_{st} .$$

Here, υ_{St} and B_{St} are the measured microwave frequency and the magnetic field at the center of the resonance line (maximum microwave absorption) for the standard sample (sputtered a-Si).

The spin density of the samples can be calculated by

$$N_S \left[cm^{-3}\right] = \frac{Q_{St}}{Q_{Sample}} \times \frac{A_{sample}}{A_{St}} \times \frac{2\times10^{15}}{V_{sample}} .$$

Here, Q_{sample}, Q_{St}, A_{sample} and A_{St} denote the quality factor of the cavity and the signal amplitude obtained by numerical double integration of the area under the absorption curve of the cw-ESR spectrum for the sample and the standard. V_{sample} is the sample volume.

In some cases, the surface spin density (N_{Sf}) is calculated by

$$N_{Sf} \left[cm^{-2}\right] = \frac{Q_{St}}{Q_{Sample}} \times \frac{A_{sample}}{A_{St}} \times \frac{2\times10^{15}}{S_{sample}} .$$

Here, S_{sample} is the film surface area in the unit of cm^2.

Peak-to-peak linewidth (*H_{PP}*): This is the distance between the maximum and minimum points of the ESR derivative spectra. H_{PP} differs from the full width at half maximum (FWHM or $\Delta H_{½}$) by a numerical factor that depends on the specific lineshapes. Homogeneous and inhomogeneous broadenings are introduced in Section 2.4.2.

For measurements at a temperature below the room temperature (RT), a He gas flow cryostat (Oxford ESR 900) has been used to offer a temperature range from 4.5 to 300 K. Details of the sample preparation and subsequent handling can be found within each chapter.

3.2 Structural properties

Characterization of the structural properties of a-Si:H, µc-Si:H, µc-SiC:H and µc-SiO$_x$:H will be focused on the material crystallinity determined with Raman scattering (I_C^{RS}) and infrared spectroscopy (I_C^{IR}). The chemical composition is analyzed by SIMS and RBS.

3.2.1 Raman Spectroscopy

Raman spectroscopy is commonly used to identify the chemical bonding and symmetry of molecules by studying vibrational, rotational and other low – frequency modes in a system. Typically, a monochromatic light beam from a laser illuminates the sample. Raman spectrum is a result of nonelastic photon scattering in the sample medium. The spectrum contains information on the lattice vibrations, i.e. the phonon spectrum of the sample. The phonon spectrum in turn is closely related to the material structure. More details about the principles and interpretation of Raman spectroscopy can be found in literature, e.g. [Larkin2011].

In the present work, Raman spectroscopy is used to evaluate the crystallinity of a-Si:H, µc-Si:H and µc-SiO$_x$:H films. Fig. 3.2 shows the measured Raman spectra of c-Si, µc-Si:H and a-Si:H. In c-Si, a narrow peak at 520 cm^{-1} with a linewidth of about 3.5 cm^{-1} corresponds to the excitation of the transverse optical (TO) phonon at the Brillouin zone center. In a-Si:H, the TO-phonon peak turns out to be a broad prominent hump at 480 cm^{-1} [Smith1971].

µc-Si:H is commonly accepted to consist of amorphous tissues and crystallites, therefore it would contain the features of both a-Si:H and c-Si, although the crystalline peak is often shifted and broadened due to the variation of the crystallites grain size and to stress in the film. A standard a-Si:H sample is measured. Fitting the as-measured Raman spectra of µc-Si:H with the spectra of the standard a-Si:H, which shows a broad line at 480 cm^{-1}, the rest of the signal is attributed to the crystalline Si phase, the Raman crystallinity (I_C^{RS}) of µc-Si:H sample is evaluated by

$$I_C^{RS} = \frac{I_{\mu c-Si:H} - I_{a-Si:H}}{I_{\mu c-Si:H}} .$$

Here $I_{\mu c\text{-}Si:H}$ and $I_{a\text{-}Si:H}$ are the numerical integration of the area under the measured Raman spectra of µc-Si:H and the fitted Raman spectra of a-Si:H.

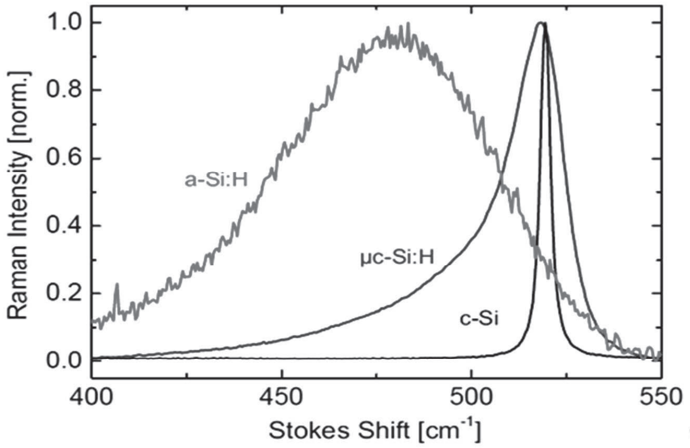

Figure 3.2 *Raman spectra of c-Si (black), µc-Si:H (blue) and a-Si:H (red). All spectra are normalized to the same maximum to facilitate lineshape comparison.*

Similar to µc-Si:H, µc-SiO$_x$:H is a phase mixture of µc-Si:H and a-SiO$_x$:H, so one can presumably use Raman measurements to evaluate the crystallinity. Fig. 3.3 shows a measured Raman spectrum of a µc-SiO$_x$:H thin film. Fitting the as-measured Raman spectra with a standard a-SiO$_x$:H sample which shows a broad line at 480 cm^{-1}, the rest of the signal is attributed to the µc-Si:H phase, the crystallinity of µc-SiO$_x$:H could be evaluated by

$$I_C^{RS} = \frac{I_{\mu c-SiO_x:H} - I_{a-SiOx:H}}{I_{\mu c-SiO_x:H}} .$$

Here $I_{\mu c\text{-}SiOx:H}$ and $I_{a\text{-}SiOx:H}$ are the numerical integration of the area under the measured Raman spectra of µc-SiO$_x$:H and the fitted Raman spectra of a-SiO$_x$:H.

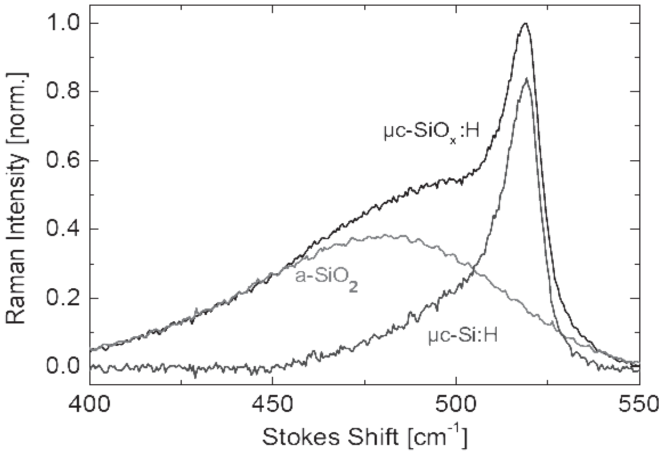

Figure 3.3 *Raman spectrum of a μc-SiO$_x$:H (black) sample and an a-SiO$_2$ (red). Fitting a-SiO$_2$ with the hump of μc-SiO$_x$:H at 480 cm^{-1}, the rest is regarded to be μc-Si:H phase (blue).*

But one should note the following problems for the evaluation of the crystallinity of the μc-SiO$_x$:H material from Raman spectra: (1) The absorption coefficient of the highly transparent a- SiO$_x$:H is much (e.g. a factor of ten times) lower than μc-Si:H at λ_{laser} = 488 nm for Raman spectroscopy. This leads to an overestimation of the μc-Si:H phase when calculating the crystallinity for layers with higher oxygen contents. (2) For μc-SiO$_x$:H films which are grown on a seed layer, the Raman signal generated by the light reaching the μc-Si:H-seed layer will contribute to the calculated crystallinity. So care has to be taken when using this approach as a measure of crystallinity.

Fig. 3.4 shows the Raman spectrum of a μc-SiC:H thin film sample prepared by hot-wire chemical vapor deposition (HWCVD) on a Cr-coated glass substrate. In the Raman spectrum of crystalline SiC, the sharp peaks can be clearly resolved [Nakashima1997]. In μc-SiC:H, the assignments of peaks can refer to c-SiC (as noted in the graph). But still it is difficult to quantitatively distinguish the amorphous, cubic, hexagonal and crystalline SiC phase unambiguously. Variation of grain sizes, presence of high density of grain boundaries boundaries and stacking faults make the evaluation of crystallinity for μc-SiC:H from Raman measurements unavailable at the moment. In this work, the infrared spectroscopy is used to indicate the extent of disorder in μc-SiC:H thin films and evaluate the crystallinity (I_C^{IR}) semi-quantitatively.

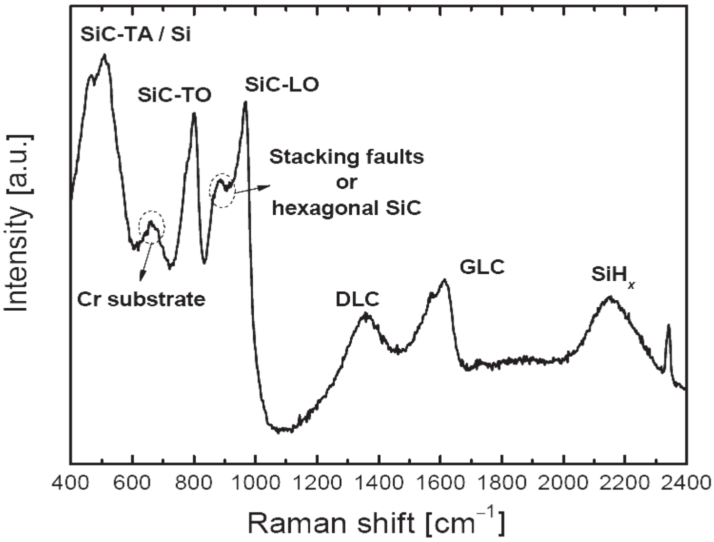

Figure 3.4 *Raman spectrum of a μc-SiC:H film. Corresponding phonon modes are indicated as follows: TA – transverse acoustic; TO and LO – transverse and longitudinal optical phonon modes; DLC and GLC mean diamond-like and graphite-like carbon, respectively [Dasgupta2008(1)]. The spike at 2320 cm^{-1} is an artifact possibly caused by N_2.*

3.2.2 Fourier Transform Infrared (FTIR) spectroscopy

The structure and the bonding configuration of SiC were investigated by FTIR spectroscopy for thin films deposited on Si wafers. The infrared spectrum of the μc-SiC:H film has a broad band at 600 – 1200 cm^{-1}, due to the stretching vibration of Si-C bonds [Spitzer1959; Dkaki2001]. The Si-C stretching mode in infrared absorption was deconvoluted into a Gaussian and a Lorentzian component with fixed peak position and linewidth. Only the peak intensity was varied. A Gaussian lineshape of the Si–C mode indicates a distribution of bond length and bond angles. This distribution is regarded as characteristic for the amorphous phase. The change in the lineshape from more Gaussian to more Lorentzian-like indicates a decrease in the material disorder due to the formation of micro-crystallites. Therefore, the ratio of the integrated intensity of the Lorentzian component to the total intensity of Gaussian plus Lorentzian components was evaluated and tentatively correlated to the disorder extent.

$$I_{SiC}^{IR} = \frac{I_{Lorentzian}}{I_{Lorentzian} + I_{Gaussian}} .$$

Higher values of I_{SiC}^{IR} correspond to lower disorder of the μc-SiC:H material. More details can be found in several publications [Calcagno2001; Kerdiles2002; Miyajima2007; Finger2009].

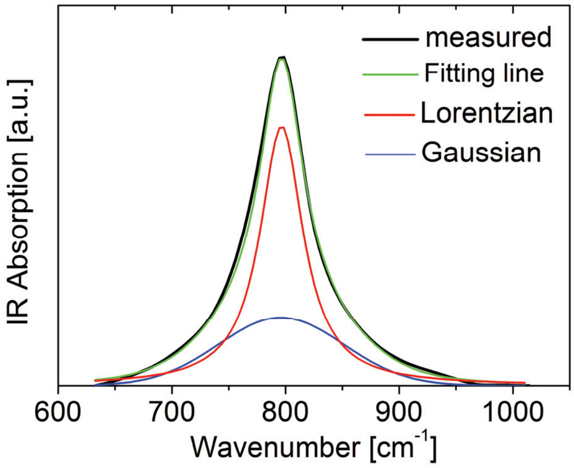

Figure 3.5 *(a) IR stretching mode spectra (black) of μc-SiC:H. The spectrum was decomposed into a Lorentzian (red) and a Gaussian (blue) line, corresponding to crystalline and amorphous phases, respectively.*

Fig. 3.5 shows a measured IR spectrum and its deconvolution for a μc-SiC:H thin film sample. During the peak-fitting process, the Lorentzian line was fixed with the peak position at around 800 cm^{-1} and FWHM of 60 cm^{-1}. The peak position of the Gaussian line was varied between 775 and 850 cm^{-1} with FWHM = 100 cm^{-1}. One can see that the sum of Lorenzian and Gaussian lines fits the measured line quite well.

3.2.3 Secondary Ion Mass Spectroscopy (SIMS)

SIMS is a powerful technique used to analyze the chemical composition of solids. It is often used to detect impurity concentrations (e.g. oxygen, nitrogen, carbide, boron, phosphorous, *etc.*) in silicon thin films, silicon alloys and silicon-based thin film solar cells. For SIMS measurements, a focused primary beam of cesium ions (Cs^{+}) with an energy of about 6 kV was accelerated towards the surface of the specimen. The impinging high energy ions eject molecules, neutral atoms and secondary ions that are analyzed by means of a quadrupole mass spectrometer to recognize different elements. The output of a SIMS measurement is the number of counts per atomic weight. In order to increase the signal-to-noise ratio, an ultra-high vacuum measurement environment is required.

In this work, using a quadrupole instrument (Atomika 4000), SIMS measurements were made to determine the concentration of C, H, N, O, Al-dopant in μc-SiC:H material. More details about the set-up, the operation principles and applications can be found in many textbooks and references therein [Benninghoven1987].

3.2.4 Rutherford Backscattering Spectrometry (RBS)

RBS is frequently used to determine the structure and the chemical composition of materials. A beam of incident He^{2+} ions (the projectile) are accelerated to high kinetic energies, usually in the range of 1 – 3 MeV, and impinge on the stationary nucleus located in the sample (target). The energies of backscattered ions are measured over some range of angles. Therefore, the energy of the backscattered ions is determined by the energy loss at the backscattering, which may take place in two processes:

One is the energy loss when ions scatter with nucleus in samples. This process depends on the mass and atomic number of the nucleus. For a given measurement angle, nuclei of two different elements will therefore scatter incident ions to different degrees and with different energies, producing separate peaks on an $N(E)$ plot (measurement count versus energy E). These peaks are characteristic of the elements contained in the material, providing a means of analyzing the composition of a sample by matching scattered energies to known scattering cross-sections. Relative concentrations can be determined by measuring the heights of the peaks.

The other is the energy loss when ions scatter with electrons in samples. This process depends on the electron density and the distance traversed in the sample. Instead of sharp backscattered peaks, peaks on an $N(E)$ plot weaken gradually towards lower energy as the ions pass through the depth occupied by that element. Elements which only appear at some depth inside the sample can be determined from the width and shifted positions in the energy spectrum, and their relative concentrations from the peak heights.

In this work, RBS technique was used to determine the incorporated oxygen content in µc-SiO$_x$:H thin films. The accuracy of the stoichiometry of SiO$_x$ is ±1% independent of its microscopic structure. More details about the operation principles and applications could be found in many textbooks and references therein [Palmetshofer2011].

The RBS measurements were provided by Bernd Holläner from the Institut für Festkörperforschung (IFF) at the Forschungszentrum Jülich, Germany.

3.3 Electronic properties

3.3.1 Electrical conductivity

The electrical transport in amorphous and microcrystalline semiconductors is a complex phenomenon which is dependent on many different features, e.g. the electronic density of states in the bands, in bandtails, and/ or bandgap, the Fermi level position, the temperature, *etc*. Assuming that the thin films are homogeneous, the macroscopic quantity σ represents an average of all contributing conduction mechanisms, and is directly related to the mobility (μ) and concentration (N) of the charge carriers (mobile holes and electrons). σ is determined by

$$\sigma = e\mu_e N_e + e\mu_h N_h$$

Here, e is the elementary charge, μ_e and μ_h are the mobilities, N_e and N_h are the concentrations of electrons and holes, respectively.

In this work, σ was measured with a Keithley electrometer that measured the current-voltage (I-V) characteristics of the sample. Two silver contacts (width $b = 0.5$ cm and distance $l = 500$ µm) were thermally evaporated onto the films. The current density between the contacts is assumed to be uniform. The substrate of the thin films is glass, which has a much lower conductivity than µc-Si:H. The current is therefore expected to flow exclusively through the thin film. σ was measured at RT in high vacuum (pressure $\leq 10^{-5}$ mbar) to avoid atmospheric influences. Before the measurement, films were annealed at 440 K for 30 min to desorb water and other atmospheric species on the film surface. σ is calculated by

$$\sigma = (I \cdot l)/(d \cdot b \cdot V)$$

Here, d is the film thickness.

3.3.2 Photo-thermal Deflection Spectroscopy (PDS)

Since it was first used for optical absorption measurement of thin film Si [Jackson1981], PDS was developed to be a powerful method featuring high sensitivity.

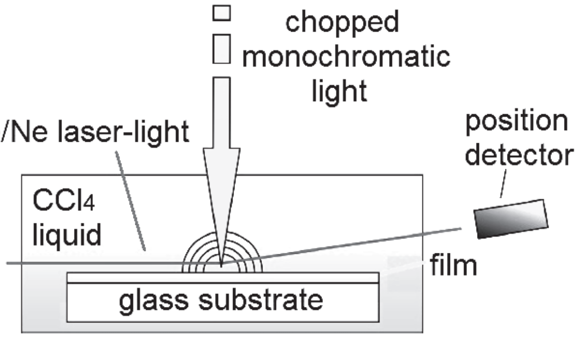

Figure 3.6 *Schematic drawing of the working principles of PDS [Wördenweber2011].*

Fig. 3.6 shows the schematic picture of the working principles of PDS. A glass substrate with a sample film is placed in the CCl_4 liquid, which is transparent in the photon energy range of the illumination light and its refractive index strongly depends on temperature. A chopped monochromatic light beam was used to illuminate the film sample. The film absorbs the light and converts the absorbed photon energy into heat which is transported to the surrounding CCl_4 liquid. The temperature gradient close to the surface results in a refractive index profile, which in turn causes the deflection of a probe beam and is related to the optical absorption of the sample.

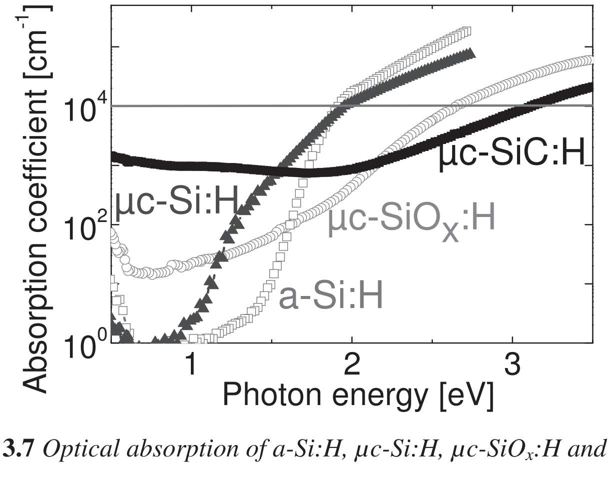

Figure 3.7 *Optical absorption of a-Si:H, μc-Si:H, μc-SiO$_x$:H and μc-SiC:H.*

In this work, PDS is used to measure the optical absorption of a-Si:H, µc-Si:H, µc-SiO_x:H and µc-SiC:H films (Fig.3.7). The photon energy E_{04}, at which the absorption coefficient is 10^4 cm^{-1}, can be determined as a measure of the optical band gap of µc-SiC:H and µc-SiO_x:H.

3.4 Thickness measurements

The thickness of the thin films is measured using a mechanical step profiler (Sloan DEKTAK 3030, Veeco) equipped with a 12 µm diameter stylus moving across the sample surface. In order to measure the thickness of the thin films, a step between the underlying Corning glass substrate and the surface of the film should be made. For different materials, such steps were made in different ways:

(1) For a-Si:H, µc-Si:H and µc-SiO_x:H films on glass substrates, a step for thickness measurements was made by etching the silicon layer with a KOH solution, until the underlying glass substrate was reached; or using laser-scribing to ablate the layer.

(2) µc-SiC:H is insensitive to the chemical reaction with HCl, H_2SO_4 or HF acid, and it is difficult to ablate the layer on glass with a laser due to its high transparency, either. Additionally, the µc-SiC:H layer has a strong adhesion to the glass substrate, this makes it difficult to use mechanical cutting methods to scrape off the layer.

Therefore, steps for later-on thickness measurements were made by masking off small dots with an approximate diameter of 1~2 mm with ink or liquid silver before film deposition. After overall deposition, µc-SiC:H material covers on both the glass and these dots. The ink can be scrubbed away simply using tissues with propanol. And, the raised silver dots can be scratched away using a scalper. With the step, film thicknesses were measured on DEKTAK. The average value of measured thickness was taken as the thickness of the µc-SiC:H thin film.

(3) For the material which has weak adhesion to the substrate (e.g. thick porous highly crystalline µc-Si:H), one can peel a small piece of film off the glass with plastic adhesive tape and then measure the height difference between the substrate and film surface to get the film thickness. For the very thin films with a thickness below 30 nm, the thickness is estimated by the deposition rate and deposition time which could be calculated from the thicker films with the same deposition parameters.

Chapter 4: Influences of glass substrates on the ESR measurements of film samples

In this chapter, first the motivation of ESR investigations of glass substrates is given. Afterwards, the ESR properties of these glass substrates before and after H-plasma surface treatment are presented. Finally, the interface between the glass substrate and the subsequent μc-SiO_x:H thin film is investigated.

4.1 Glass substrates exposed to hydrogen plasma

In this work, two types of alkali free borosilicate glasses were used for thin-film deposition: Corning1737 and Corning Eagle^{2000} (In the following, they will be referred to as CG1737 and EG2000, respectively). For both glasses, the thickness can either be 0.7±0.07 or 1.1±0.07 mm. The high broadband optical transmission and low light absorption make these kinds of glasses appropriate for being used as substrates of thin-film Si layers and solar cells. Prior to deposition, all the glass substrates were cleaned by sonication in a warm (65 °C) solution of a decontaminant diluted in deionized water, rinsed with deionized water and dried in a spin dryer.

When using substrates for film deposition, additional problems may arise from the fact that the substrate itself possibly has its own ESR-active species, for instance, *E´* centers (where *E´* denotes an oxygen vacancy in SiO_2), which is often observed in quartz and silica glasses [Weeks1956; Nelson1960; Weeks2008].

A number of pre-existing and post-manufacture-treatment-induced paramagnetic defects in silica and silicate glasses have been reported [Combrisson1954; Lenahan1998, Skuja2008]. For instance, during the PECVD process, some defects may be created due to surface etching by the reactive species of the plasma. Even at low concentrations, these defects may contribute to the ESR signal, especially when the signal from the film on the glass substrates is weak; the signal from the glass itself becomes pronounced and may cause data misinterpretation.

Another source of parasitic contributions to ESR spectra of thin films on glass is the interface states between the glass substrate and the material grown on it. An example is the P_b-center at the Si/SiO$_x$ interface [Stesmans1991, and references therein].

For the H-plasma treatment, cleaned glasses – CG1737(0.7mm), EG2000(0.7mm), CG1737(1.1mm) and EG2000(1.1mm), each with a size of 2.5×10 cm^2, were preheated at 185 °C in high vacuum for 2 h, exposed to the H-plasma in a PECVD system for 5 min, and then moved out of the deposition chamber to a transfer lock and finally cooled down to room temperature in a high vacuum (pressure < 10^{-5} pa) before ESR measurements. Glasses with and without H-plasma treatments were cut to pieces with the size of about 2×0.3 cm^2 and placed in the ESR quartz tube (Wilmad Glass type 710-SQ-250 with an inner diameter of 4 mm). For glasses with a thickness of 1.1 mm, two stacked pieces fit in the tube for ESR measurements; for glasses with the thickness of 0.7 mm, three to four pieces have been placed in the tubes.

Fig. 4.1 shows the ESR spectra of different glasses with (red lines) or without (black lines) H-plasma treatment. ESR measurements were performed at 40 K, modulation frequency = 100 kHz, modulation amplitude = 3G and microwave power = 0.02 mW. All the spectra were normalized to the same glass surface area for a comparison of ESR lineshape and spectral intensity.

No ESR signal is observed for the glasses that were cleaned in the standard way before film deposition. However, the glasses that have been treated with H-plasma exhibit different ESR features. All the H-plasma-treated glasses show ESR signals centered at $g \approx 1.998$ and 2.014. The first signal has an asymmetric lineshape with a peak-to-peak linewidth of about 32.5 G, and the signal at $g \approx 2.014$ is not as pronounced as the signal at $g \approx 1.998$.

As noted in Fig. 4.1 that, for EG2000(0.7mm), CG1737(1.1mm) and EG2000(1.1mm), the surface spin density are N_{Sf} = 1.8×10^{15}, 2.0×10^{15} and 5.4×10^{14} cm^{-2}, respectively. As for CG1737(0.7mm), the H-plasma treatment results in little increase of the ESR spectral intensity. One should always be aware of these glass signals during ESR evaluation of samples on glasses.

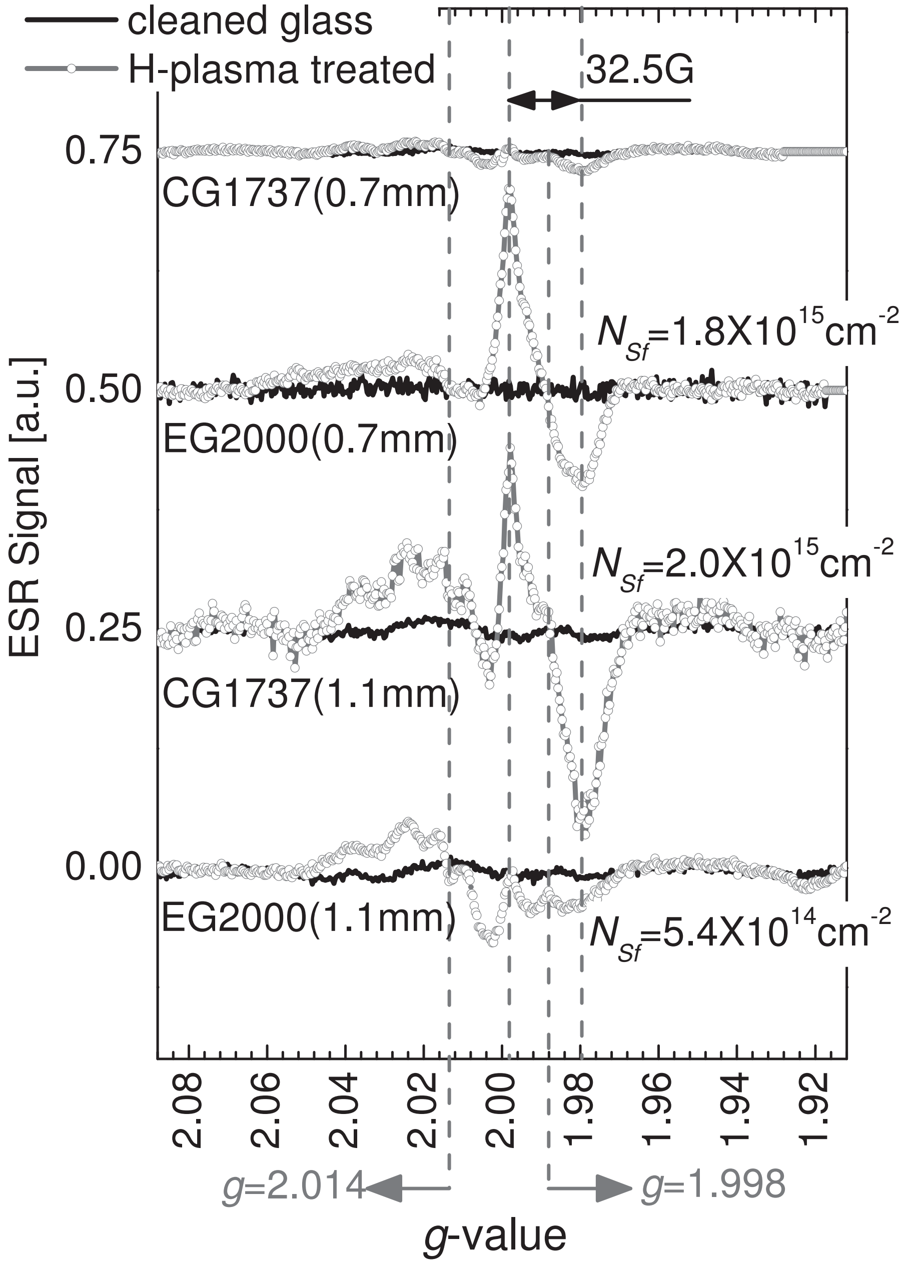

Figure 4.1 *ESR spectra of different glasses with (red) and without (black) H-plasma treatment. ESR spectra were measured at 40 K and normalized to the same glass surface area.*

4.2 Glass substrates covered with μc-SiO$_x$:H films

ESR measurements of μc-SiO$_x$:H thin films suffer from the glass signal, especially for those films with a relatively low spin density and/or a film thickness of less than 100 nm. When the signal of the deposited layer is not strong enough, the glass signal could lead to data misinterpretation. Therefore, it is necessary to perform a comparative study of μc-SiO$_x$:H on glass substrates in terms of the following two aspects:

- To which extent will the H-plasma induced glass signal distort the μc-SiO$_x$:H signal?
- How to exclude this H-plasma induced background signal for interpretation of ESR properties of μc-SiO$_x$:H material?

All the μc-SiO$_x$:H films were deposited with a thickness varied from a few tens nm to 1600 nm.

4.2.1 Glass substrates covered with very thin μc-SiO$_x$:H films

Using 1 sccm SiH_4 (with 2% PH_3), 500 sccm H_2 and 7 sccm CO_2 as precursor gases, μc-SiO$_x$:H thin films were deposited by PECVD on glass substrates – CG1737(1.1mm), CG1737 (0.7mm), EG2000(1.1mm) and EG2000(0.7mm). The deposition rate was estimated to be 0.1 nm/s. The deposition time was varied from 0, 10, 20, 40, 80, 160, 640 to 1280 s. Therefore, the estimated film thickness varies from 0 to ~128 nm, correspondingly.

After film deposition, glasses were cut into small pieces with the size of about 2×0.3 cm^2 for ESR measurements at a temperature $T = 40$ K with modulation frequency = 100 kHz, modulation amplitude = 3 G and microwave power = 0.02 mW. All the spectra in Fig. 4.2 show a resonance at $g \approx 2.004$ with intensity increasing with the film thickness (indicated by arrows in Fig. 4.2). This signal was also found in very thick (> 1600 nm) μc-SiO$_x$:H samples and tentatively attributed to the Si-dangling bonds in μc-Si:H surrounded by a-SiO$_x$:H [Xiao2010(1)]. This result is in good agreement with the reported values – In intrinsic a-SiO$_x$:H, the reported effective average g-value is 2.0050; for PH_3-doped n-type a-SiO$_x$:H, the g-value varies from 2.0035 to 2.0050 with increasing oxygen content [Janotta2004].

On the other hand, early in 1960s, it has been suggested that mechanical damage might give rise to detectable ESR signals which are attributed to free radicals [Windle1964]. Following this suggestion, one may also link the signal at $g \approx 2.004$ with the mechanical cutting action of the glass substrates. Further work is required to investigate the cutting effect on glasses.

For films deposited on CG1737(1.1 mm) and EG2000(0.7 mm) glasses, also another signal at $g \approx 1.99$ was observed. It is similar to the H-plasma-induced ESR signal shown in Fig. 4.2. Its spectral intensity is comparable to the signal at $g \approx 2.004$ of the deposited material and, surprisingly, the intensity also increases with the deposition time. At present, there is no clear understanding on how the PECVD process affects the glass surface and leads to the defects giving an ESR signal at $g \approx 1.99$.

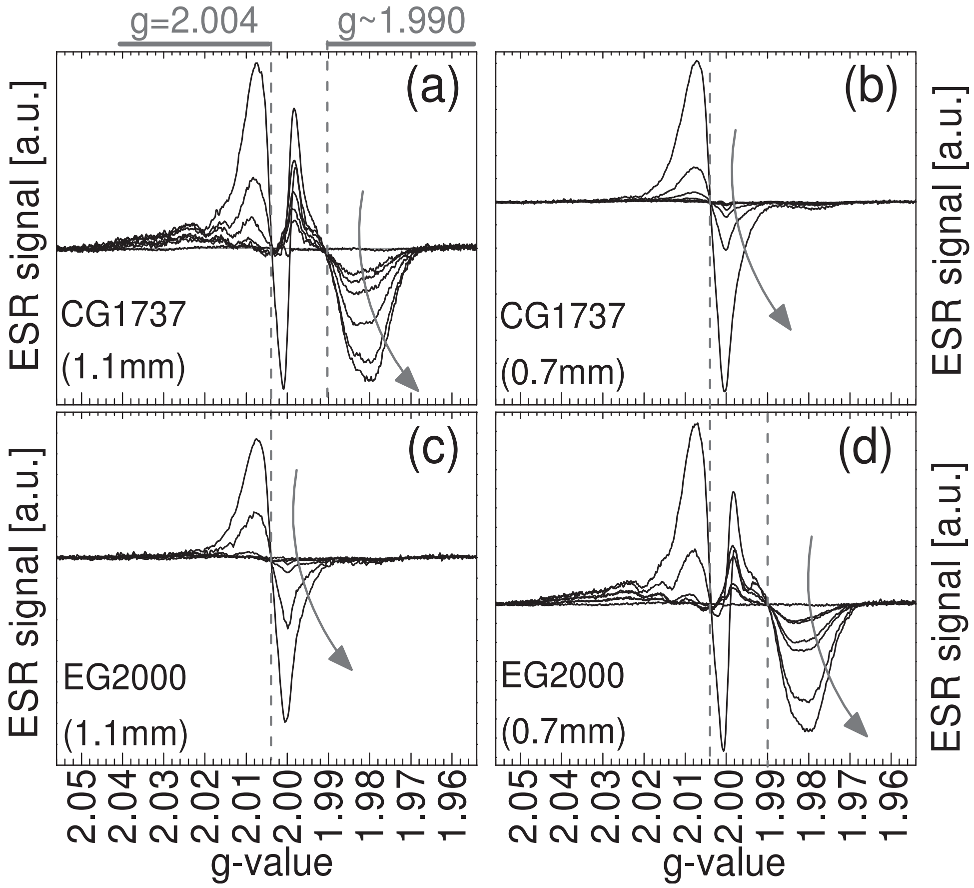

Figure 4.2 *ESR spectra of different glass substrates covered with very thin µc-SiO*$_x$*:H films deposited on. Arrows indicate the evolution of the spectra with increasing film thickness. All spectra were measured at 40 K and normalized to the surface area of the glass substrates.*

Taking the double integration values under the derivative ESR spectra over the whole range in Fig. 4.2, the surface spin densities (N_{Sf}) from those glass substrates covered with very thin μc-SiO$_x$:H films were calculated and summarized in Fig. 4.3. As the deposition time changes from 0 to 1280 s, N_{Sf} increases from 6.2×10^{14} to 3.5×10^{15} cm^{-2} for CG1737(1.1mm) shown in Fig. 4.3(a), from 1.1×10^{14} to 1.2×10^{15} cm^{-2} for CG1737(0.7mm) shown in Fig. 4.3(b), from 2.2×10^{14} to 1.0×10^{15} cm^{-2} for EG2000(1.1mm) shown in Fig. 4.3(c), and from 6.0×10^{14} to 3.0×10^{15} cm^{-2} for EG2000(0.7mm) shown in Fig. 4.3(d), respectively.

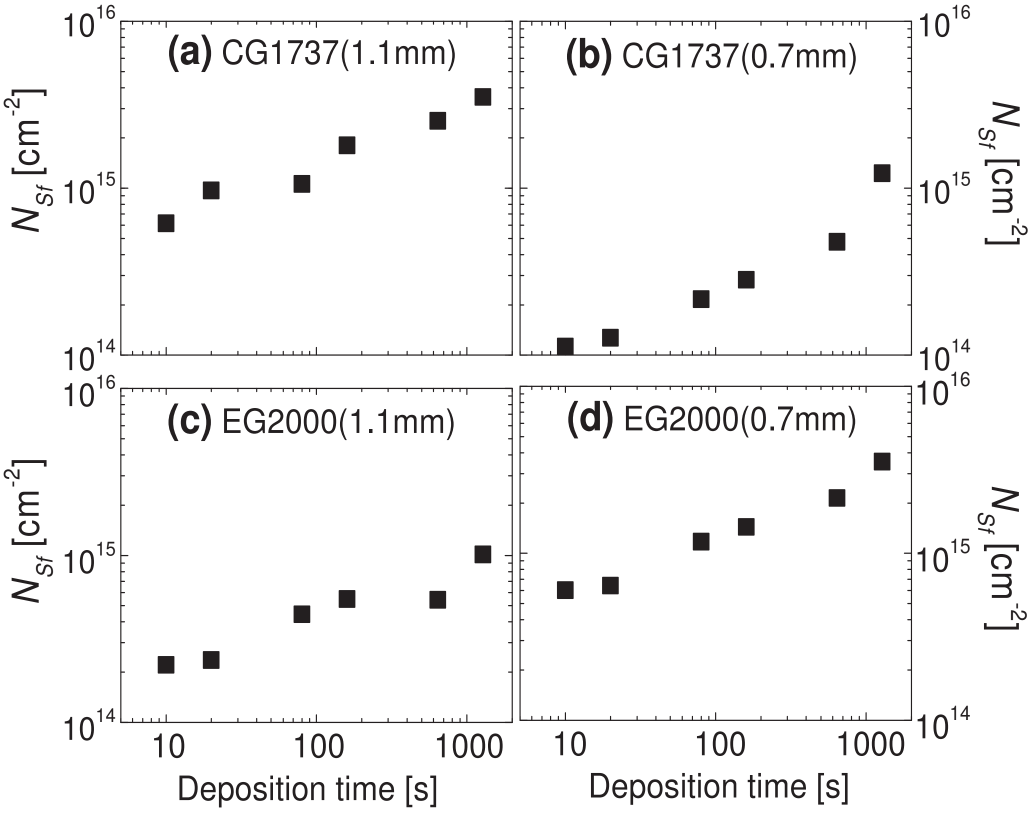

Figure 4.3 *N_{Sf} for different glass substrates covered with very thin μc-SiO$_x$:H films: (a) CG1737(1.1mm); (b) CG1737(0.7mm); (c) EG2000(1.1mm); (d) EG2000(0.7mm).*

Briefly, within the investigation range, when glasses are covered with very thin (0…128 nm) µc-SiO$_x$:H films, the surface spin density increases with the film thickness but not simply linearly as the film thickness increases. Note that this surface spin density evaluation includes signals both from the glass ($g \approx 1.99$) and also the µc-SiO$_x$:H film on it ($g \approx 2.004$).

In the PECVD process, as soon as the plasma is on, H plasma radicals start reacting with the glass surface resulting in the ESR signal at $g \approx 1.99$ until the glass surface is gradually covered with µc-SiO$_x$:H film. Therefore, N_{sf} from the glass probably increases with deposition time but not linearly. $N_{sf\,(\mathrm{glass})}$ may reach a saturation level after some time deposition.

On the other hand, as for the µc-SiO$_x$:H film on glass, to evaluated $N_{sf\,(\mu\mathrm{c\text{-}SiO}x\mathrm{:H})}$, one has to take into account both the growth rate and inhomogeneity of defect distribution Its contribution at $g \approx 2.004$ to the surface spin density keeps increasing with deposition time.

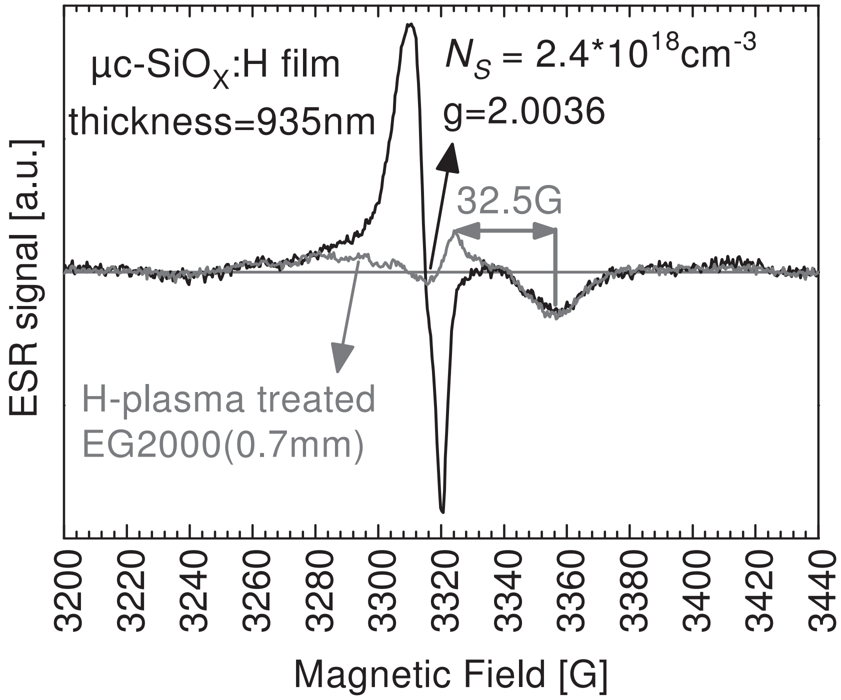

Figure 4.4 *Subtraction of the ESR signal of H-plasma-treated glass (red) from the ESR spectrum of µc-SiO$_x$:H film (black) on EG2000(0.7mm) glass substrate.*

For evaluation of the bulk spin density of µc-SiO$_x$:H, an example is shown in Fig. 4.4. The black line is the signal from µc-SiO$_x$:H (with g = 2.0036 and spin density of $N_S = 2.4\times10^{18}$ cm^{-3}), it was deposited on EG2000(0.7mm) with a thickness of 935 nm. ESR spectra were measured at 40 K. The red line is the signal from the glass EG2000(0.7mm) which has been treated by H-plasma for 5 min in the PECVD system. In order to eliminate the glass signals, the spectrum from H-plasma treated glass ($g \approx 1.99$) was scaled and matched the feature found at 3340 – 3380 G with the spectrum from µc-SiO$_x$:H film sample. Glass signals were subtracted before ESR evaluation of µc-SiO$_x$:H material.

4.2.2 Glass substrates covered with thick µc-SiO$_x$:H films

Fig. 4.5 displays the ESR spectra for CG1737(1.1 mm) glass treated with H-plasma for 5 min and covered with *n*-type µc-SiO$_x$:H films with a thickness of 20, 450 and 600 nm. All the spectra were measured at 40 K and normalized to the same surface area of the glass substrates.

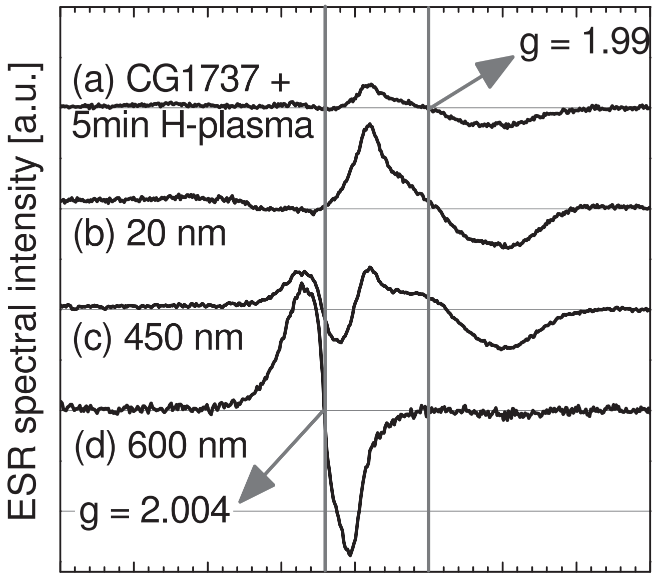

Figure 4.5 *Evolution of the ESR signal of µc-SiO$_x$:H on CG1737(1.1mm) with increasing film thickness of 20, 450 and 600 nm, compared to the H-plasma-treated glass.*

The spectrum corresponding to the sample with the thickness of 20 nm (Fig. 4.5(b)) is quite similar to CG1737(1.1mm) with 5 min of H-plasma treatment (Fig. 4.5(a)), only the intensity of the resonance at $g = 1.99$, which is assumed to come from the glass surface, increases after covering the glass with 20 nm μc-SiO$_x$:H. No signal from the μc-SiO$_x$:H material was found.

In Fig. 4.5(c), the μc-SiO$_x$:H film has a thickness of about 450 nm, the signal intensity at $g = 1.99$ does not increase further with thicker μc-SiO$_x$:H compared to Fig. 4.5(b). The signal at $g = 2.004$, which is believed to be from the silicon oxide material [Xiao2010(1)], its intensity increases with as the film is thicker. By subtracting the glass signal from the signal shown in Fig. 4.5(a), an ESR spin density (N_S) in the sample of about 1×10^{19} cm^{-3} was calculated.

Surprisingly, for the μc-SiO$_x$:H film with a thickness of 600 nm (Fig. 4.5(d)), the intensity of the signal at $g \approx 1.99$ is negligible compared to that of the signal at $g \approx 2.004$.

4.3 Summary and conclusions

Four kinds of glass substrates (Corning1737 and Eagle^{2000}, both with a thickness of 0.7 and 1.1 mm) have been treated with H-plasma for 5 min. ESR signals have been observed at $g \approx 1.998$ and $g = 2.014$, which are attributed to defect states on the glass surface, induced by the H-plasma in the PECVD process. These signals need to be taken into account for a correct data interpretation of materials covering the glass.

Thus, for ESR investigation of Si material and its alloys like silicon carbide and silicon oxide, a sufficient amount of spins is required. From the test measurements in this chapter, at least ~10^{16} spins are required in the films in order to be able to neglect the substrate signals.

Chapter 5: ESR investigation of a-Si:H and µc-Si:H powders

The application of hydrogenated amorphous and microcrystalline silicon (**a-Si:H** and **µc-Si:H**) in electronic devices, e.g. being used as both the sunlight absorber and doped layers in thin-film Si solar cells, is well known. A detailed understanding of the structural, electrical and optical properties of the material is essential for the improvement of device performance. ESR is a suitable technique which has proven to be useful and powerful in gaining microscopic information about the electronic states on disordered Si and its alloys.

This chapter starts with the necessity of preparation of a-Si:H and µc-Si:H powder samples for ESR measurements. Concerning the powder preparation processes, influences on the material crystallinity and/or ESR properties that probably arise from the substrate, contact of the material with the atmosphere and/or with liquids, *etc*., to investigate the correlation between the defect density and ESR-detected spin density in a-Si:H and µc-Si:H is an interesting topic.

5.1 Sample preparation: a-Si:H and µc-Si:H powders by PECVD

This section starts with a description of the necessity of a-Si:H and µc-Si:H powders for ESR measurements, followed by the selection of temporary substrates for deposition of hydrogenated thin film silicon with *plasma-enhanced chemical vapor deposition* (PECVD). Finally, the powder collection procedures are elaborated.

5.1.1 Necessity of a-Si:H and µc-Si:H powders for ESR measurements

It is commonly accepted that in a-Si:H and µc-Si:H, the dominant paramagnetic defect is the silicon dangling bond (Si-db) – unsaturated three-fold coordinated Si atoms. Si-dbs can be positively charged (D^+), neutral (D^0) or negatively charged (D^-) when they are occupied by 0, 1 or 2 electrons, respectively.

In intrinsic a-Si:H, only the neutral (D^0) Si dangling bonds (db) which distribute around the midgap are paramagnetic and can be detected by ESR. A *g*-value of $g = 2.0050 \sim 2.0055$ has been observed [Stutzmann1989; Street1991; Astakhov2009]. In intrinsic μc-Si:H samples, two resonances at $g \approx 2.0052$ and $g \approx 2.0043$ have been proposed [Finger1994; Finger1998; Lips2003]. Both of them are ascribed to db defect states. All these defect states in a-Si:H and μc-Si:H materials act as the recombination centers and/or trapping centers for excess charge carriers and may limit the efficiency of thin-film silicon solar cells.

For material research, a-Si:H and μc-Si:H films with a thickness of a few hundred nm to a few μm are usually deposited from the gas phase on various substrates such as glasses, ceramics, metals or plastics. These samples together with their substrate cannot always be used in a straightforward manner for ESR experiments for two reasons:

First of all, the dimensions of the substrate to be placed in the X-band ESR resonance cavity are limited to a few mm in width and 10 – 20 mm in length, particularly for experiment at low temperatures. Metallic or other lossy substrates, which would influence the microwave absorption of the materials, are ruled out from the very beginning in these experiments. On a 1 cm^2 glass substrate, the volume of a 1 μm thick Si film is 10^{-4} cm^3. With reasonable quality intrinsic a-Si:H or μc-Si:H, which has spin densities of 10^{15} – 10^{16} cm^{-3} [Finger1998; Astakhov2009], this results in a total amount of 10^{11} to 10^{12} paramagnetic states distributed over 10 G (peak-to-peak linewidth) for the dominant db defects, e.g. about $10^{10}-10^{11}$ spins/G have to be detected. A sensitivity of 10^9 spins/G at RT for super high Q (quality factor Q > 25000) ESR cavity has been achieved [Maier1997]. However, commercial X-band cavities (with Q = 3000 – 5000 at room temperature for non-lossy samples) have a detection limit of $10^{10}-10^{11}$ spins/G. Therefore the mentioned film sample on glass substrate has an ESR signal at the sensitivity limit of the system and cannot provide reliable measurements.

Additional problems in this case arise from the substrate itself which may have its own ESR active species that even at low concentration will contribute to the extremely weak signal from the film and make data interpretation difficult or maybe even worthless, e.g. the well-known E´ center in quartz and silica glass [Shendrik1985]. Such defects may exist in the substrate originally or may be created during the deposition process, at which reactive species such as hydrogen can etch the surface of the substrate.

A way to increase the sample mass is to deposit the film on a larger area and then to try to collect and condense the material into a smaller probe volume. For ESR measurements, the use of powder samples allows to place a larger amount of material in the center of the resonant cavity. This results in higher signal intensity and an improved signal-to-noise ratio. This approach has been used since long for thin film silicon materials, where typically metal foil is used as a temporary substrate such as Molybdenum (Mo) or Aluminum (Al).

However, it has always been argued that the material prepared in such a way may differ from material which is used for other investigations or which is implemented in devices like solar cells. In particular the removal of the material by an etching process or by mechanical force is of concern here. But also the possible influence of different substrates on the material growth and the resulting properties has to be considered. Different thermal and electrical properties of the substrate can affect the coupling to the heater, the glow discharge and growth process itself. In particular for μc-Si:H such a strong substrate dependence of the material growth has been reported in many studies [Kondo1996; Dirani2000; Bailat2002].

Briefly, a-Si:H and μc-Si:H material in the powder form is crucially necessary for cw-ESR investigation, and substrate dependence of ESR properties is an essential topic.

5.1.2 Temporary substrates: Al-foil, Mo-foil and ZnO-covered glasses

Considering the convenience and availability, we normally use the household Al-foil as the sacrificial substrate for ESR powder preparation. Sometimes, we also used Mo foil due to its convenience of powder collection. Meanwhile, for thin-film Si solar cell deposition, glasses which are covered with a transparent conductive oxide (TCO, e.g. Al doped ZnO denoted as 'ZnO:Al') layer, are used for the consequent deposition of hydrogenated Si layers. For the preparation of thin-film Si powder samples, ZnO-covered glass substrate is also used as a temporary substrate, and it therefore serves two purposes: (i) the deposition process can be done in standard configuration with glass substrates similar to solar cell deposition with the same thermal and electronic coupling of the substrate to the heater and the plasma and (ii) ZnO provides the same nucleation for a-Si:H and μc-Si:H as in the case of solar cells.

These three kinds of temporary substrates all have their own features for a-Si:H and μc-Si:H powder preparation:

- Mo-foil: With the size of 10 cm × 10 cm × 0.05 mm (thickness), the flat Mo metal foil is rigid enough to be directly placed in a metal frame for film deposition. When the as-deposited Si film has no strong adhesion to the Mo substrate, Si flakes can be easily peeled off and then collected by bending the foil. This dry treatment greatly shortens the exposure time of Si powder material to the atmosphere and avoids the wet etching process. For other types of Si films with high internal strain, especially for materials at the transition range of μc-Si:H to a-Si:H, the adhesion between Si films and Mo substrate may be too weak, which causes peeling off and loss of the Si film already in the deposition system before collection. On the other hand, for material with low deposition rate where only small sample thickness is available, or material with very good adhesion to the metal substrate, peeling of the material from the substrates is difficult. It should also be mentioned that the incorporation of Mo into a-Si:H, μc-Si:H, a-SiO$_x$:H, *etc*., with correspondent formation of donors or deep states has been reported with $g = 1.93$ and $H_{PP} = 50 – 70$ G [Stutzmann1991]. Therefore one should pay attention to a possible ESR signature of Mo impurities.
- Al-foil: The standard household Al-foil has a thickness of 13 μm, and it can be easily etched off in HCl acid. As thin-film Si usually has a good adhesion to Al-foil, the use of Al-foil as substrate overcomes the problem of losing material before collection like that of Mo substrate. Because Al-foil is quite soft, four pieces of glasses (2.5×10 cm^2) are wrapped with the Al-foil and placed in the metal frame (10×10 cm^2) for film deposition. Afterwards, Al is etched away with 12.5% HCl acid. After etching, the Si powder has to be filtered from the suspension and dried in ambient air before it can be collected and sealed in a quartz tube. Obviously this prolonged exposure time of the material to liquids (such as HCl and H_2O) and/or air is a disadvantage and possible influences on the material properties may occur. While removal of the substrate is easy in this case, the usage of the Al temporary substrates has some challenges including the mounting of the thin Al-foil in the deposition system, the unknown effects concerning contact to the substrate heater and finally the influence of the metallic substrate on the glow discharge and film growth.
- ZnO-covered glass: For thin-film Si solar cells, ZnO:Al is often used as the transparent conductive oxide (TCO) layer, on which other photovoltaic materials are grown subsequently. Using ZnO-covered glass as temporary substrate, the deposition geometry remains unchanged for development of cells and powder material preparation. Meanwhile, the disadvantage from

using the soft Al-foil as substrate can be avoided when using a rigid glass substrate. ZnO serves as a sacrificial layer and can be also removed with HCl acid. Because the ZnO is sandwiched between the glass and the Si film on it, a long-time etching (several hours) is needed. Like for the processing of the material on Al-foil, one will have to investigate possible effects of such an extended etching process on the material properties.

5.1.3 Thin-film µc-Si:H and a-Si:H deposition by PECVD

Hydrogenated Si films with structure covering highly crystalline µc-Si:H to a-Si:H were deposited by PECVD at a very frequency of 80 MHz. Details of the system set-ups can be found elsewhere [Vetterl2001]. Silane (SiH_4) and hydrogen (H_2) were used as source gases. The total flow of SiH_4 and H_2 were kept constant as 100 sccm. The silane concentration is defined as ratio of SiH_4 gas flow to the gas mixture as follows:

$$SC = \frac{[SiH_4]}{[SiH_4] + [H_2]}$$

By increasing SC, hydrogenated silicon with microstructure from highly crystalline µc-Si:H to a-Si:H can be prepared.

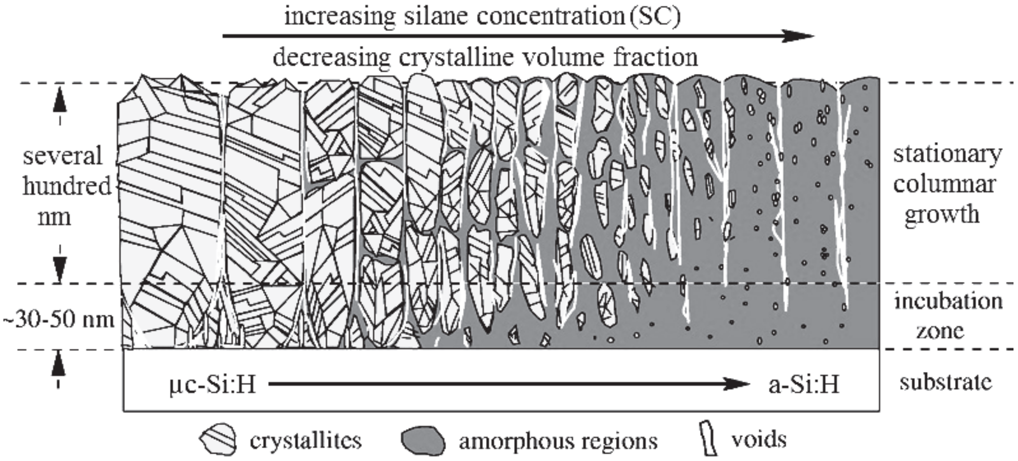

Figure 5.1 *A schematic microstructure model of hydrogenated silicon thin films. From the left to the right, the crystallinity is decreasing as material structure changes from highly crystalline µc-Si:H to a-Si:H. Figure taken from [Vetterl2000])*

As illustrated in the schematic diagram of Fig. 5.1, from the left to the right hand side, the material structure changes from highly crystalline μc-Si:H to predominantly a-Si:H. It is already well-known that such a structural transition is readily realized by increasing SC. All the other deposition parameters that would influence the properties of the resulting films were kept constant, e.g. the total gas pressure $p = 1.5\times10^3$ Pa, substrate temperature $T_S = 185$ °C, substrate – electrode distance d = 11 mm, deposition power density = 0.33 W/cm^2, deposition frequency = 80 MHz, and deposition power = 20 W.

Film thicknesses were in the range of 2 – 5 μm, yielding a powder mass between 40 – 100 mg for ESR measurements, e.g. film thickness = 2 μm, film area = 10×10 cm^2, density of silicon $\rho_{Si} = 2.33$ g/cm^3. Then the powder mass can be estimated as follows:

$$m = 2\ \mu\text{m} \times 100\ \text{cm}^2 \times 2.33\ \text{g/cm}^3 = 46.6\ \text{mg}$$

5.1.4 Intrinsic a-Si:H and μc-Si:H powder collection

For the powder preparation, thin films were deposited on three types of temporary substrates – Mo-foil, Al-foil and ZnO-covered glass. Consequently different procedures are required to collect the Si powders as follows:

- Mo-foil: After Si film deposition, the Mo-foil was bent to peel off the silicon flakes which were immediately sealed in quartz tubes filled with helium at a pressure $p = 5\times10^4$ Pa.
- Al-foil: The Al-foil, which is covered by the as-deposited Si film, was etched away with a 12.5% HCl solution leaving the Si material as a suspension of small flakes in the solution. Normally, a complete removal of Al-foil with a thickness of 13 μm is finished within 12 min. In order to investigate the etching effect on the material properties, Si flakes were also kept in the solution for different times varying from 12 min to 16 h.
- ZnO-covered glass: After Si film deposition, the 10×10 cm^2 glass substrates were cut into 2-cm wide strips and left in the 12.5% HCl solution overnight to separate the Si material from the glass.

In the cases of both Al-foil and ZnO-covered glass temporary substrates, after etching, the remaining Si flakes were filtered out of the fluid solution (filter paper Grade 595½: 4 – 7μm) and thoroughly rinsed with de-ionized water. Subsequently, the material was left in the air for about 16 hours until it has dried naturally. The mass of the dry powder sample is measured with a high-precision electronic scale (sensitivity: 0.1 mg) before it is filled into standard ESR quartz tubes (Wilmad Glass, Type 710-SQ-250 with an inner diameter of 3.9 mm). If consisting of very loosely packed flakes, the material was additionally crushed with a very thin glass rod to obtain comparable packing densities and filling heights (≤ 1 cm) in the tubes. Being connected to a vacuum system, the quartz tubes were evacuated and purged with 4 cycles of filling up with 1 bar He (purity: 99.999%) and pumping down to 10^{-3} Pa with a turbo pump. Finally a He atmosphere of 5×10^4 Pa is left in the tubes and they are sealed with a welding torch to maintain a defined environment for the sample powder. Material in this state is referred as the "*As-prepared*" state in the following text.

5.2 a-Si:H and µc-Si:H powders for ESR investigation – Role of the substrate and preparation procedures

Instabilities and metastable phenomena are reported for both a-Si:H [Staebler1977; Tanielian1982; Smirnov2006] and µc-Si:H [Vepřek1983; Finger2003; Dylla2003]. In particular, with recent emphasis on the study of µc-Si:H, which is grown at high hydrogen dilution and shows a pronounced porosity, the existence of crack-like voids in this material facilitates the diffusion of atmospheric gases (e.g. H_2O, CO_2, N_2, O_2, *etc.*) into the voids or the column boundaries structure. Adsorption and/or chemical reactions, e.g. oxidation, might change the surface potential and introduce band bending and therefore affect the electronic properties of the µc-Si:H material. Such effects are related to the whole preparation procedure from the film deposition, to the wet chemical etching of the temporary substrate, drying process and all the exposure processes of the sample to atmosphere. In all a careful control of the effects of different thin-film Si powder preparation procedures for ESR experiments remains of high interest.

The present section will discuss the influences of the three different methods for a-Si:H and µc-Si:H ESR powder sample preparation and to what extent possible influences on the thin film Si material properties can be avoided or taken care of.

Using Al-foil, Mo-foil and ZnO-covered glass as temporary substrates, hydrogenated Si powders were prepared and the structure ranges from highly crystalline µc-Si:H ($I_C^{RS} \geq 80\%$, SC = 2%), to material at the transition region between crystalline and amorphous growth further referred to as 'medium crystalline µc-Si:H' ($I_C^{RS} \approx 40\%$, SC = 5%), and finally to material which shows no crystalline phase in the Raman spectrum – a-Si:H ($I_C^{RS} \approx 0\%$, SC = 10%).

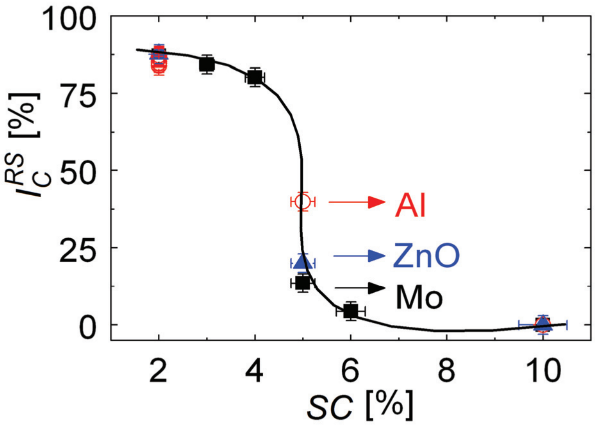

Figure 5.2 I_C^{RS} *vs. SC for samples deposited on Mo-foil, Al-foil and ZnO-covered glass. In the critical transition region (SC = 5%), corresponding substrates are indicated. Error-bars for Raman crystallinity and silane concentration are noted. The line is a guide to the eyes.*

In Fig. 5.2, I_C^{RS} is shown for samples prepared with different SC and on different substrates. The error-bars from the evaluation of material crystallinity (ΔI_C^{RS} = ±5%) and from the gas supply (ΔSC = ±5%, especially when the total gas flow is relatively small) are noted. A transition of the material from the highly crystalline µc-Si:H to a-Si:H is observed as SC changes from 2% to 10%. The material crystallinity I_C^{RS} decreases from above 80% to 0% with a fairly steep transition from highly crystalline to fully amorphous material between SC = 4% and 6%. The hydrogenated Si material in the moderate crystallinity region shows I_C^{RS} = 10 – 30%. Actually it is usually difficult to define a sharp transition 'point' between highly crystalline and amorphous growth. Even if keeping all the deposition parameters the same, to reproduce material with the same crystallinity in this critical transition region is very difficult.

Fig. 5.3 shows the ESR spectra of the materials prepared with different crystallinity (I_C^{RS} ≈ 80, 40, 0%, represents the highly crystalline µc-Si:H, moderate crystalline µc-Si:H and a-Si:H, respectively.) on different substrates (Mo-foil, Al-foil and ZnO-covered glass). Spectra in the same column represent materials of the similar microstructure; while in the same row represent the same substrates of Mo-foil, Al-foil and ZnO-covered glass.

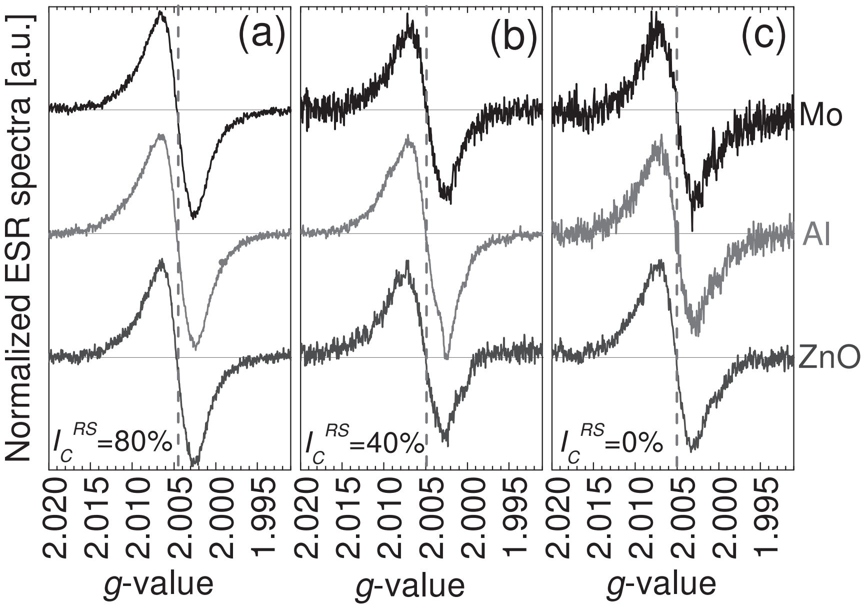

Figure 5.3 *ESR spectra of (a) highly crystalline μc-Si:H with* $I_C^{RS} \approx 80\%$ *, (b) moderate crystalline μc-Si:H with* $I_C^{RS} \approx 40\%$ *and (c) a-Si:H with* $I_C^{RS} = 0\%$*. Intensities of the spectra were adjusted in order to compare the lineshape.*

In Fig. 5.3(a), (b) and (c), all spectra show a slightly asymmetric single resonance, a peak-to-peak linewidth of H_{PP} = 6 – 8 G and a g-value increases from 2.0047 to 2.0051 as material changes from highly crystalline μc-Si:H to a-Si:H. Since the ESR measurement time is normally kept the same for all the samples, with the similar powder mass, samples of the lower spin density display a spectrum that is noisier than the high-spin-density ones. However, from the comparison between groups of the similar Raman crystallinity (I_C^{RS}), no substrate-dependence was observed.

Seemingly, the simplest fast and dry preparation procedure using Mo-foil as temporary substrate is the most attractive method unless the series of samples with a range of crystallinity is needed. But in this case one might face the severe problem of the material loss due to weak adhesion of the deposited material to the Mo substrate, especially when the sample has high internal stress, e.g. material at the μc-Si:H to a-Si:H transition region. Note that no ESR signals from Mo impurities with g = 1.92 ~ 1.93 [Stutzmann1991] were detected.

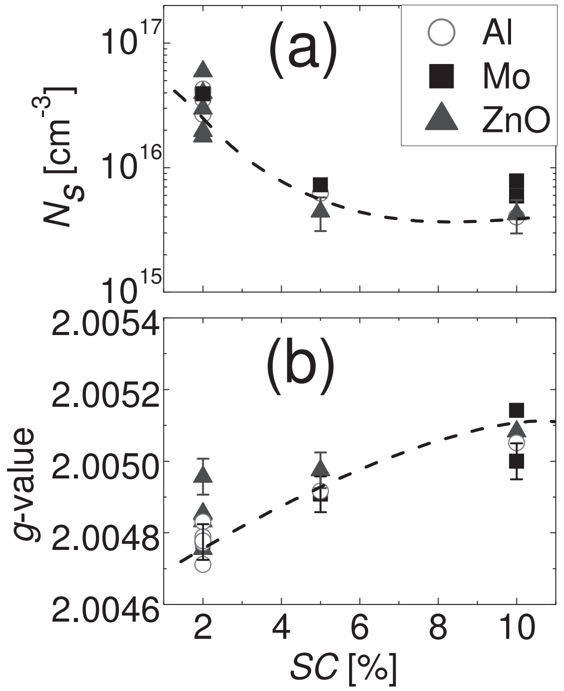

Figure 5.4 *(a) N_S and (b) g-value vs. SC for hydrogenated Si. All the ESR measurements were performed at RT. The evaluation error-bars for N_S (±15%) and g-values (± 0.00005) are noted.*

Fig.5.4 (a) shows the spin densities (N_S) for different hydrogenated Si powder materials prepared with three different preparation procedures within the range of SC = 2 – 10%. It was observed that the spin density decreases from 2 – 6×10^{16} cm^{-3} for highly crystalline μc-Si:H to 4 – 7×10^{15} cm^{-3} for a-Si:H. And these results are in agreement with previous work [Finger1998; Astakhov2009]. For a given crystalline volume fraction, the material from different substrates has similar N_S dependence on material crystallinity, rather than substrates.

Fig. 5.4(b) shows that as SC increases from 2% to 10%, *g*-value increases from 2.0047 to 2.0051, this variation of the *g* value indicates a change in the silicon-dangling- bonds defect structure or defect energy from highly crystalline μc-Si:H ($I_C^{RS} \geq 80\%$ when SC = 2%) to fully amorphous material ($I_C^{RS} = 0$ when SC = 10%). There is a considerable scatter in the g-value data for each substrate and no substrate dependence of *g*-value can be found.

In summary, three kinds of temporary substrates – Al-foil, Mo-foil and ZnO-covered glass were used for depositions of hydrogenated silicon films. Consequently, different post deposition processes were required for the Si powder detachment. It's known that the chemical nature and microstructure of the substrate on which Si films are grown plays a critical role in the resulting film microstructure, especially at the stage of nucleation and first 100 nm of the film [Kondo1996]. Therefore one might expect divergence in the properties of Si films prepared on these substrates.

Note that, however, there was no difference observed in the crystallinity and ESR properties of the Si:H powders prepared on Al-foil, Mo-foil and ZnO-covered glass. This may be attributed to a rather thick films (> 2 μm) used in the study which eliminates the effect of substrate so critical at first 100nm of the film. Therefore, all three substrates can be used and chosen according to the sample requirements. While Al and Mo foils are traditionally used as temporary substrates, the ZnO-covered glass is a new player which can be recommended.

When using ZnO-covered glass as temporary substrate, there are some suggestions to shorten the HCl-etching time for the future for ESR powder preparations:

1) Prepare less compact ZnO on glass substrates. The standard ZnO that is commonly used as the substrate for solar cells is prepared in a magnetron sputtering system at a temperature, pressure, discharge power and argon flow of 300 °C, 0.1 Pa, 1.5 kW and 100 sccm, respectively. Using higher sputtering pressure or lower temperature or lower power rate can get less compact ZnO film which is easier to etch off with HCl acid;
2) Use higher HCl-acid concentration to increase the etching rate;
3) Perform the etching at higher temperature, ultrasonic or catalysts for faster chemical reaction of HCl with ZnO and therefore increase the etching rate;
4) ZnO layer is sandwiched with glass at the bottom and Si film deposited on the top. The chemical reaction of HCl with ZnO will start from the glass edges. To laser scribe the Si – ZnO – glass stack, particularly from the glass side, instead of mechanical cutting, can increase the area of the cross section for chemical reaction and consequently faster the etching, without destroying the Si layers.

5.3 Metastability and instability effects in a-Si:H and µc-Si:H

It has been reported that atmospheric gas adsorption, absorption and/or oxidation affect the surface states, electron distribution and electronic transport processes in µc-Si:H [Vepřek1983; Finger2003; Dylla2004] and a-Si:H [Tanielian1982; Smirnov2006].

The atmospheric gas adsorption and absorption result in an increase of ESR dangling bond resonance, but they are reversible by annealing the samples in inert atmosphere (e.g. He or Ar) or in high vacuum at a temperature that is below the deposition temperature. The dissociative surface gases can be desorbed, and the ESR properties can be restored without changing the material microstructure. As is shown in Fig. 5.5(a), when annealing the highly crystalline µc-Si:H powder samples in He atmosphere, the ESR spectral intensity decreases strongly as the annealing process goes on, while the spectral shape always similarly keeps as a slightly asymmetric single broad line with a peak-to-peak width of $H_{PP} = 6 – 8$ G and the resonance center was shifted down to some lower values..

It is known that annealing samples under different conditions, such as at open air, O_2 or Ar atmosphere [Dylla2004], in vacuuminfluences conductivity and ESR in thin film siliocn. From Fig. 5.5(b) one can see that annealing samples in the open air or in the O_2 atmosphere [Dylla2004] leads to effects that are different from that of annealing µc-Si:H in He. Annealing µc-Si:H samples in the open air is believed to result in the oxidation effect, which consequently leads to excessive defects (as is shown in Fig. 5.5(b)) and these defects cannot be reversed simply by annealing processes. The ESR spectra were distorted by an addition of another component from the higher *g*-value region, not always a single broad line; and the comprehensive *g*-value which we defined as the cross-zero value was shifted towards higher values. Estimated from the whole annealing experiments in both the He atmosphere and open-air ambient, the corresponding spin-density and *g*-values are shown in Fig. 5.5(c) and (d), respectively.

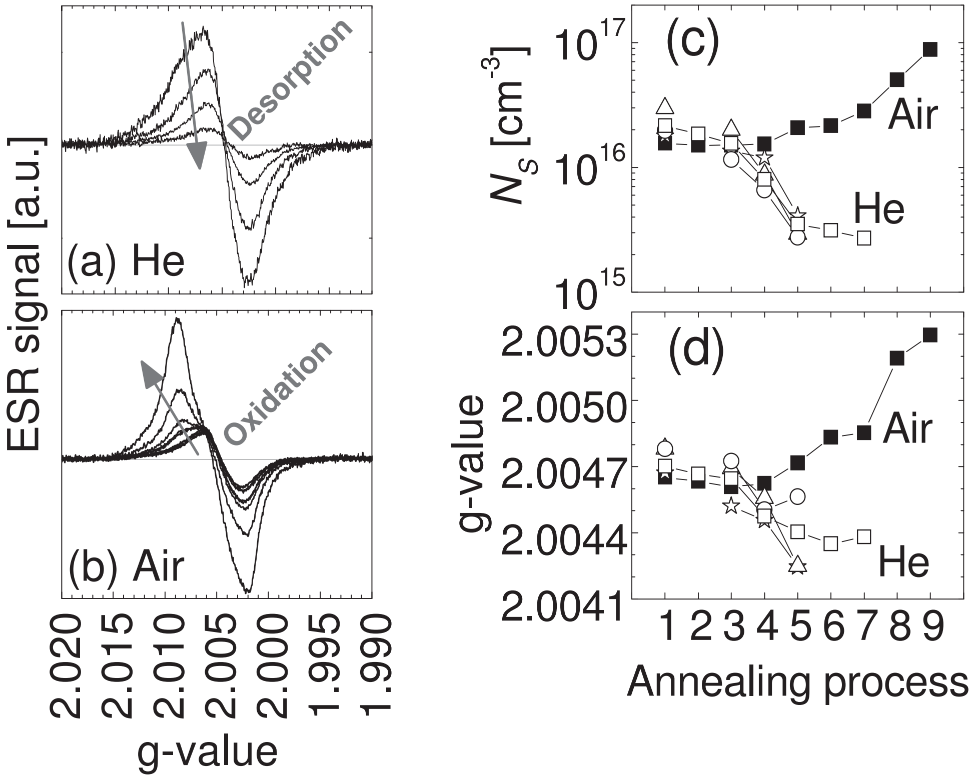

Figure 5.5 *ESR spectra with annealing processes in He (a) and open ambient (b) for highly crystalline μc-Si:H (* I_C^{RS} *> 80%). Arrows indicate the annealing processes as indicated as the X-axis in (c) and (d): 1 – As-prepared state; 2…5 – Annealed at 40, 80, 120 and 160 °C for 30 min; 6…9 – Annealed at 160 °C for 1, 2, 4 and 16 h. ESR was measured at RT, and after each step, spin density (c) and g-values (d) were calculated.*

As shown in Fig. 5.5(c), when annealing the μc-Si:H samples in He, the spin density N_S was decreased by one order of magnitude from 2×10^{16} cm^{-3} to be as low as 3×10^{15} cm^{-3}, and *g*-value was shifted from 2.0047 towards lower values of 2.0043. While in the case of annealing samples in the open-air ambient, N_S were increased from 2×10^{16} cm^{-3} up to a higher level of 10^{17} cm^{-3}, and *g*-value from 2.0047 up to some higher values of 2.0053. In addition, a further change in the ESR spectrum is observed upon prolonged exposure of the samples to air whichincreases the ESR spectral intensity and shifts its resonance centre towards the higher values.

These results are coherent with previous studies [Vepřek1983; Dylla2003; Finger2003; Dylla2004], in which the former effect (annealing in He atmosphere leads to lower N_S and smaller g-values) was attributed to the desorption of the gas molecules which stick to the surface of the material, and the latter was due to the oxidation in the open-air during the annealing processes.

All these adsorption, absorption and/or oxidation effects may take place during the sample preparation procedures, such as during the wet chemical etching of the temporary substrates or during the drying process in ambient air.

In the following section, the HCl-etching and atmosphere-related metastability and instability effects in μc-Si:H and a-Si:H will be discussed. Their reversibility and irreversibility are examined by an annealing sequence. Samples at different states are named as follows:

As-prepared: a-Si:H and μc-Si:H films were deposited on temporary substrates, made into powders by different consequent procedures and sealed in quartz tubes for ESR measurements. Samples at this states is named as 'as-prepared' states.

Annealed: After ESR measurements at the as-prepared state, samples were annealed step by step at temperatures of 40, 80, 120 and 160 °C for 30 min in the He atmosphere. After each step, ESR spectra were recorded subsequently both at room temperature and 40 K.

Exposed: The quartz tubes were cut open and the powder samples were exposed to the air ambient. After 24 h's air exposure, samples were resealed to the quartz tubes filling with He atmosphere for ESR measurements.

5.3.1 HCl-etching-related metastability and instability effects

In order to investigate the HCl-etching related metastability and instability effects, for thin films prepared at each silane concentration on Al-foil from the same deposition run has been divided into two parts: One part is etched in the standard way of 12 min, and the other part is left in the HCl acid for 16 h. Powder samples are collected in the standard way as described in Section 5.1.4.

Fig. 5.6 shows the ESR spectra for the powder samples of all these three morphologies – (a) a-Si:H ($I_C^{RS} = 0\%$ with SC = 10%), (b) moderate crystalline μc-Si:H ($I_C^{RS} = 40\%$ with SC = 5%) and (c) highly crystalline μc-Si:H ($I_C^{RS} = 85\%$ with SC = 2%). In each group of

Fig. 5.6(a), (b) and (c), ESR spectra were measured at room temperature and normalized by the same powder mass for a comparison of lineshape and spectral intensity.

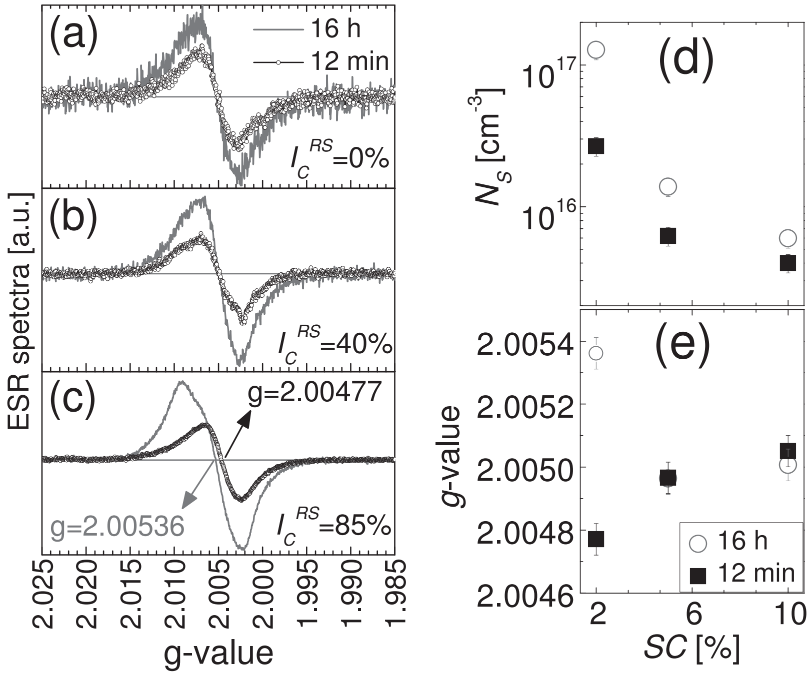

Figure 5.6 *ESR spectra of (a) a-Si:H (b) moderate crystalline and (c) highly crystalline μc-Si:H with 12 min's (black) and 16 h's etching (red). (d) N_S and (e) g-value vs. SC.*

Comparing the red lines in Fig. 5.6(a), (b) and (c) with the black lines, it has been observed that all the long-time etched (16 h) samples show higher spin densities than that of the samples etched for 12 min. The higher the material crystallinity is, the stronger the etching-induced ESR spectral intensity is. In the case of both a-Si:H (Fig. 5.6(a)) and moderate crystalline μc-Si:H (Fig. 5.6(b)), except for the signal intensity, virtually no difference in the ESR lineshape of samples due to long etching time was observed. But for the highly crystalline μc-Si:H (Fig. 5.6(c)), in addition to a pronounced increase of ESR signal which means an increase in spin density (N_S), a very noticeable change in the ESR lineshape and an increase of the effective *g*-value have been observed.

The corresponding ESR spin density and *g*-values are plotted versus etching time in Fig. 5.6(d) and (e). Long-time etching (16 h) results in an increase of the spin density and a shift of the average resonance center towards higher *g*-values. Especially for the highly crystalline silicon (SC = 2%), N_S increases strongly from 3×10^{16} to 2×10^{17} cm^{-3} , and due to the appearance of an additional signal with g > 2.005, the average *g*-value of the ESR spectra shifts from 2.00477 (HCl etching for 12 min) to 2.00536 (HCl etching for 16 h).

The duration of etching was systematically varied from 12 min up to 16 h to investigate the susceptibility of highly crystalline μc-Si:H (with $I_C^{RS} \geq 80\%$) to its exposure to air or liquids. Films were prepared in five deposition runs under identical settings of deposition parameters and etched with different etching times. To verify possible differences from run-to-run variations of the spin properties, in addition to these five samples, a sample from one run has been divided into four parts and etched with HCl acid for 12 min, 6 h, 14 h and 16 h. The results are summarized in Fig. 5.7.

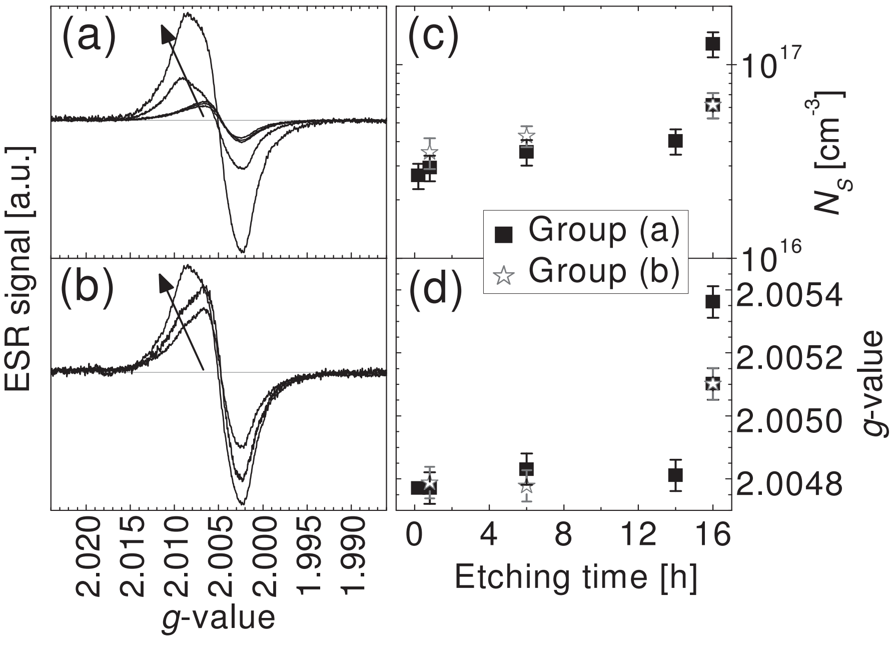

Figure 5.7 *Evolution of ESR spectra of highly crystalline μc-Si:H prepared in different (a) and same (b) runs with variation of the etching time. Arrows indicate the increase of the etching time.* N_S *(c) and g-values (d) vs. etching time.*

Fig. 5.7(a) shows the ESR spectra of highly crystalline μc-Si:H samples prepared with the same conditions and etched for different time in HCl. All the ESR spectra were measured at room temperature and normalized by the same powder mass. Spin density and g-values are shown in Fig. 5.7(c) and (d). Up to etching for 6 h, the spectra are similar with slight increase of the intensity as the etching process prolongs. With longer etching time (> 5 h), N_S abruptly increases from 3×10^{16} to 2×10^{17} cm^{-3} and g-values from 2.0048 to 2.0054, with an obvious change in the ESR lineshape.

Fig. 5.7(b) shows the evolution of the ESR lineshape with different etching times for a sample deposited in one run but divided into three parts for different etching times. The arrow indicates the increase of etching time. An increase in the resonance intensity and change in the lineshape were observed, very similar to the observation documented in Fig. 5.7(a). This is supported by N_S and g-value in Fig. 5.7(c) and (d), for which squares and stars refer to samples of group (a) and (b), respectively. Both groups show the same development of N_S and g-value. Long time etching leads to the appearance of an additional ESR signal at the range with g-value > 2.005, for which the source is still not clear.

Following the discussion of earlier studies [Vepřek1983; Finger2003; Dylla2004], the observed changes in the spin properties after prolonged exposure to the aqueous etching solution are correlated to the adsorption of H_2O or O_2 on inner surfaces in the highly crystalline μc-Si:H with its typical columnar and porous structures. Correspondingly one would expect that these effects are metastable and can be removed again by low temperature annealing, keeping $T_{Annealing} < T_{Deposition}$. Therefore, a highly crystalline μc-Si:H sample was stepwise annealed up to 160 ºC.

Fig. 5.8(a) shows the evolution of the ESR spectra with annealing steps applied to the sample etched for 16 h and sealed in He-filled quartz tube after drying. The spectra were recorded after each annealing step of 40, 80, 160 ºC for 30 min, then at 160 ºC for 1, 2, 4, and 6 h. Fig. 5.8(b) shows N_S (circles) and g-values (stars) evaluated from the spectra in Fig. 5.8(a). By annealing the samples at 80 °C, a recovery of N_S and g-value had been observed. Considering the error-bar of N_S (±15%) and g-value (±0.00005), at 160 °C for 1 h, both values recover fully to the level which is found for the material with the minimum etching time of 12 min. With further annealing at 160 °C, N_S is further reduced below this level while the g-value does not shift further. Going beyond an annealing time of 2 h at 160 °C does not result in any further changes in the ESR properties but N_S for highly crystalline μc-Si:H are exceptionally low (10^{16} cm^{-3}).

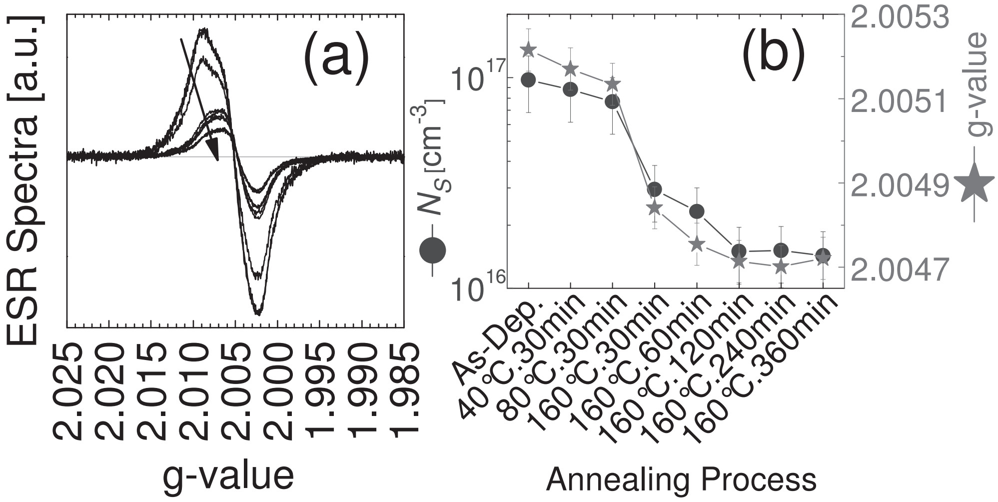

Figure 5.8 *(a) Evolution of the ESR spectra for a highly crystalline μc-Si:H (* I_C^{RS} *> 80%) powder sample. Arrow indicates the annealing processes. (b) Dependence of* N_S *(dots) and g-values (stars) on the annealing process. ESR spectra were measured after each annealing step.*

In summary, the effect of Mo-, Al-foil and ZnO-covered glass substrates and correspondent recovery procedures on the properties of ESR powder samples has been investigated for a-Si:H and μc-Si:H films. Under conditions of restriction of the duration of all critical substrate removal steps: air exposure, HCl etching, to the necessary minimum very similar ESR results for all three substrates: Mo, Al and ZnO-covered glass have been observed. No substrate-dependent differences have been found by ESR and Raman measurements. Mo-foil can be recommended to be the most appropriate substrate for convenience of a-Si:H and μc-Si:H powder collection. While in some cases, especially for samples with the crystallinity at the transition region between highly crystalline and amorphous silicon, material has bad adhesion to the Mo substrate, Al-foil should be used.

Significant extension of the HCl etching time of the Al substrate to 16 h led to a considerable increase in intensity of ESR spectra of all material (from highly crystalline μc-Si:H to a-Si:H). The magnitude of the instability changes has been found to be dependent on the material microstructure. The effect has been the most pronounced in highly crystalline μc-Si:H where distortion of ESR spectra has been found in addition.

A proper annealing procedure eliminates the HCl-etching induced changes in the ESR spectra. Together with N_S and g-values, the effect of prolonged etching seems to be similar to the reversible atmospheric metastability and instability effects investigated earlier in μc-Si:H with ESR [Vepřek1983; Finger2003; Dylla2004].

Annealing μc-Si:H powder samples in He atmosphere at a temperature that is below the deposition temperature could remove the surface atmospheric adsorption without defect creation by breaking any bonds like Si-Si or Si-H. With reasonable annealing time, e. g. 160 °C for 1–2 h, the ESR spin density of dangling bonds in μc-Si:H was decreased from 10^{17} cm^{-3} to a stable value of 10^{16} cm^{-3}, and g-value from 2.0052 to 2.0047. Further annealing did not lead to further change in N_S and g-values.

Assuming that these changes in the ESR properties – spin density, g-values and lineshape are related to the adsorption of atmospheric gases in the open air or the contact with the water during the HCl-etching process, annealing in vacuum would help to desorb these gases or water and restore the ESR properties. While exposing them to the open air would restore the samples to the initial states. And this is the main topic of the next section.

5.3.2 Atmosphere-related metastability and instability effects

A four-step sequence has been used to investigate the atmosphere-related metastability and instability effects in a-Si:H and μc-Si:H powder samples:

1) *As-Prepared*: Powder samples were prepared in the standard preparation process and sealed in quartz tubes in He atmosphere;
2) *Annealed. I*: Samples were sealed in the tube at 160 °C for 30 min;
3) *Air-Exposed*: Opening the tube, exposing the material to ambient air for 24 h, and then sealing in the tube with He again;
4) *Annealed. II*: Second annealing in the tube at 160 °C for 30 min.

ESR spectra have been taken after each treatment step.

The evaluated N_S is shown in Fig. 5.9 for different types of substrates and sample crystallinity. Each point is an average of spin density measured on several identical samples.

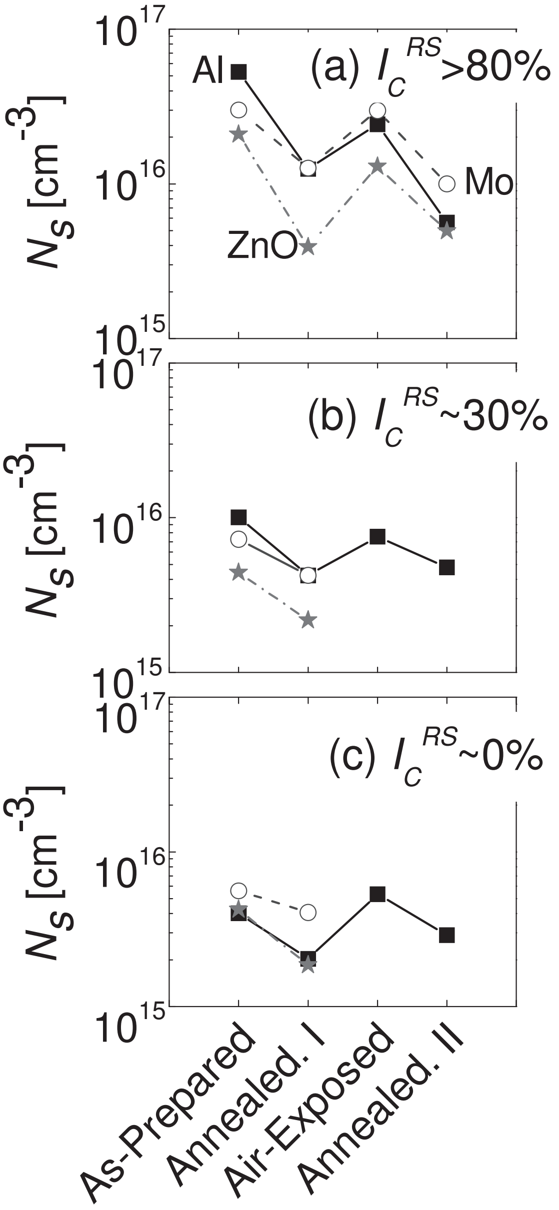

Figure 5.9 *Dependence of ESR N_S with the treatment steps for (a) highly crystalline µc-Si:H (b) moderate crystalline µc-Si:H (c) a-Si:H. Different symbols represent samples deposited on different substrates (Mo-, Al-foil and ZnO). Lines are guide for eyes.*

Initially highly crystalline μc-Si:H (Fig. 5.9(a)) has an average N_S of 2–5×10^{16} cm^{-3} with a tendency for higher values in the samples prepared on Al and lower values for the ones on ZnO. Annealing decreased N_S to be almost five times below the initial value for all types of substrates. After air-exposure and repeated sealing Ns increased up to 1–3×10^{16} cm^{-3}, a little below the initial state but considerably higher than annealed state. After the second annealing step, N_S was restored to the same level after the first annealing step.

Considering the very long exmepriment period, in order to reduce the number of measurements for moderately crystalline and amorphous samples only the samples deposited on Al have been exposed to the entire four steps procedure while others were not exposed to air after the first annealing.

In Fig. 5.9(b) and (c), N_S in both moderately crystalline and amorphous material changes with the sample treatment qualitatively in the same way as in highly crystalline material in Fig. 5.9(a) but with smaller amplitude. In Fig. 5.9(b) as-prepared N_S in moderately crystalline μc-Si:H is within 5–9×10^{15} cm^{-3}. In Fig. 5.9(c) N_S in a-Si:H is around 5×10^{15} cm^{-3} at both the as-prepared and air-exposed states. In both cases N_S is reduced after annealing by around 2.5 times.

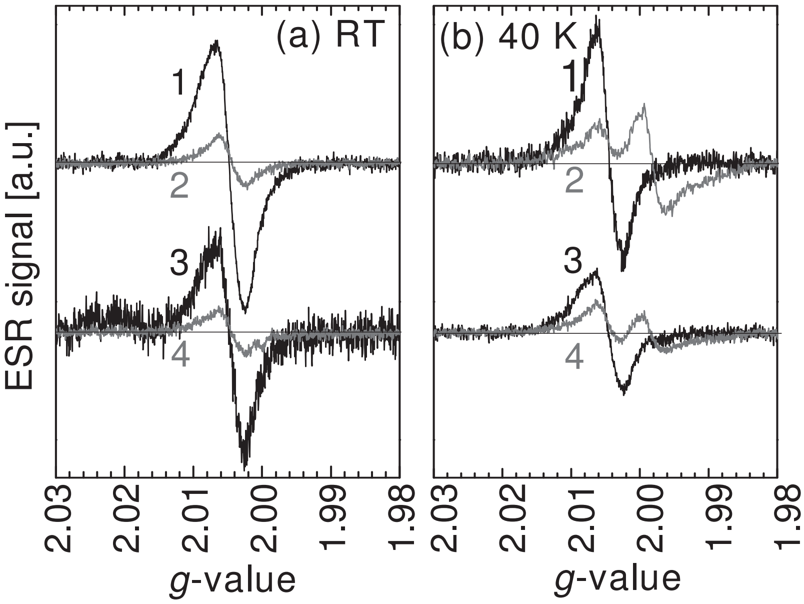

Figure 5.10 *ESR spectra measured at RT (a) and 40 K (b) for the highly crystalline μc-Si:H powder at sample states of: 1 As-prepared; 2 Annealed.I; 3 Air-exposed; 4 Annealed.II*

The biggest effect of the annealing and air exposure was observed in the highly crystalline sample. The example of ESR spectra taken at every of four steps in this material at room temperature is given in Fig. 5.10(a). The spectra show typical μc-Si:H slightly asymmetric single resonance with a peak-to-peak width of H_{PP} = 7 G attributed to dangling bonds (db). There were no changes in the lineshape or central resonance position detected during the treatment sequences. Only the spectral intensity of the resonance measured at room temperature has been changed with annealing and air exposure.

In Fig. 5.10(b) ESR spectra measured at 40 K are shown for the same sample and the same treatment as in Fig. 5.10(a). Here we see that air exposure result in changes of both the intensity and the shape of the ESR spectra. At the as-prepared state, the ESR spectrum is a single line with g = 2.0047 attributed to db. After annealing the resonance appeared to include two components: (i) weakened db-resonance at g = 2.0047 and (ii) newly emerged CE resonance at g = 1.998 commonly attributed to the conduction band tail/ extended states. After the next step of air-exposure the shape of the resonance returns to a single db-related component observed at the as-prepared state. The intensities of components of spectra 2 and 3 in Fig. 5.10(b) have been evaluated with a simple deconvolution procedure with use of pure db and pure CE resonances observed in the intrinsic and heavily *n*-type doped highly crystalline μc-Si:H. The results of deconvolution are compared to the intensity of the db-resonance measured at RT in Fig. 5.11.

Fig. 5.11 shows the dependence of the ESR spin density on the sample treatment processes for highly crystalline μc-Si:H powder using Al-foil as temporary substrate. Fig. 5.11(a) displays the variation of db-related N_S at room temperature, from 1–2×10^{16} cm^{-3} at the as-prepared and air-exposed states to 3×10^{15} cm^{-3} at the annealed states. At 40 K, in Fig. 5.11(b) one could find the similar fluctuation of N_S for the db resonance. Result shown in Fig. 5.11(c) reveals that nearly no CE resonance contribution was observed at both the as-prepared and air-exposed states; while CE was found prominent at the annealed states to be 3×10^{15} cm^{-3}, counting half of the spectral intensity.

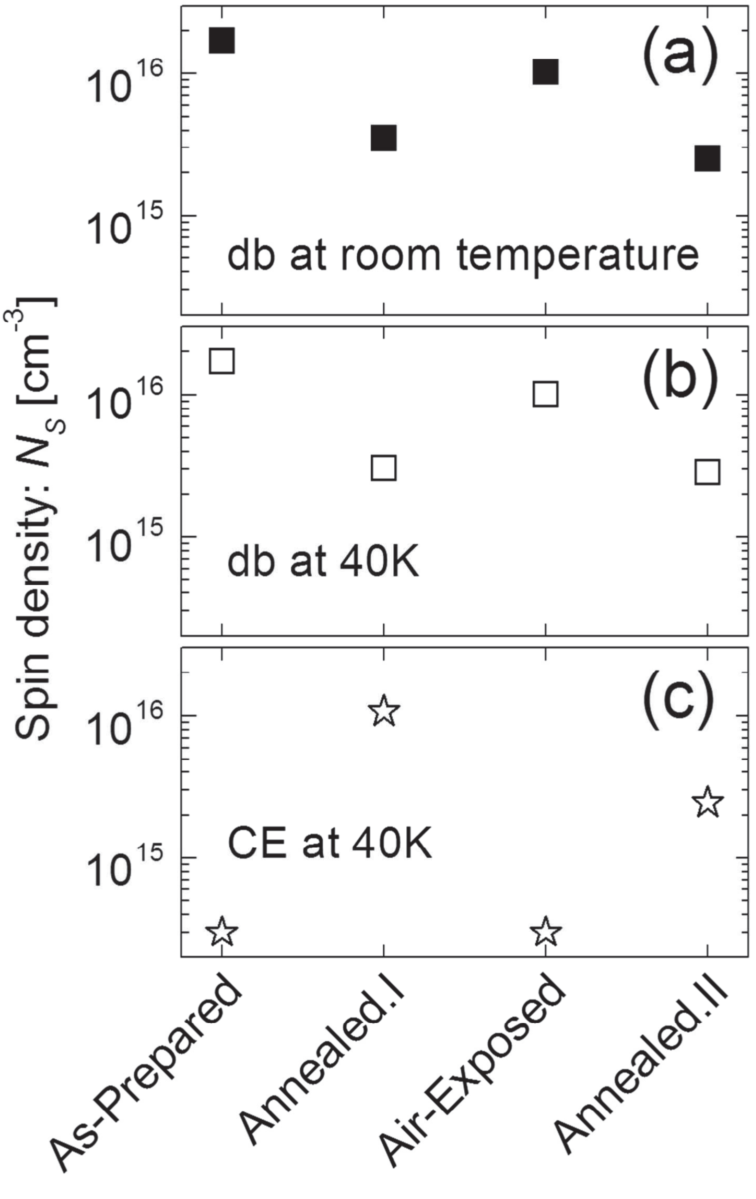

Figure 5.11 *Spin density after different treatment steps calculated from the spectra presented in Fig. 5.10. (a) N_S corresponds to db resonance at RT and individual contributions of (b) dangling bonds and (c) CE resonance at 40 K.*

5.3.3 Discussion: Determination of defect density in a-Si:H and µc-Si:H from ESR spin density

From all the above results, one could see that during the preparation of ESR samples of a-Si:H and µc-Si:H the material is exposed to air and in some cases aqueous solution. Therefore atmosphere – related metastability and instability effects are expected to affect the electronic properties of the material and consequently the density of the paramagnetic defects observed in ESR experiment. The metastability and instability effects may be reversible with annealing in vacuum or inert gas atmosphere. Therefore ESR measurements taken after air exposure and after annealing in inert atmosphere provide a way to examine possible metastability and instability effects.

The spin density of the dangling bond resonance monitored throughout the four steps procedure of preparation – annealing – air exposure – annealing has been found to be different. These variations are most obviously observed in the most crystalline samples and may reach a factor of 10. The spectra taken at 40 K in these samples after annealing contain a considerable portion of the CE resonance attributed to the conduction band tail states which is an indication for a Fermi level shift towards the conduction band as shown in Fig. 5.12.

It has been reported that µc-Si:H without intentional doping exhibits a slight *n*-type character [Finger1994; Jadkar2000], the Fermi level position is slightly above the midgap and close to the conduction band tail. Due to the adsorption of atmospheric components (e.g. H_2O, O_2 and/ or N_2) on the material surface, the *as-prepared* µc-Si:H material shows a band bending as Fig. 5.12(a) illustrates.

It is believed that annealing µc-Si:H at 160 °C in the He inert gas atmosphere removes the adsorbed atmospheric components from the material surface, effectively E_F is much closer to the conduction band tail at the *annealed* state (as is shown in Fig. 5.12(b)) than at the *as-prepared* state. This is confirmed with the observation of CE resonance at 40 K (Fig. 5.10(b)) at the annealed state and it is in good agreement with the conductivity observations [Smirnov2006].

Exposing the µc-Si:H material to the open air leads to the atmospheric adsorption. The ESR spectrum, the spin density and *g*-value are similar to the *as-prepared* state. The effective shift of the Fermi level closer to the midgap is expected to provide single occupation for the majority of the db states and N_S is believed to be closely related to N_D. After annealing and desorption of the adsorbed species the distribution of the db charge states returns to the known "slightly *n*-type character" of undoped μc-Si:H. In this case a portion of the singly occupied db states becomes doubly occupied, invisible for ESR, and we observe reduction in N_S after annealing. The second run of air exposure – annealing shows qualitatively the same ESR picture.

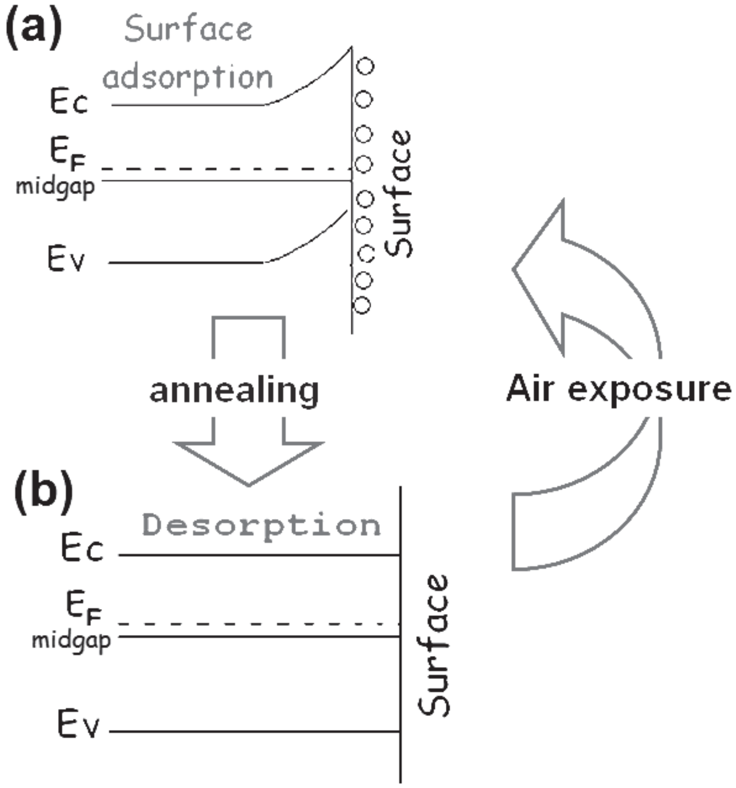

Figure 5.12 *Band diagram showing how the annealing – air exposure – annealing process changes the occupation of band tail states and the position of Fermi level in μc-Si:H.*

Atmosphere – related metastability and instability effects may introduce band bending which results in change in the conductivity most pronounced in the highly crystalline μc-Si:H [Smirnov2006]. For ESR measurements the band bending is important because of recharging of defect states and correspondent variations in N_S attributed to dbs. Appearance of the signals related to the tail states in the resonance is an evidence for the shift of E_F in either direction away from the midgap. Correspondent recharging of the db states implies that the fraction of the D^0 charge states will decrease and N_S cannot be considered as a good measure for N_D.

Taking all these facts together with the ESR observations, we attribute the variations of N_S to the recharging of the db states but not a variation of the density of these defects.

The preparation – related metastability and instability effects are considered to be very important for the N_S determination in μc-Si:H, especially in highly crystalline μc-Si:H. It is important to underline that N_S measured in the defined annealed sample state underestimates the db density while in the undefined aged state after the air exposure N_S represents the density of db more adequately. The problem is critical for highly crystalline μc-Si:H ($I_C^{RS} \geq 80\%$) where the difference in N_S between annealed and aged state may reach a factor of 10. For moderate crystalline μc-Si:H ($I_C^{RS} \approx 30\%$) and a-Si:H the influence of the preparation related air exposure is not as strong as that of highly crystalline μc-Si:H and makes up about factor 2.

Interestingly, the spin density appears to be a good measure of N_D in the “aged” state of the sample, after exposure to air during powder preparation. On the other hand if the atmospheric species have been removed by annealing the spin density may underestimate N_D.

5.4 Summary and conclusions

In this chapter, three different powder preparation methods were firstly introduced in detail. Mo-foil, Al-foil and ZnO:Al-covered glass were used as temporary substrates.

Being in contact with the HCl acid liquids or atmosphere for too long a time (e.g. 16 h), hydrogenated Si materials especially those highly crystalline ones would suffer from the metastability and instability effects. The HCl-etching related and the atmospheric adsorption would be reversed by annealing samples in the closed He atmosphere, while annealing at open ambient leads to atmospheric oxidation which could not simply be reversed by annealing.

It was found that N_S in μc-Si:H at aged states (e.g. after preparation or air exposure) is higher than in the annealed state. The variation of db resonance intensity is related to the recharging of the db-states due to adsorption of atmospheric species during sample preparation. N_S in the degraded state represents N_D more adequately than in the annealed state.

Chapter 6: ESR investigation of µc-SiC:H

Using hot-wire chemical vapor deposition (HWCVD), µc-SiC:H had been successfully produced at low deposition temperatures (T_S < 400 °C) on cheap glass substrates [Klein2005; Dasgupta2008; Huang2008; Chen2009] and used as the window layer in *n*-side-illuminated thin-film Si solar cells with *n–i–p* configuration (layer sequence µc-SiC:H *n*-layer/ µc-Si:H *i*-layer/ µc-Si:H *p*-layer) [Huang2007; Finger2009; Chen2009; Chen2011; Chen2012]. *P*-type doping with Al had also been realized [Chen2010(1); Chen2010(2)].

This chapter describes the preparation of µc-SiC:H by HWCVD. Deposition parameters such as the monomethyl-silane concentration (c_{MMS}), the filament and substrate temperature (T_F, T_S), the deposition pressure (p), and the Al-doping ratio (p_{TMAl}/p_{MMS}) were varied to obtain materials for window layers in thin-film Si solar cells. This work focuses on the ESR investigation and the correlation between ESR, and structural, electrical and optical properties of both *n*-type and *p*-type µc-SiC:H films.

6.1 Preparation of nominally undoped µc-SiC:H by HWCVD

Nominally undoped µc-SiC:H thin films were prepared by HWCVD. Details of the set-ups of this deposition system can be found elsewhere [Klein2003].

Monomethyl-silane (5% SiH_3CH_3 diluted in H_2, MMS for short) and pure H_2 are used as the precursor gases. Deposition parameters were varied as follows:

(1) Monomethyl-silane concentration: c_{MMS} = 0.3 – 2%, it is defined as the ratio of the gas flow of MMS to the total gas flow: $c_{MMS} = [MMS]/([MMS]+[H_2])$

(2) Filament temperature: T_F = 1750 – 2200 °C

(3) Substrate temperature: T_S = 200 – 550 °C

(4) Deposition pressure: p = 2 – 75 Pa.

μc-SiC:H films were deposited on glass substrates for ESR, electrical dark conductivity (σ_D), PDS and SIMS measurements. For infrared absorption measurements, films were deposited on double-side polished c-Si wafers. Infrared spectra were measured with a commercial Nicolet FTIR spectrometer over the range of 400 – 4000 cm^{-1} at room temperature. The film crystallinity (I_C^{IR}) can be estimated. Paramagnetic states have been investigated by conventional continuous wave X-band ESR spectrometer in the temperature range of 10 – 300 K. σ_D was measured at room temperature in a high vacuum ($p < 10^{-3}$ Pa) after annealing at 160 °C. PDS was used to determine the optical bandgap and absorption of free carriers and/or bandgap defects. Impurity and doping concentrations were measured by SIMS.

Note that all ESR measurements are performed on thin films with a thickness of 50 – 420 nm. For some thin film samples that did not have a sufficient amount of spins (e.g. low spin density, small amount of material), ESR measurements suffered from low signal-to-noise ratios and/or background signals of the glass substrates. The glass signals were subtracted in the way as described in Chapter 4. For more detailed ESR investigation, μc-SiC:H powders were prepared as described in Section 5.1.

6.2 ESR investigation of nominally undoped μc-SiC:H thin films

In order to obtain highly crystalline, highly transparent and highly conductive μc-SiC:H for application in thin-film Si solar cells, deposition parameters like monomethyl-silane concentration (c_{MMS}), substrate temperature (T_S), deposition pressure (p)and filament temperature (T_F) were adjusted and optimized. In the following section, their influence on the thin film crystallinity, electrical conductivity, and ESR spectra will be discussed.

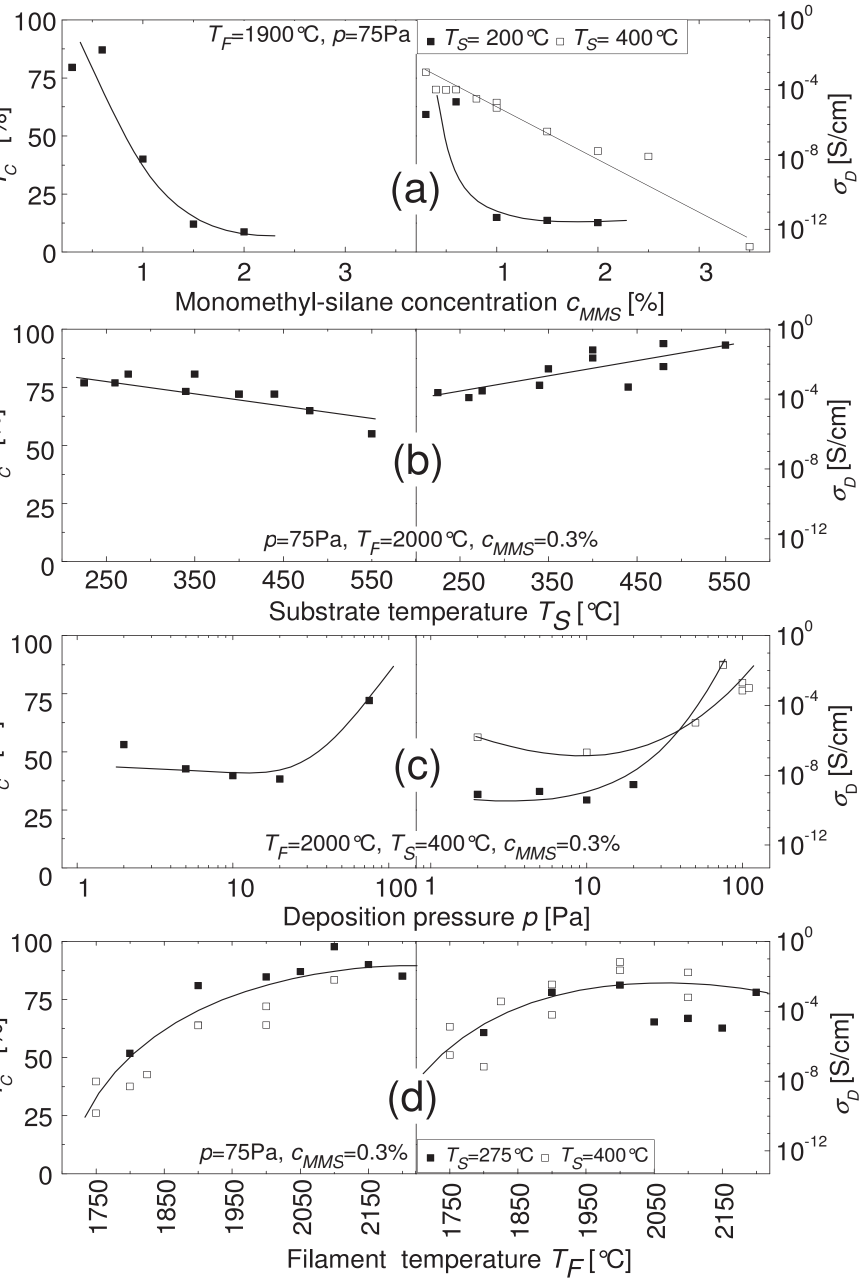

Figure 6.1 *Dependence of I_C^{IR} and σ_D on (a) c_{MMS}; (b) T_S; (c) p; (d) T_F for μc-SiC:H films. Constant deposition parameters in each series are labeled. Lines are guides for the eye.*

Fig. 6.1(a) shows the dependence of I_C^{IR} and σ_D on the monomethyl-silane concentration (c_{MMS} = 0.3 – 2%). The increase of c_{MMS} results in a reduction of the μc-SiC:H film crystallinity from $I_C^{IR} \approx 80$ to 10% as observed by the Infrared spectroscopy, and this finding is in agreement with the results from transmission electron microscopy (TEM) measurements [Klein2006]. This structural transition results in the reduction of σ_D by 7 orders of magnitude from 10^{-5} to 10^{-12} S/cm with increasing c_{MMS}.

Fig. 6.1(b) shows the dependence of I_C^{IR} and σ_D on the substrate temperature (T_S = 260 – 550 °C). As T_S increases, I_C^{IR} is kept at a high level between 77% to 55%, whereas σ_D increases slightly by 3 orders of magnitude from 10^{-4} up to 10^{-1} S/cm. The finding of an increase in σ_D on T_S is consistent with previous work [Dasgupta2008(2)], there TEM micrographs showed that the gross structural properties of the films remain nearly unaltered with change of T_S, the structure of these SiC thin films is excluded to be the reason for the increase in σ_D, but impurities and crystalline defects such as stacking faults in these materials are speculated.

Fig. 6.1(c) shows the influence of the deposition pressure (p = 2 – 75 Pa) on I_C^{IR} and σ_D for *n*-type μc-SiC:H thin films prepared at T_F = 2000 °C, T_S = 400 °C and c_{MMS} = 0.3%. When p is below 20 Pa, the film crystallinity is nearly constant at $I_C^{IR} \approx 40\%$. At p = 75 Pa, I_C^{IR} increases to 72%. A similar trend is found in σ_D – it is constant at 10^{-9} S/cm when p is below 20 Pa and increased to a high level of about 10^{-2} S/cm for the highest crystallinity.

Fig. 6.1(d) shows the influence of the filament temperature (T_F = 1750 – 2200 °C) on I_C^{IR} and σ_D. Keeping the pressure p = 75 Pa and the MMS concentration c_{MMS} = 0.3% constant, two series of samples were compared by varying T_F from 1750 to 2100 °C. The crystallinity covers a wide range from $I_C^{IR} \approx 25\%$ to a highly crystalline level of $I_C^{IR} > 90\%$. σ_D rises from 10^{-6} up to 10^{-1} S/cm as the material becomes more crystalline.

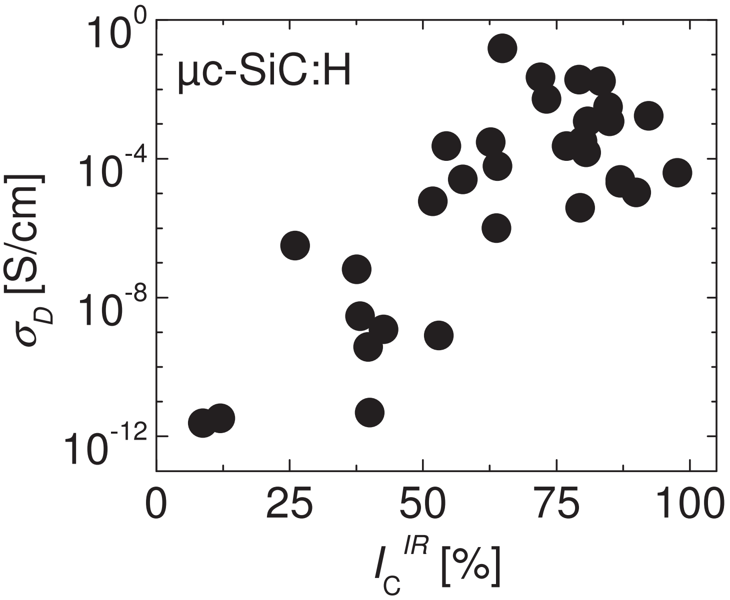

Figure 6.2 C*onductivity σ_D vs. crystallinity I_C^{IR} for nominally undoped μc-SiC:H thin films.*

In Fig. 6.2, the electrical conductivity (σ_D) is plotted as a function of the film crystallinity (I_C^{IR}). σ_D increases by more than 10 orders of magnitude from 10^{-12} S/cm for low-crystallinity μc-SiC:H to around 0.1 S/cm for material with high crystallinity ($I_C^{IR} > 50\%$). All these samples were nominally undoped, but $\sigma_D > 10^{-4}$ S/cm is as high as in N-doped SiC crystals [Silva2006].

The concentration of impurities (e.g. nitrogen and oxygen) was measured with SIMS in a set of samples prepared with $T_S = 200 - 550$ °C [Finger2009]. It was found that [N] almost keeps constant at 10^{19} cm^{-3}, [O] slightly increases from 10^{19} to 10^{20} cm^{-3}. And the ESR spin density was found to be $N_S = 10^{18}$ to 10^{19} cm^{-3}.

Considering the possible hopping conductivity from electronic transport via phonon-induced tunneling of electrons between localized states which are randomly distributed in energy and position, for this T_S series, the conductivity of these nominally undoped μc-SiC:H samples was measured in the temperature range of room temperature (~ 25 °C) to 160 °C. When plotting the natural logarithm $\ln\sigma(T)$ as a function of $1/k_BT$ (in the unit of eV^{-1}), $\ln\sigma(T)$ decreased linearly with $1/k_BT$.

The thermal activation energy (ΔE) was estimated from the temperature-dependence curve gradiant: $\ln\sigma(T) \sim 1/k_BT$. ΔE was found to be varied between 0.003 eV for the sample with highest T_S = 550 °C to 0.14 eV for the sample with lowest T_S = 200 °C. With such low activation energy, the hopping conductivity (σ_{hop}) through midgap defect states can be ruled out to be the reason for that high conductivity ($\sigma_D > 10^{-4}$ S/cm).

In SiC crystals, N acts as donor impurity [Götz1994; Choyke2004]; shallow O centers are donor-like defects in SiC, while deep O centers behaves as acceptor-like defects [Dalibor1998]. A shift of the Fermi level from midgap towards the conduction band tail can be concluded from the unintentional *n*-type doping, and it is presumed to be the dominant reason for such a high electrical conductivity ($\sigma_D > 10^{-4}$ S/cm) in nominally undoped μc-SiC:H material.

The effects of c_{MMS}, T_S, p and T_F on the spin density (N_S) and *g*-values estimated from ESR measurements at 40 K are summarized in Fig. 6.3.

In Fig. 6.3(a), an increase in N_S from 1.0×10^{18} to 5.4×10^{18} cm^{-3} and a slight increase in *g*-value from 2.0033 to 2.0035 is observed as c_{MMS} increases from 0.3 to 2%. In all the other series of T_S, p and T_F (Fig. 6.3(b), (c) and (d)), the spin density in μc-SiC:H remains at a very high level of 2×10^{18} – 2×10^{19} cm^{-3}, showing a slight decrease trend for increasing T_S, p and T_F. All the *g*-values in the series of T_S, p and T_F show a weak reduction between 2.0034 and 2.0030, however, a considerable scatter in the data points is observed.

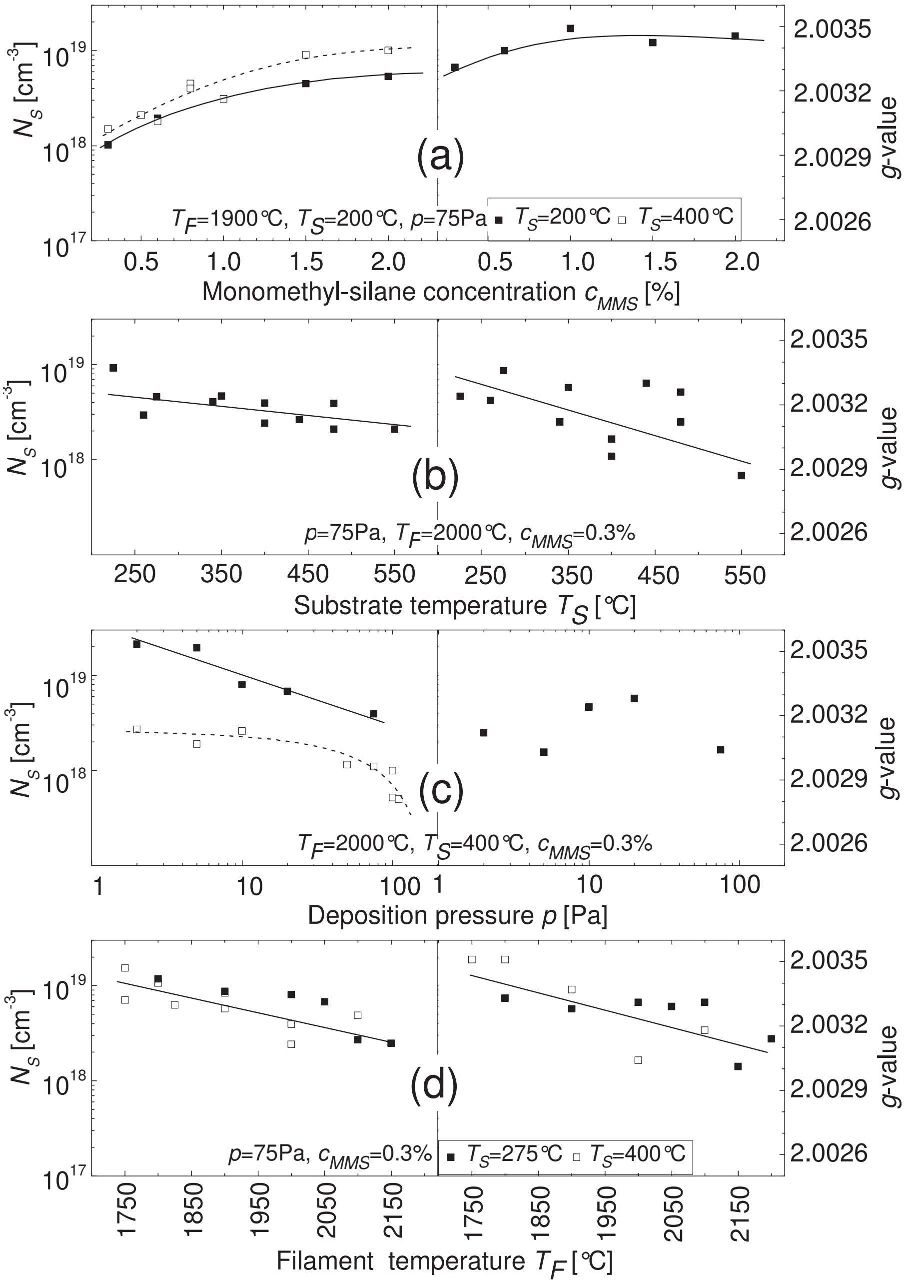

Figure 6.3 *Dependence of N_S and g-value on (a) c_{MMS}; (b) T_S; (c) p; (d) T_F for nominally undoped μc-SiC:H films. ESR spectra were measured at 40 K. Lines are guides to the eyes.*

Despite of a big data scattering, Fig. 6.4 shows a weak dependence of the spin density N_S on the crystallinity I_C^{IR} of nominally undoped μc-SiC:H films. All the samples have a high spin density $N_S = 2\times10^{18} - 2\times10^{19}$ cm^{-3}, and N_S shows a slight decrease with increasing crystallinity.

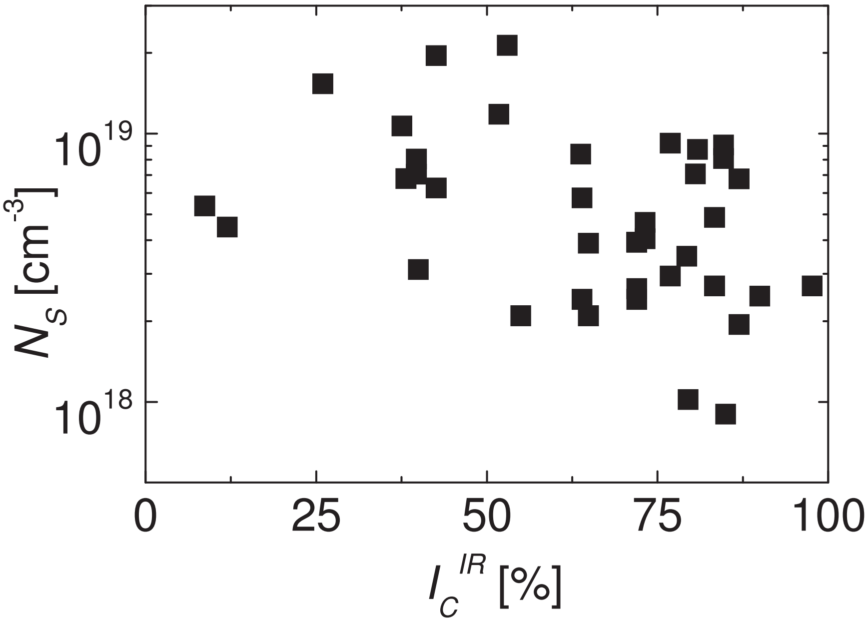

Figure 6.4 *Spin density (N_S) vs. thin film crystallinity (I_C^{IR}) for undoped μc-SiC:H samples by varying the deposition parameters c_{MMS}, T_S, p and T_F.*

Since only the paramagnetic defect states contribute to the ESR signal, the changes in the spin density could reflect the changes in the electronic occupation of the defect states. By analyzing the ESR spectral shape, more information about the paramagnetic defects can be derived. The evolution of room-temperature ESR spectra of nominally undoped μc-SiC:H samples with different crystallinity is given in Fig. 6.5.

All the samples demonstrate a slightly unsymmetrical single narrow central resonance with a peak-to-peak width (H_{PP}) of around 4 G and a g-value of 2.003 (±0.00005), which is assigned to neutral dangling bond defects [Janzén2003; Mizuochi2005] which are related to the Si- or C-vacancies. N_S of dangling bond states for low crystalline sample with $I_C^{IR} = 9\%$ was found to be around 10^{19} cm^{-3}. As the crystallinity increases, the central sharp resonance is resolved with a pair of hyperfine satellites with a splitting of 6 G. These hyperfine structures are supposed to be related to the nitrogen impurities [Wieringen1958] which may form a donor state, and therefore may be responsible for the high *n*-type conductivity in nominally undoped μc-SiC:H thin films. The film with the highest crystallinity ($I_C^{IR} \geq 90\%$) demonstrates ten times lower $N_S = 3\times10^{18}$ cm^{-3}.

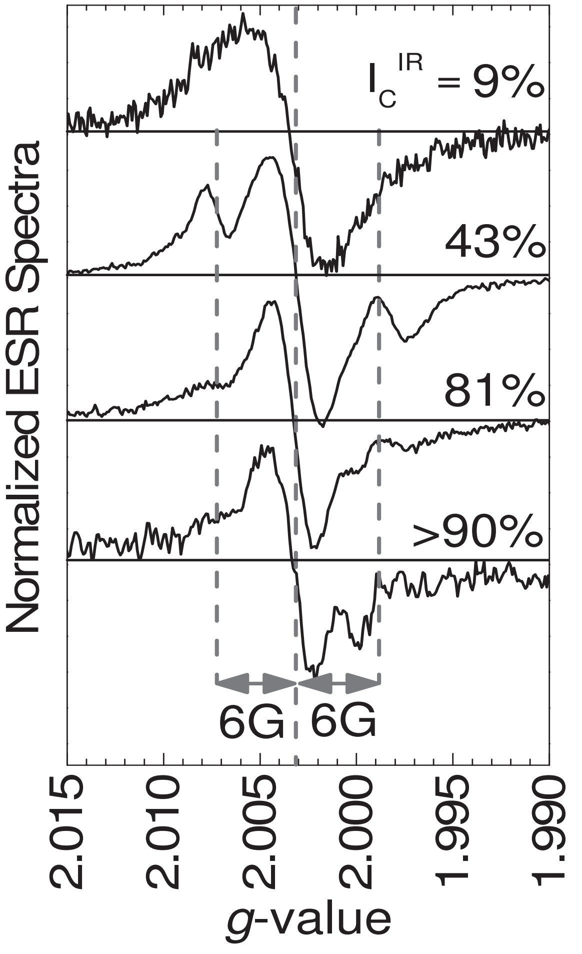

Figure 6.5 *ESR spectra of undoped μc-SiC:H films with different crystallinity (I_C^{IR}). The amplitude of the spectra is normalized to the same maximum for lineshape comparison.*

In summary, different deposition parameters (c_{MMS}, T_S, p and T_F) for nominally undoped μc-SiC:H films have a strong influence on the structural and electrical properties of the material, in agreement with earlier studies [Klein2006; Dasgupta2008; Klein2008]. The material was nominally undoped, but it exhibits pronounced *n*-type character as confirmed by thermal-power measurements, which is arguably attributed to the unintentionally doped oxygen ([O] = 10^{19} – 10^{20} cm^{-3}) and/or nitrogen ([N] = 10^{19} cm^{-3}) impurities.

The electrical dark conductivity (σ_D) covers a wide range of 10^{-12} – 10^{-1} S/cm and depends on the film crystallinity (I_C^{IR}). For most of the μc-SiC:H samples, they have high electrical conductivity ($\sigma_D \geq 10^{-5}$ S/cm) despite of high spin density ($N_S = 10^{18}$–10^{19} cm^{-3}), one possible reason is that E_F is moved towards the conduction band by unintentional *n*-type doping with nitrogen and/or oxygen. Increasing monomethyl-silane concentration (c_{MMS}) and substrate temperature have a negative influence on the film crystallinity, while higher pressure (p) and filament temperature (T_F) lead to higher film crystallinity.

6.3 Al-doping and post-deposition annealing of μc-SiC:H films

For optimal operation of a-Si:H single junction or a-Si:H/μc-Si:H tandem cells, the *p*-*i*-*n* configuration with *p*-side illumination is preferable [Hack1985], due to relatively low hole drift mobilities (μ_h = 3×10^{-3} cm^2/V·s, 300 K) compared to electrons (μ_e = 1 cm^2/V·s, 300 K). Therefore, a *p*-type window layer is required.

For *p*-type μc-SiC:H sample preparation, the same mixture of monomethyl-silane (5% Si_3HCH_3, diluted in H_2, MMS for short) was used as the source gases. Al is introduced in the form of $Al(CH_3)_3$ (Trimethyl-aluminum, TMAl for short). H_2 is used as carrier gas to dilute and transport TMAl to the gas mixture of MMS and H_2. The Al-doping ratio, which is defined as the ratio of the partial pressures of TMAl and MMS (p_{TMAl}/p_{MMS}), is varied from 0 to 0.1547. The effective amount of Al-doping, as well as the non-metallic species H, N and O, was measured with SIMS by Dr. Uwe Breuer from central division of analytical chemistry (ZCH) of Forschungszentrum Jülich. In order to calculate the accurate atom numbers in μc-SiC:H, c-, μc- and a-SiC were implanted with 0.1at.% Al and used as the standard references.

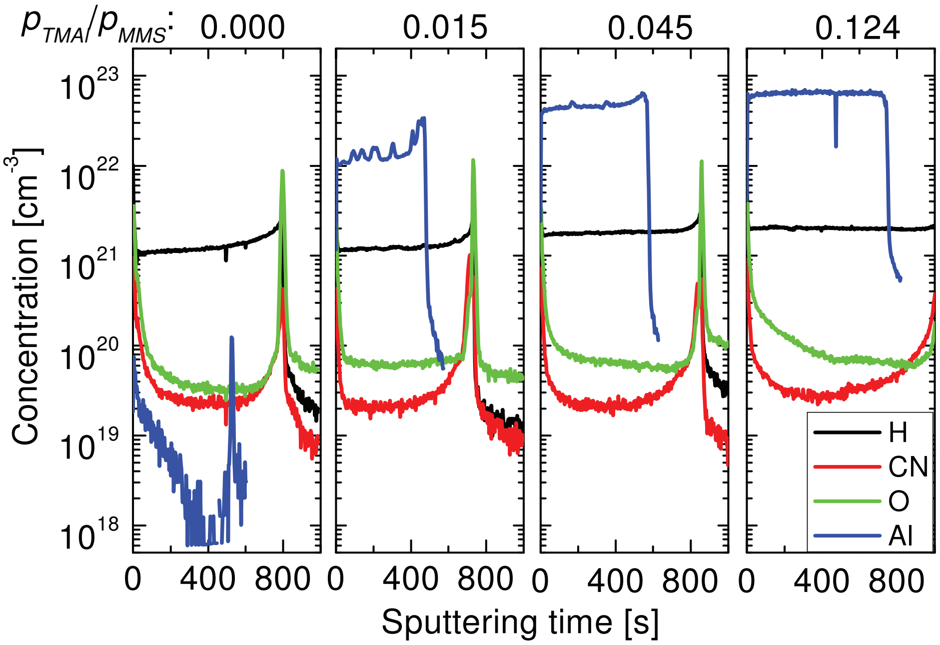

Figure 6.6 *Atomic concentrations of H, N, O and Al in μc-SiC:H films measured by SIMS. The corresponding doping ratio of* p_{TMA}/p_{MMS} *is noted above each spectrum.*

Fig. 6.6 shows that as p_{TMA}/p_{MMS} increases as 0.000, 0.015, 0.045 to 0.124, the amount of incorporated Al atoms increases from an undetectable level in undoped μc-SiC:H samples to a very high level of 6×10^{22} cm^{-3}, which implies alloying of Si-C with Al. It has proven the effective incorporation of Al with increase of p_{TMA}/p_{MMS}. At the same time, the concentration of incorporated H is 10^{21} cm^{-3} in undoped and lowly Al-doped (p_{TMA}/p_{MMS} = 0.015), while doubles in highly Al-doped (p_{TMA}/p_{MMS} = 0.045 and 0.124) μc-SiC:H samples. The O concentration in undoped μc-SiC:H is 3×10^{19} cm^{-3} and in Al-doped ones is 7×10^{19} cm^{-3}. But N has the same concentration of 3×10^{19} cm^{-3} in undoped and Al-doped samples. This finding indicates that the increase amount of O may come from the MMS source gas rather than from a leakage of the deposition chamber.

Al-doping leads to changes in the microstructure of the μc-SiC:H films. Fig. 6.7(a) shows the infrared spectra of μc-SiC:H thin films prepared at different p_{TMA}/p_{MMS}. The main peak centering at around 800 cm^{-1} corresponds to the Si-C stretching mode and is used as an indication of ordered SiC phase [Kerdiles2000; Rajagopalan2003]. As p_{TMA}/p_{MMS} increases, this peak changes from a narrow Lorentzian-like line to a broader Gaussian-like line, the peak position shifts towards lower wave numbers, and the integrated intensity decreases as well. The FWHM of the Si–C stretching vibration mode was observed to increase with decreasing grain size of SiC crystallites [Dkaki2001].

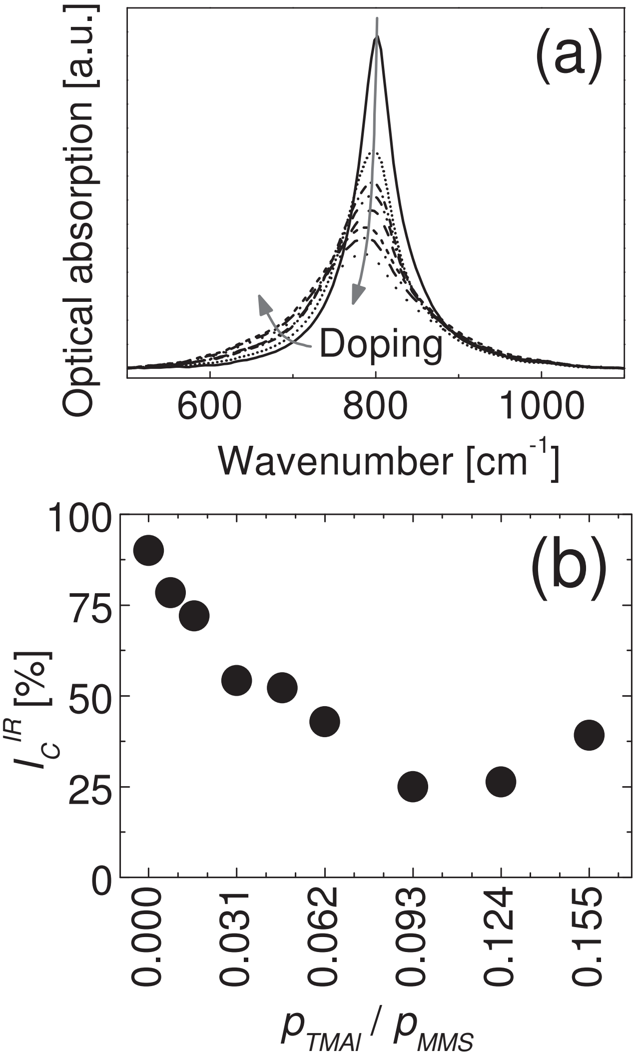

Figure 6.7 *(a) Infrared spectra of Al-doped μc-SiC:H thin films. Arrows indicated the increase of Al-doping ratio; (b) Thin film crystallinity (I_C^{IR}) v.s. Al-doping ratio p_{TMAl}/p_{MMS}.*

The film crystallinity (I_C^{IR}) was evaluated to be the ratio of integrated intensity of Lorentzian line to the total intensity. Fig. 6.7(b) presents the dependence of I_C^{IR} on the Al-doping ratio. A decrease of film crystallinity was observed with I_C^{IR} = 90% for undoped μc-SiC:H to 25% for the highly Al-doped μc-SiC:H films. That Al-doping hinders the crystalline growth of the SiC alloys was also confirmed by other techniques like Raman scattering, XRD and TEM [Miyajima2006; Chen2010(2); Köhler2011].

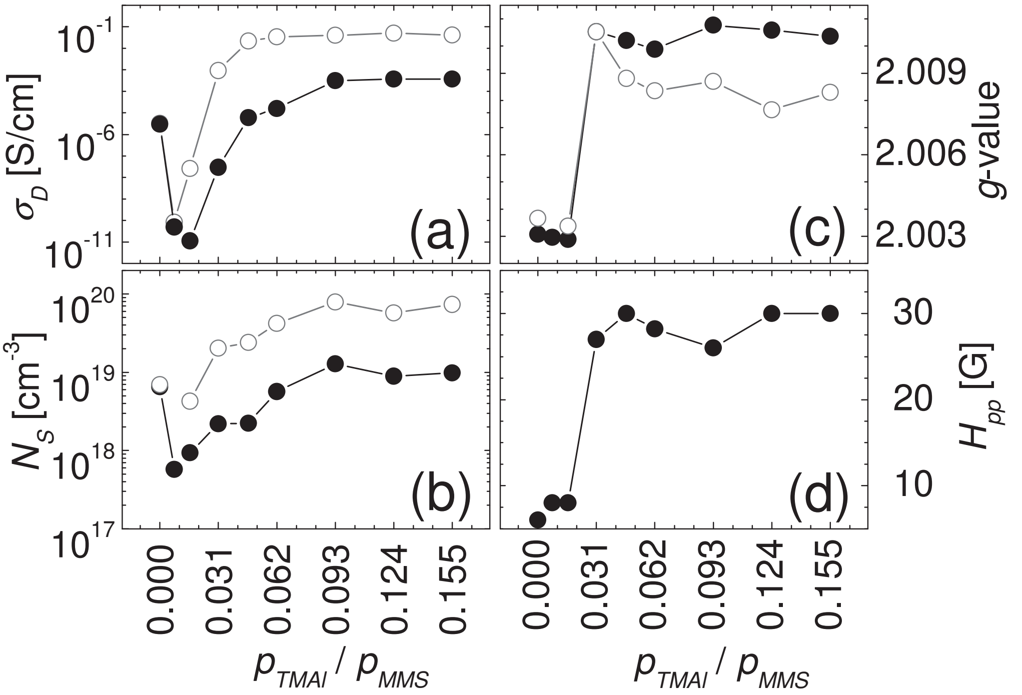

Figure 6.8 *Variation of (a) σ_D, (b) N_S, (c) g-value and (d) H_{PP} of ESR spectra with increasing Al-doping ratio (p_{TMAl}/p_{MMS}). Full symbols represent the as-prepared state; open circles represent the annealed state (450 °C for 30 min.). ESR measurements were performed at 40 K.*

The doping effect on σ_D, N_S, g-value, and peak-to-peak linewidth (H_{PP}) of the ESR spectra is presented by filled dots in Fig. 6.8 as a function of the Al-doping ratio (p_{TMAl}/p_{MMS}). Fig. 6.8(a) displays a typical compensation behavior from the initial n-type to the final p-type conductivity with Al-doping. The compensated material ($0 < p_{TMAl}/p_{MMS} < 0.031$) reaches a minimum conductivity value of $\sigma_D = 10^{-11}$ S/cm and N_S = 5×10^{17} cm^{-3} (Fig. 6.8(b)), and then increase to a saturated value of $\sigma_D = 4\times10^{-4}$ S/cm and N_S = 10^{19} cm^{-3} as p_{TMAl}/p_{MMS} increases from 0 to 0.1547. More Al-doping did not lead to further increase of σ_D or N_S.

Fig. 6.8(c) and (d) show that the *g*-value and H_{PP} remained unchanged at 2.003 and 6 G for undoped and compensated samples; but for $p_{TMAl}/p_{MMS} \geq 0.031$ all the samples have a *g*-value of $g \approx 2.01$ and $H_{PP} \approx 30$ G. The variation of the *g*-value suggests a change of paramagnetic defect from the Si- and/ or C-dangling bonds in highly crystalline nominally undoped μc-SiC:H to paramagnetic holes in the valence band tail in low crystalline *p*-type μc-SiC:H.

It is known that thermal annealing can activate Al acceptors in SiC. A series of μc-SiC:H films with increasing Al-doping ratio was annealed as follows: They were put in a quartz tube (diameter ≈ 25 mm) and pumped to a high vacuum with pressure below 2×10^{-3} Pa. Afterwards the tube was heated up to and kept at 450 °C for 30 min, and then cooled down before samples were taken out for investigation by ESR, electrical conductivity and optical absorption.

In Fig. 6.8, σ_D, N_S, *g*-value, and H_{PP} of the ESR spectra after annealing samples at 450 °C for 30 min are presented by empty circles. The variation of σ_D and N_S with Al-doping ratio was still observed. Annealing resulted in an overall increase of σ_D and N_S, the maximum value reached $\sigma_D^{\max} = 10^{-1}$ S/cm and $N_S^{\max} = 7\times10^{19}$ cm^{-3}, respectively.

An interesting finding is the annealing-induced variation of the *g*-values. For the samples with $g \approx 2.0031$, after annealing the *g*-values shifted to higher values; while for those highly Al-doped samples which had a $g \approx 2.0105$, after annealing the *g*-values shifted to lower values ($g \approx 2.0085$). This general shift of the resonance center could be resolved clearly in the ESR spectra displayed in Fig. 6.9. The evolution of ESR spectra of μc-SiC:H films before (black lines) and after annealing (red lines) are exhibited. One may notice that the ESR spectra suffered from the background signals from glass substrates, especially for samples with Al-doping ratio of $0.0309 < p_{TMAl}/p_{MMS} < 0.0619$.

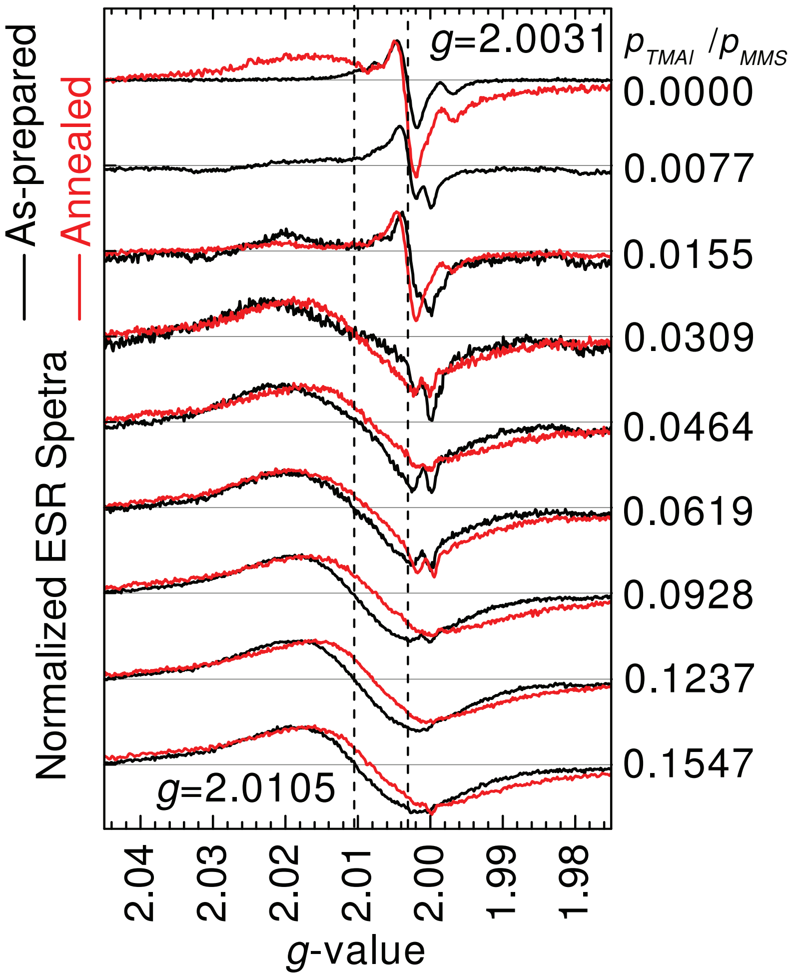

Figure 6.9 *ESR spectra measured at 40 K for μc-SiC:H thin films with increasing* p_{TMAl}/p_{MMS} *before (black) and after annealing (red). All the ESR spectra were normalized to the same maximum intensity for better comparison of ESR spectra.*

The influence of annealing of the optical absorption on nominally undoped and Al-doped (p_{TMAl}/p_{MMS} = 0.031) μc-SiC:H is shown in Fig. 6.10. One can see in Fig. 6.10 that for the undoped μc-SiC:H, annealing almost makes no difference in the optical bandgap (E_{04}), but a slightly higher absorption at low photon energies (E < 2 eV) is observed. As for the Al-doped μc-SiC:H, annealing led to an overall shift of the absorption spectrum towards lower photon energy. After annealing, E_{04} was reduced while a higher absorption in the low energy region was observed. Combined with the increase of ESR spin density and electrical conductivity, the absorption at $E < 2$ eV is attributed to the absorption of free carriers and/or defects.

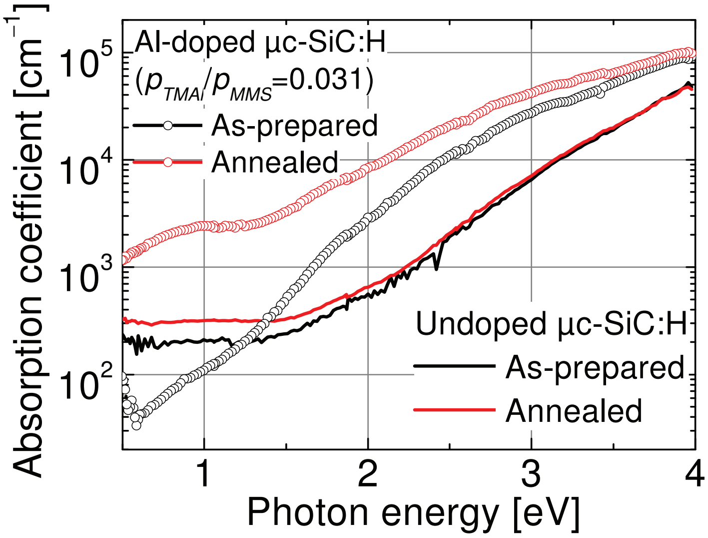

Figure 6.10 *Optical absorption of undoped and Al-doped (p_{TMAl}/p_{MMS} = 0.031) μc-SiC:H films before (black) and after annealing (red).*

6.4 Influences of pressure, substrate and filament temperature on *p*-type μc-SiC:H films

By Al-doping, *p*-type μc-SiC:H was successfully achieved. A high electrical conductivity has been obtained, but Al-doping also deteriorated the thin film crystallinity. But as a window layer, sufficient crystallinity is required for the nucleation of the consequent film if it is applied in μc-Si:H cells. Therefore, besides the Al-doping as discussed in Section 6.2, a broad range of deposition parameters was investigated to obtain *p*-type μc-SiC:H with high conductivity, high crystallinity and high transparency. They were varied as follows:

Substrate temperature: $T_S = 300 – 390$ °C
Deposition pressure: $p = 2 – 275$ Pa
Filament temperature: $T_F = 1900 – 2100$ °C.

In each series, p_{TMAl}/p_{MMS} and c_{MMS} were carefully selected to keep the μc-SiC:H material in the *p*-type doped region but still with high crystallinity.

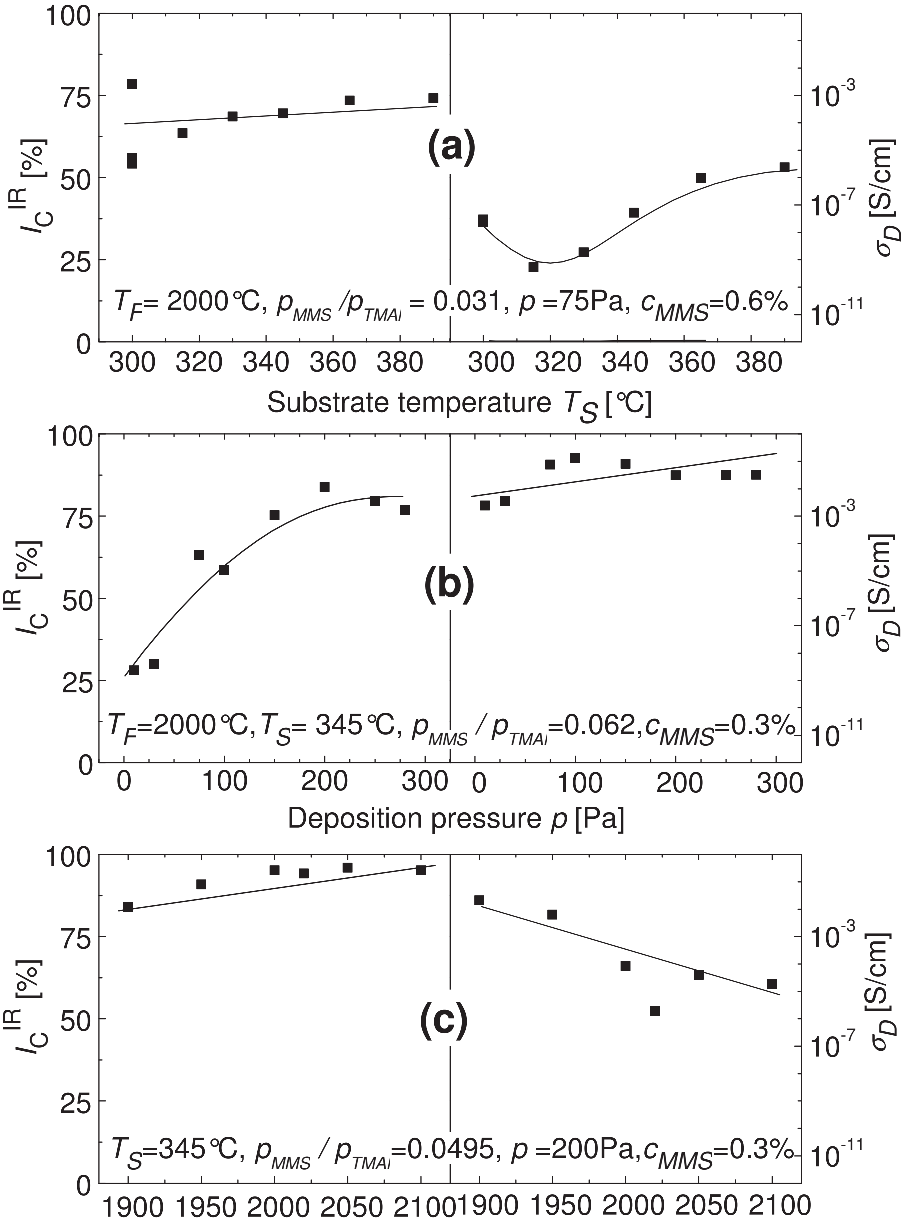

Figure 6.11 *Dependence of* I_C^{IR} *and* σ_D *on (a)* T_S*, (b)* p *and (c)* T_F *for Al-doped μc-SiC:H films. Other deposition conditions in each series are labeled. Lines are used to guide the eye.*

Fig. 6.11(a) shows the effect of the substrate temperature (T_S = 300 – 390 °C) on I_C^{IR} and σ_D. Other preparation conditions correspond to p_{TMAl}/p_{MMS} = 0.031 in Fig. 6.12. As T_S is varied from 300 °C to 390 °C, the crystallinity stays constant at 70%, and σ_D decreases from 10^{-8} S/cm to 10^{-10} S/cm then increases by four orders of magnitude up to 10^{-6} S/cm.

Fig. 6.11(b) shows the effect of the deposition pressure (p = 10–280 Pa) on I_C^{IR} and σ_D for p-type μc-SiC:H prepared at T_F = 2000 °C, T_S = 345 °C and p_{TMAl}/p_{MMS} = 0.062. The increase in pressure leads to an increase of the crystalline volume fraction from 30% up to 80% and a small gradual increase in conductivity at a high level around 10^{-1} S/cm.

Fig. 6.11(c) shows that, as T_F increases from 1900 to 2100 °C, the crystallinity maintains at a very high level of 85–95%. The dark conductivity σ_D surprisingly decreases from 10^{-2} to 10^{-5} S/cm at the highest T_F which yields the highest crystallinity.

Thus, with optimization of the deposition parameters, highly conductive as well as highly crystalline p-type μc-SiC:H can be obtained. In all the T_S, p and T_F series, the Al-doping ratio was selected high enough to provide sufficient p-type doping of μc-SiC:H films but sufficiently low to avoid alloying of SiC with Al. As sample preparation developed, p_{TMAl}/p_{MMS} was slightly varied to make a compromise of high conductivity and high optical transparency.

N_S and g-values are summarized in Fig. 6.12, depending on T_S, p and T_F, respectively.

Fig. 6.12(a) shows that as T_S increases from 300 to 390 °C, N_S first decreases from an average level of 1–5×10^{18} cm^{-3} to the minimum value of 5×10^{17} cm^{-3} at T_S = 315 °C, and then increases to 2×10^{18} cm^{-3} at T_S = 390 °C, while the g-values stay nearly constant at 2.003.

Fig. 6.12(b) shows that as the deposition pressure increases from 10 to 280 Pa, N_S firstly decreases from 10^{19} to 2×10^{18} cm^{-3} at p = 75 Pa, then increases slightly as p is further increased. The g-value decreases from 2.009 to 2.003.

Fig. 6.12(c) shows the influence of the filament temperature T_F on N_S and g-values. As T_F increases from 1900 °C to 2100 °C, the spin density remains constant at a low level around 1–2×10^{18} cm^{-3} and the g-value remains constant at 2.003.

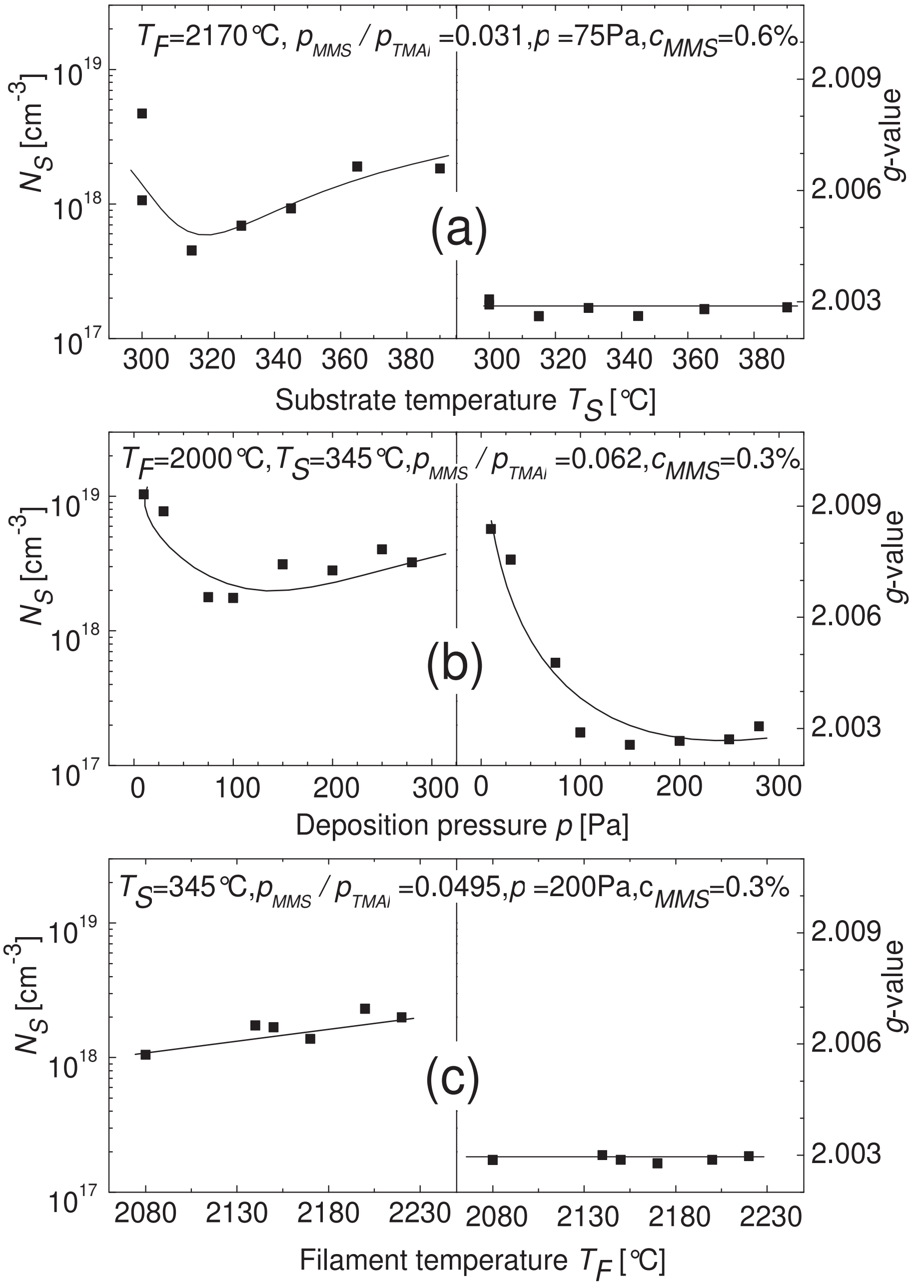

Figure 6.12 *Dependence of N_S and g-values for Al-doped μc-SiC:H films on (a) T_S, (b) p and (c) T_F. All the ESR spectra were measured at 40 K. Lines are guides for the eye.*

Briefly, all the Al-doped μc-SiC:H samples show a high level of spin density varying between 10^{18} – 10^{19} cm^{-3}, with a minimum value of 5×10^{17} cm^{-3} in the sample which is doped to be nearly intrinsic (shown in Fig. 6.12(b)).

One has to be aware that any variation of the preparation parameters will affect both the structural and chemical composition of the material. Moreover, even at the same chemical composition and crystallinity, the crystalline phase may vary due to different polytypes of crystalline silicon carbide (c-SiC). Nevertheless, the crystallinity is a relevant integral measure of structural order in the material which has been used above for the comparison of the samples from the undoped set prepared under different conditions.The strong effects of Al-doping are also clearly observed in ESR measurements. The variation of the spin density as a function of Al-doping is consistent with a shift of the Fermi level from the conduction band down into the gap and then further into the valence band tail.

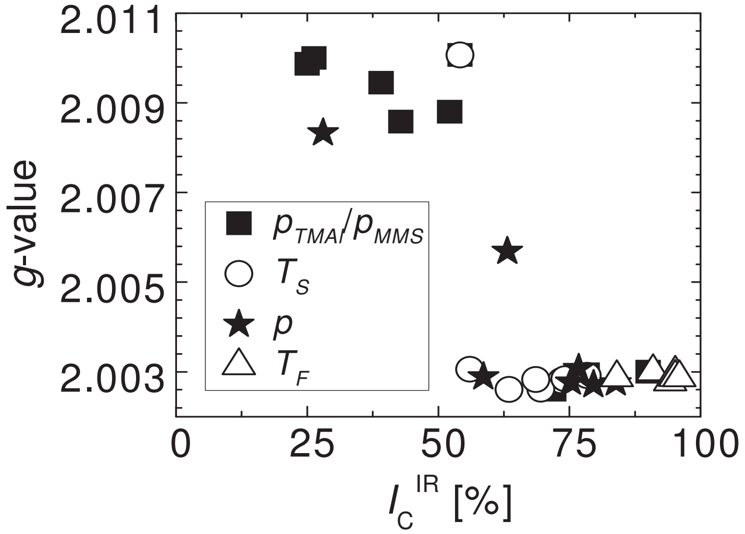

Figure 6.13 *g-values estimated from the ESR measurements at 40 K for Al-doped μc-SiC:H films prepared at different preparation conditions vs. thin film crystallinity* I_C^{IR}.

In the ESR spectrum of the compensated μc-SiC:H sample (p_{TMAl}/p_{MMS} = 0.0077), in addition to the narrow line at g = 2.003, a broad ($H_{PP} \approx 30$ G) resonance at $g \approx 2.01$ appears and dominates the spectrum for higher Al doping levels. This broad ESR spectrum of the *p*-type μc-SiC:H is qualitatively similar to ESR observations in *p*-type a-Si:H [Dersch1981]. By analogy is associated with holes trapped in the valence band tail. This broad resonance at $g \approx 2.01$ has only been observed in *p*-type μc-SiC:H of low crystallinity. When plotting the *g*-values as a function of the thin film crystallinity (Fig. 6.13), one can find that in contrast to the low crystalline *p*-type μc-SiC:H samples, the highly crystalline *p*-type μc-SiC:H shows the narrow resonance at $g = 2.003$ similar to the *n*-type μc-SiC:H, and the explanation still remains puzzling.

In summary, all the μc-SiC:H samples have relatively high $N_S = 5\times10^{17} - 2\times10^{19}$ cm^{-3}, with the minimum occurring in the compensated sample. For *p*-type μc-SiC:H one can roughly distinguish between amorphous material where the highest N_S has been observed and highly crystalline μc-SiC:H which has lower N_S in the range of 1–5×10^{18} cm^{-3}. Note that the calculated ESR N_S is the integration of all paramagnetic states (e.g. the Si- and C-dbs) observed in ESR experiment where possible contributions from Si-db from C-db in μc-SiC:H can not be resolved.

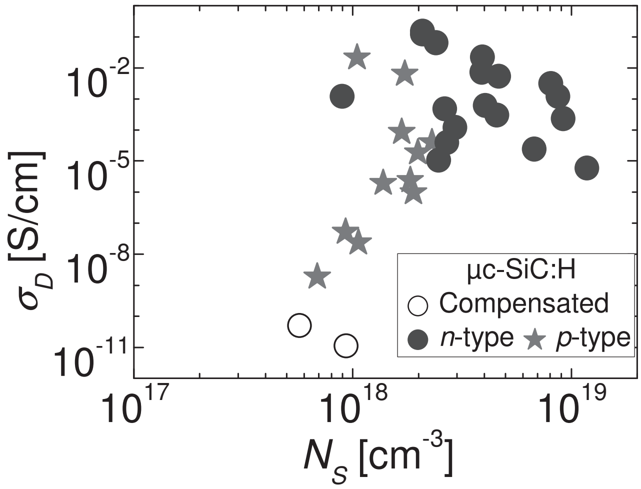

Figure 6.14 *σ_D vs. N_S for highly crystalline (I_C^{IR} ≥ 50%) n-type, compensated and p-type μc-SiC:H films. All the samples show a g-value of 2.003.*

In order to compare the dependence of conductivity on the ESR spin density, in Fig. 6.14, σ_D is plotted as a function of N_S for all the *n*-type, compensated and *p*-type μc-SiC:H samples with high crystallinity (I_C^{IR} ≥ 50%). It is interesting to find that the compensated samples show the lowest σ_D and N_S; all *n*-type μc-SiC:H, which are nominally undoped but unintentionally doped by nitrogen and oxygen impurities, show a high electrical conductivity ($\sigma_D > 10^{-5}$ S/cm) independent on the spin density (N_S); while for *p*-type μc-SiC:H, σ_D increased from 10^{-7} S/cm to a high level of 10^{-1} S/cm. ESR lines with very similar *g*-values have been observed in highly crystalline μc-SiC:H (in both *p*- and *n*-type materials) with different conductivity and Fermi level position. This finding makes the identification of defects in μc-SiC:H difficult. At present the observed picture is speculatively explained by the inhomogeneities in μc-SiC:H tissues.

6.5 Summary and conclusions

The relationships between the structure, electrical conductivity and paramagnetic states have been investigated for μc-SiC:H thin films prepared over a broad range of HWCVD process parameters, such as T_S, p, T_F, c_{MMS}. Nominally undoped μc-SiC:H films are *n*-type doped, which is presumed to be related with N impurities considering the electrical conductivity and the similarity of ESR spectra with N-doped SiC crystals [Wieringen1958]. Al-doping leads to compensation of the unintentional *n*-type doping and provides effective *p*-type doping at higher Al concentrations. A high conductivity of 0.1 S/cm has been achieved. The reduction of crystallinity induced by Al-doping can be minimized by adjusting other process parameters, and has resulted in highly doped μc-SiC:H with a material crystallinity $I_C^{IR} = 60 - 90\%$ and electrical conductivity $\sigma_D = 10^{-6} - 10^{-2}$ S/cm.

ESR spectra of Al-doped μc-SiC:H are strongly affected by the material structure and are not in direct relation with Al-doping. A broad resonance with $H_{PP} \approx 30$ G at $g \approx 2.01$ is observed in Al-doped μc-SiC:H of low crystallinity. By analogy with ESR spectra of *p*-type a-Si:H, this ESR line is suggested to originate from paramagnetic holes in the valence band tail. In contrast, highly crystalline Al-doped μc-SiC:H shows the resonance at $g = 2.003$ similar to the undoped μc-SiC:H material.

In Al-doped *p*-type μc-SiC:H films, no direct correlation of *g*-value or N_S with σ_D has been found, whereas crystallinity and Al concentration play critical roles in the electrical and paramagnetic properties. All the Al-doped μc-SiC:H samples still have a high N_S varying from 10^{18} to 10^{19} cm^{-3}. Sufficient electrical conductivity that is applicable for Si-based thin-film solar cells can be achieved with increasing the Al-doping ratio (e.g. $p_{TMAl}/p_{MMS} > 0.0464$ in Fig. 6.8(a)), increasing the substrate temperature (e.g. $T_S > 360$ °C in Fig. 6.11(a)) and optimized deposition pressure and filament temperature.

Chapter 7: ESR investigation of µc-SiO$_x$:H

Silicon oxide in various forms of structure or composition has been providing a countless number of optoelectronic applications over history. In the field of Si-based thin-film solar cells, hydrogenated microcrystalline silicon oxide (µc-SiO$_x$:H) has been used as the *window layer* of both *n*-type µc-SiO$_x$:H for µc-Si:H or *p*-type µc-SiO$_x$:H for a-Si:H single junction cells [Ichikawa1996; Jana2000; Matsumoto2008; Sritharathikhun2009; Smirnov2010; Lambertz2012] and also the *intermediate reflector layer* (IRL) in a-Si:H/µc-Si:H tandem cells [Sichanugrist1993; Sarker2002; Bühlmann2007; Lambertz2007; Schropp2008; Grundler2010; Cuony2010; Lambertz2011]. For both applications, a well – adjusted compromise between the electrical, optical and structural properties is required, e.g. sufficient electrical conductivity (σ) for a low series resistance of the tandem cells; high optical transparency, which means a wide optical bandgap (E_{04}), to minimize light absorption losses; appropriate material crystallinity for the subsequent film growth, *etc*.

µc-SiO$_x$:H has been proven to be a phase – mixture of µc-Si:H and a-SiO$_x$:H [Lambertz2007], in which the microcrystalline component can offer sufficient conductivity and sensitivity for doping. The a-SiO$_x$:H component can supply a large refractive index difference between the IRL and the cell material ($n_{\mathrm{SiO2}} = 1.5$, $n_{\mathrm{Si}} = 3.8$) to reflect more light back to the top cell when being used as an IRL, and wider optical bandgap ($E_{04(\mathrm{SiO2})} = 8.9$ eV, $E_{04(\mathrm{Si})} = 1.8$ eV) to remain transparent for long wavelength light to reach the bottom cell.

This chapter starts with the sample (film, powder) preparation. ESR features of the µc-SiO$_x$:H material are elaborated for PH$_3$-doped powder samples. A wide range of deposition parameters (e.g. oxygen content, PH$_3$-doping, seed layer and [SiH$_4$]:[H$_2$] gas ratio) is investigated with regard to the material crystallinity, electrical conductivity, ESR spin density and *g*-values. At the end of the chapter, a short summary will be given.

7.1 µc-SiO$_x$:H sample preparation by PECVD

µc-SiO$_x$:H thin films were deposited by Radio Frequency Plasma-Enhanced Chemical Vapor Deposition (RF-PECVD, 13.56 MHz) with a plasma power density of 0.33 W/cm^2 at a substrate temperature of T_S = 185 °C. Silane (SiH_4), hydrogen (H_2) and carbon dioxide (CO_2) are used as source gases, and a gas mixture of 2% phosphine (PH_3) in SiH_4 has been used for *n*-type doping. The electrode geometry and typical deposition parameters are listed in Table 7.1:

Table 7.1 *Electrode geometry and deposition parameters for µc-SiO$_x$:H films*

Electrode geometry	
Diameter	135 mm
Anode (A) – Cathode (C) distance	20 mm
Deposition parameters	
Substrate temperature	185 °C
Pressure	4.0 mbar
Radio frequency	13.56 MHz
Power density	0.33 W/cm^2
Gas flow	
SiH_4	0 – 2.0 sccm
H_2	100 – 1000 sccm
CO_2	1 – 7.0 sccm
2% PH_3 in SiH_4	0 – 1 sccm
Seed layer (~ 30 nm)	No seed, VHF *i*- or *n*-type µc-Si:H seed

Note: A '*seed layer*' is a very thin (thickness ≤ 30 nm) predeposited intrinsic µc-Si:H layer on glass substrate before µc-SiO$_x$:H film deposition. It is designed to benefit the nucleation of the subsequent µc-SiO$_x$:H layer and also its adhesion to the substrate.

In the following context, for simplification of sample denotation, abbreviations will be used to represent the deposition parameters for a given sample. The abbreviation is presented in the same order as in table 7.1, e.g. '1/ 500/ 1.5/ 2%/ *i*-seed' means gas flows for SiH_4, H_2 and CO_2 are 1, 500, 1.5 sccm, respectively, 2% PH_3 in SiH_4 is used for doping and an *i*-type µc-Si:H seed layer is deposited prior to the µc-SiO$_x$:H film deposition.

Films with a thickness of 270 – 1600 nm were deposited on glass substrates. RBS measurements were performed on films deposited on glass substrates for estimation of the oxygen content, and PDS measurements for optical absorption.

For electrical conductivity measurements, Ag contacts (thickness = 700 nm, length = 5 mm, width = 5 mm, distance = 0.5 mm) were evaporated onto the film. In order to avoid a possible influences of atmospheric gases (e.g. O_2, N_2, H_2O, CO_2, *etc*.), which may be adsorbed on the film surface, films were annealed at 440 K for 30 min in vacuum. Conductivity is measured at room temperature in high vacuum (pressure $\leq 10^{-3}$ pa).

For crystallinity evaluation (I_C^{RS}), Raman scattering measurements were performed on thin films deposited on glass substrates. Zero crystallinity means that no µc-Si:H signal is found in the Raman spectra, the material is basically a-SiO$_x$:H of, high oxygen content (e.g. $SiO_{1.5}$) and wide band gap ($E_{04} \approx 2.8$ eV). The most crystalline material is the pure µc-Si:H without oxygen incorporation. Normally, highly crystalline µc-Si:H has a paramagnetic defect density of a few times 10^{15}–10^{16} cm^{-3}, which is 3 orders of magnitude lower than that of a-SiO$_x$:H (a few times 10^{18} – 10^{19} cm^{-3}) [Janotta2004].

For ESR measurements below room temperature (e.g. 40 K), samples are placed in a quartz tube which has an inner diameter of 4 mm. Therefore, glasses substrates with films were cut into small slides with a size of 0.3×2 cm^2. Each ESR measurement has been averaged over a large number of scans with the modulation field kept at approximately half of the peak-to-peak linewidth of the narrowest feature in each spectrum.

µc-SiO$_x$:H powder samples were prepared in the similar way as Si powders (described in Section 5.1) with the deposition parameters of 1/ 500/ CO_2 = 0.5 and 1.5 sccm/ 2%/ no-seed. The electrical dark conductivity (σ_D) and Raman crystallinity (I_C^{RS}) were both measured on co-deposited thin film samples on glass substrates. For samples with CO_2 = 0.5 and 1.5 sccm, they have σ_D = 0.28 and 0.02 S/cm and $I_C^{RS} \approx 60\%$ and 40%, respectively.

7.2 ESR investigation of *n*–type µc-SiO$_x$:H powder

7.2.1 Paramagnetic defects in Si/SiO$_x$ system

Spectroscopic signatures of the paramagnetic defects in the silicon – silicon oxide systems have been reported in a number of ESR studies, most of these primarily dealt with two most important families of paramagnetic centers: E' centers and P_b centers. Here, some paramagnetic defects which are related to the μc-SiO$_x$:H material are listed:

- Si dangling bonds in a-Si:H and μc-Si:H: ($Si_3 \equiv Si\bullet$, here the short lines represent chemical bonds, and the dot represents an unpaired electron in a dangling Si sp^3 hybrid). A Si dangling bond (Si-db) defect is an unpaired electron localized on a silicon backbonded to three atoms of silicon or hydrogen. The dominating paramagnetic defect in hydrogenated Si is believed to be the neutral Si-db. It has been widely discussed in both a-Si:H [Brodsky1969; Street1980; Dersch1981; Stutzmann1985; Yam1986] and μc-Si:H [Finger1998; Müller1999; Lips2003], in which it shows a g-value of $g = 2.0050 \sim 2.0055$ and $g = 2.0043 \sim 2.0052$, respectively.
- $E^{'}$ centers ($O_3 \equiv Si\bullet$): They are actually Si-db-like defects, in which an unpaired electron localized on a single or multiple Si backbonded to oxygen atoms, essentially pictured as an oxygen vacancy center. The $E^{'}$ centers are the most prominent paramagnetic defects in amorphous silicon oxide, there are different variants, such as $E_{\alpha}^{'}, E_{\beta}^{'}, E_{\gamma}^{'}, E_{\delta}^{'}, E_{S}^{'}$ or EX centers [Weeks1956; Carlos1984; Takahashi1987; Awazu1993; Lenahan1998; Buscarino2007; Jivănescu2010]. In PECVD – deposited SiO$_x$, $E^{'}$ centers are mainly found near the oxide/air interface [Barklie2001, and references therein]. In a-SiO$_2$, $E^{'}$ centers have an average g-value of $g = 1.9998 \sim 2.0021$ [Jivănescu2010], depending on the microstructural environment surrounding the paramagnetic defects.
- P_b centers ($Si_3 \equiv Si\bullet$) at or near the Si/SiO$_2$ interface: They are ascribed as trivalent silicon, which has an unpaired electron localized on a Si backbonded to three Si atoms in the Si-O network. P_b -type centers have been widely reported in a-SiO$_2$ grown on crystalline Si substrates [Nishi1971; Caplan1979; Lenahan1982; Stathis1991; Cartier1995; Stesmans2008], e.g. at the (111) Si/a-SiO$_2$ interface, P_b point defects have been identified with ESR technique, they exhibit a g-value of $g_1 = g_2 = 2.0086$ and $g_3 = 2.0013$ and a hyperfine doublet with $a_{\mathrm{iso}} \approx 112$ G [Brower1983]; at the (100) Si/a-SiO$_2$ interface, two types of P_b -type point defects – P_{b0} [Stesmans1990; Keunen2011] and P_{b1} [Stesmans1998] variants, have been observed with ESR, P_{b0} exhibits a g-value of $g_1 = g_2 = 2.0081$ and $g_3 = 2.00185$, P_{b1} exhibits a g-value of $g_1 = 2.00735$, $g_2 = 2.00577$, $g_3 = 2.0022$.

- S center ($SiO_2 \equiv Si\bullet$, or a combination with $Si_2O \equiv Si\bullet$): It is attributed to an intermediate variant state between E'_γ and P_b centers [Holzenkampfer1979; Hosono1994; Stirling2002]. In SiO$_x$,(0< x < 2) it was reported to have a *g*-value of g = 2.0027.
- P-related defects: P$_1$ (Hole trap, $O_3 \equiv P\bullet$), P$_2$ (Hole trap, $O_4 \equiv P\bullet$), P$_4$ (Electron trap, $O_2 = P\bullet$) and POHC (Phosphorous oxygen hole trapping center) [Griscom1976; Griscom1983]. Additionally, in μc-Si:H, by efficient phosphorous doping, the Fermi-level shifts towards the bottom of the conduction band, so that the CE-resonance has also been reported [Finger1994; Finger1998; Müller1999; Fuhs2000; Lips2002; Lips2003].
- C – and N – related defects: The reaction of C and N competing with O for Si atoms only takes place at a temperature ≥ 750 °C, which is much higher than the deposition temperature for μc-SiO$_x$:H ($T_S \approx$ 185 °C). Therefore these two kinds of defects could be ignored.

7.2.2 ESR investigation of PH$_3$-doped μc-SiOx:H powder

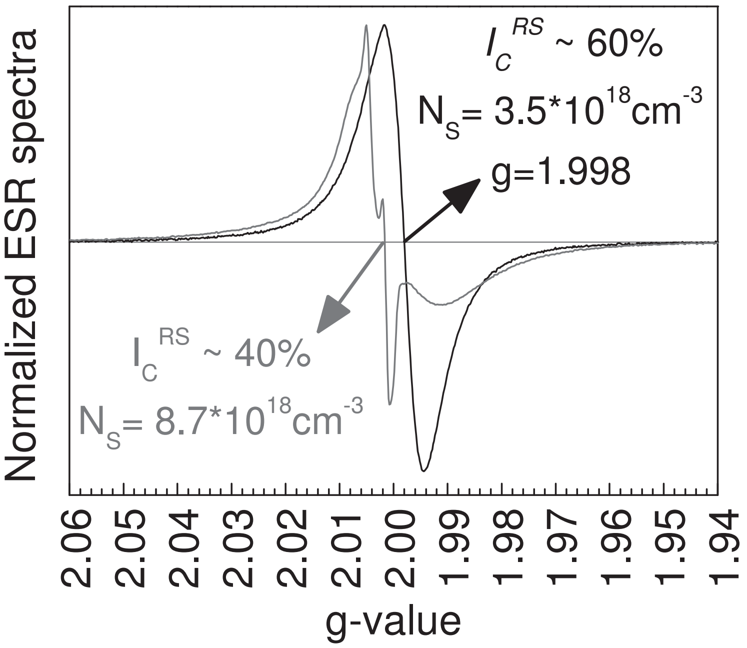

Figure 7.1 *Normalized ESR spectra measured for μc-SiO$_x$:H powders* (1/ 500/ CO$_2$ = 0.5 and 1.5 sccm/ 2%/ no seed). *Corresponding Raman crystallinity and spin density are noted.*

Fig 7.1 shows the ESR spectra for the two µc-SiO$_x$:H powder samples. The spectra were normalized to the same maximum intensity for comparison of the ESR line shape. The µc-SiO$_x$:H powder sample with CO$_2$ = 0.5 sccm ($I_C^{RS} \approx 60\%$) has a high spin density of $N_S = 3.5\times10^{18}$ cm^{-3}. Its ESR spectrum centered at g = 1.998 and turned out to be a single broad line which has a peak-to-peak width of H_{PP} = 12 G. This resonance is similar to CE-resonance in *n*-type Si, which is also known in µc-Si:H [Finger1994; Malten1999; Lips2003]. The sample with CO$_2$ = 1.5 sccm ($I_C^{RS} \approx 40\%$) has a higher spin density of $N_S = 8.7\times10^{18}$ cm^{-3}.

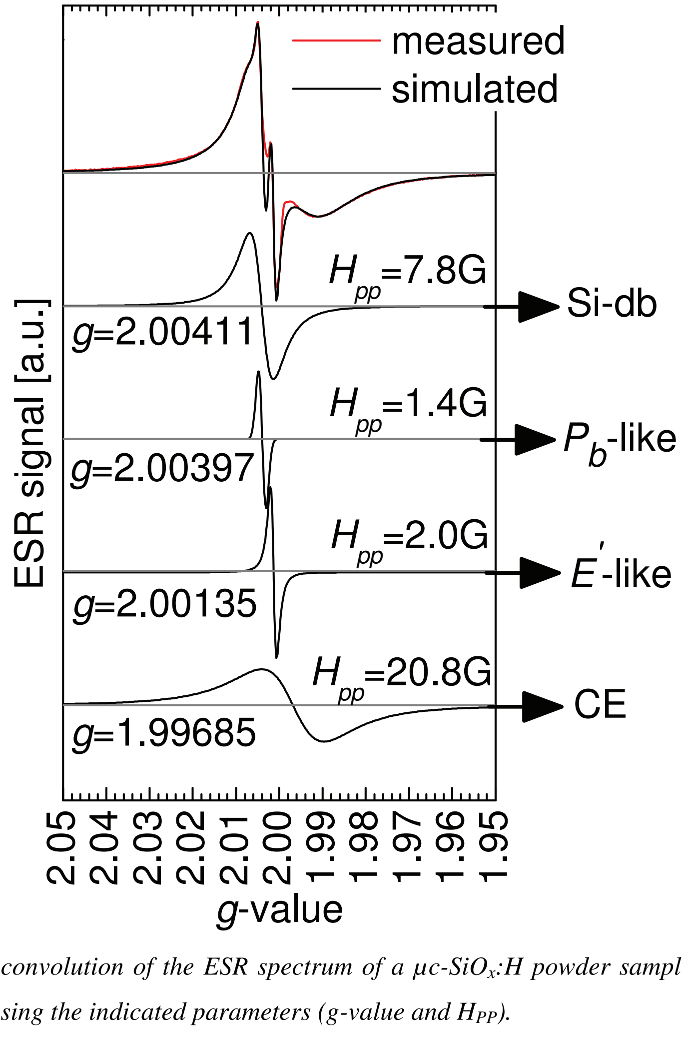

Figure 7.2 *Deconvolution of the ESR spectrum of a µc-SiO$_x$:H powder sample (1/ 500/ 1.5/ 2%/ no seed) using the indicated parameters (g-value and H_{PP}).*

The ESR spectrum is more complex and can be decomposed into different components. Fig. 7.2 shows a comparison of the as – measured ESR spectrum (red line) of powder sample 1/ 500/ 1.5/ 2%/ no seed with the simulation spectra (dark lines). The simulation line is a composition of four components with the following parameters (g-value, peak-to-peak linewidth): (2.00411, 7.8 G), (2.00397, 1.4 G), (2.00135, 2.0 G), and (1.99685, 20.8 G).

The component with $g = 2.00411$ and $H_{PP} = 7.8$ G is similar to the line observed in µc-Si:H, where it is attributed to Si dangling bonds. The second and third components are suggested to be from P_b – like and/ or E' – like centers. The fourth component is attributed to the CE – resonance (as described in Section 5.3).

7.3 ESR investigation of µc-SiO$_x$:H thin films

µc-SiO$_x$:H alloy thin films were deposited on Corning glasses by PECVD. Deposition parameters like the oxygen incorporation (CO_2), phosphorus doping (PH_3), the hydrogen dilution (ratio of the gas flow: [SiH_4]:[H_2]) and the seed layer were investigated. The correlation between structural, optical, electrical, and ESR properties will be discussed next.

7.3.1 Effect of oxygen incorporation

The amount of oxygen incorporated into the µc-SiO$_x$:H films is a key parameter that determines the material's optical and electronic properties. A series of µc-SiO$_x$:H films (1/ 500/ CO_2 = 0…7.0 sccm/ 2%/ no seed) were prepared with only varying the CO_2 flow.

Raman spectra of µc-SiO$_x$:H are shown in Fig. 7.3. The peak at 520 cm^{-1} is attributed to silicon crystallites, and the peak at 480 cm^{-1} to the amorphous phase (a-SiO$_x$:H, $x = 0 – 1.5$). All the spectra were normalized by the same maximum intensity for comparison of lineshape. As the CO_2 flow increases from 0 to 1.5 sccm, the intensity of peak at 480 cm^{-1} increases. When CO_2 flow ≥ 2.0 sccm, only a single broad line at 480 cm^{-1} was observed, no peak corresponding to µc-Si:H phase can be found, the material is a-SiO$_x$:H. I_C^{RS} is plotted as a function of the CO_2 gas flow in the inset of Fig. 7.3. The material covers a microstructure range from highly crystalline µc-Si:H (I_C^{RS} = 75%) to a-SiO$_x$:H (I_C^{RS} = 0%)

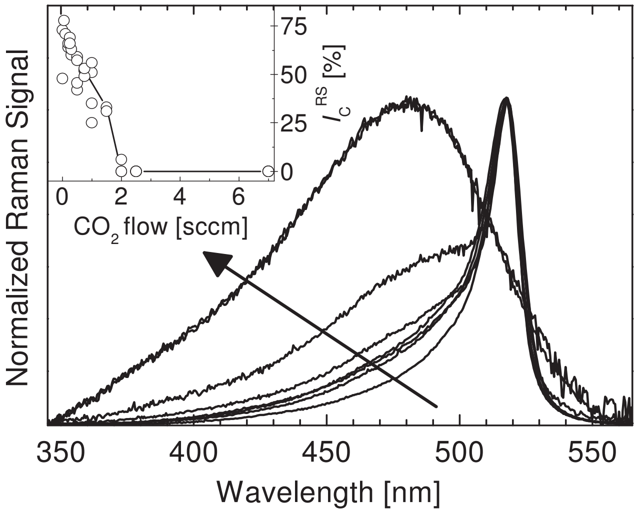

Figure 7.3 *Normalized Raman scattering spectra of μc-SiO$_x$:H films (*1/ 500/ CO$_2$ = 0…7.0 sccm/ 2%/ no seed*) on glass substrate. The arrow indicates the increase of CO$_2$ gas flow. I_C^{RS} is plotted as a function of CO$_2$ gas flow in the inset.*

The amount x of incorporated oxygen is shown in Fig. 7.4 as a function of CO$_2$ flow. It demonstrates an increase of the oxygen content from microcrystalline Si (x = 0) to amorphous silicon oxide (a-SiO$_{1.5}$:H). Obviously, x increases with CO$_2$ flow and nearly saturates at relatively high CO$_2$ flow ≥ 3 sccm.

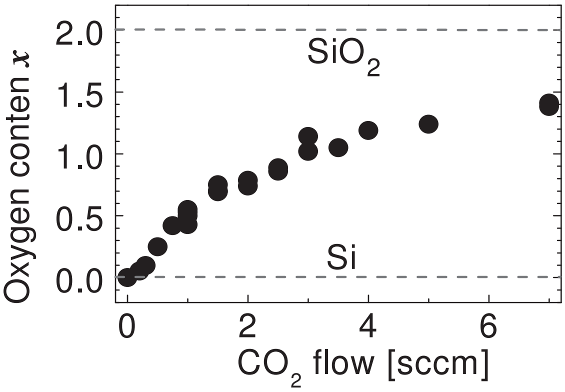

Figure 7.4 *Oxygen content in μc-SiO$_x$:H samples vs. CO$_2$ gas flow. Dashed lines indicate the limits of pure Si (x = 0) and bulk SiO$_2$ (x = 2).*

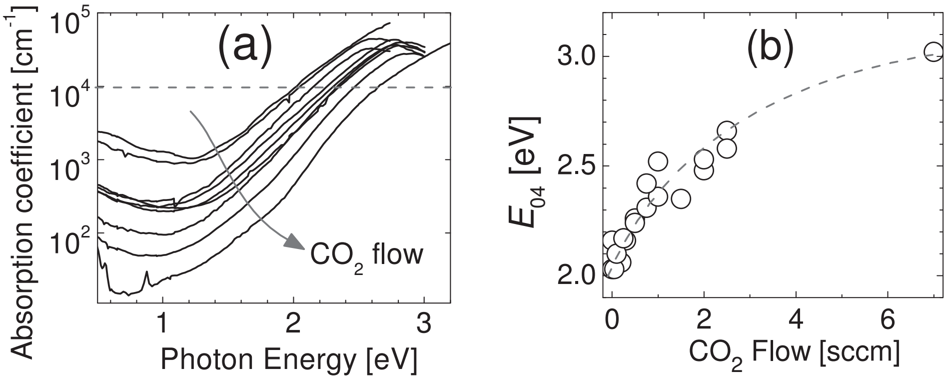

Figure 7.5 *(a) Optical absorption for μc-SiO$_x$:H layers (1/ 500/ CO$_2$= 0.0…7.0 sccm/ 2%/ no seed). The arrow indicates the increase of CO$_2$ flow. (b) E_{04} vs. CO$_2$ flow.*

As the oxygen content increases, the optical absorption also changes. From Fig. 7.5(a) one can see that the photon energy at an absorption coefficient α = 10^4 cm^{-1} (E_{04}) increases from 2.0 to about 3.0 eV as CO$_2$ flow increases from 0.0 to 7.0 sccm (Fig. 7.5(b)), and the optical absorption in the lower photon energy region decreases. The absorption at lower photon energy is believed to be related to the free carriers and defects located in the band gap.

Fig. 7.6 presents the ESR spectra (a), spin density (b) and *g*-values (c) from this series of μc-SiO$_x$:H samples. ESR measurements were performed at 40 K. From the ESR spectra in Fig. 7.6(a) one can see that the peak-to-peak width (H_{PP}) of the ESR spectra increases as the CO$_2$ flow increases from 0 to 1.0 sccm and then decreases at higher CO$_2$ flow. The spin density (Fig. 7.6(b)) stays at a few 10^{18} cm^{-3} at low CO$_2$ flow, then goes up to 8×10^{19} cm^{-3} at CO$_2$ flow = 2.5 sccm. Meanwhile, the *g*-value (Fig. 7.6(c)) is shifted monotonically from *g* = 1.998 (CE-resonance" in *n*-type μc-Si:H) to *g* = 2.0043 (Si-db in a-SiO$_x$:H matrix).

In Fig. 7.6, one may notice that the ESR spectrum of the film sample with CO$_2$ flow = 1.5 sccm looks different with its counterpart powder sample in Fig. 7.1. This may be due to the background signal from the glass substrate.

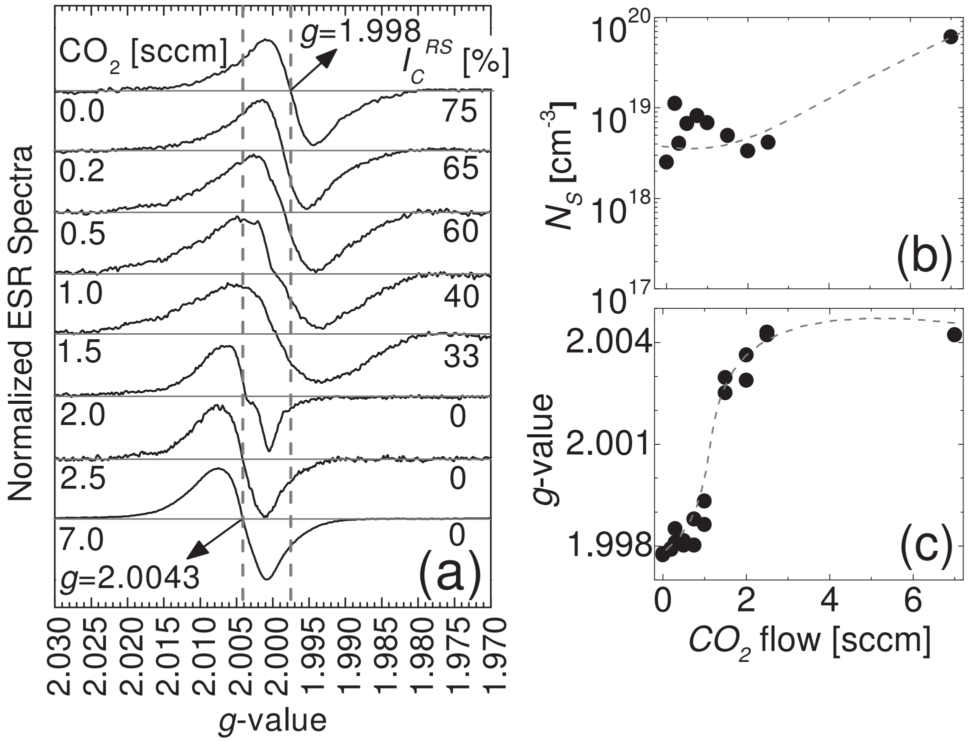

Figure 7.6 *(a) Normalized ESR spectra of μc-SiO$_x$:H layers (1/ 500/ CO$_2$ = 0.0…7.0 sccm/ 2%/ no seed); (b) Spin density and (c) g-value vs. CO$_2$ flow.*

All the results shown above demonstrate that CO$_2$ in the precursor gases as the source of oxygen has significant effects on the properties of PH$_3$-doped μc-SiO$_x$:H films. With increasing oxygen incorporation, the following phenomena were observed:

- Films varied from highly crystalline μc-Si:H to amorphous silicon oxide ($I_C^{RS} \approx 80 - 0\%$);
- The optical bandgap (E_{04}) increases from 2.0 to 2.8 eV with a reduction of the optical absorption at lower photon energies;
- The ESR spin density (N_S) increases from 3×10^{18} to 8×10^{19} cm^{-3};
- The paramagnetic defects varies from the CE-resonance to Si-db-like defects in a-SiO$_x$:H;
- As is shown in Fig. 7.7, the electrical conductivity is reduced by 14 orders of magnitude from 10^{1} to 10^{-13} S/cm along with the simultaneous reduction in film crystallinity.

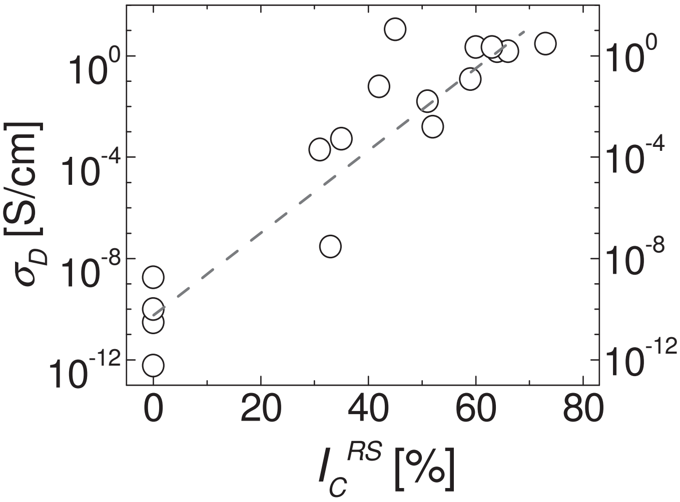

Figure 7.7 *Electrical dark conductivity σ_D vs. Raman crystallinity I_C^{RS} for μc-SiO$_x$:H layers (1/ 500/ CO_2 = 0.0…7.0 sccm/ 2%/ no seed).*

7.3.2 Effect of PH_3-doping

PH_3-doping is required to offer sufficient conductivity for both the intermediate reflector layer (IRL) and window layer in thin-film Si solar cells. And effective PH_3-doping is believed to take place in the μc-Si:H crystallites rather than in a-SiO$_x$:H. In this section, the effects of PH_3-doping on the structural, electronic and ESR properties will be investigated.

Similar to μc-Si:H and a-Si:H prepared by the PECVD technique using SiH_4 and H_2 as source gases, the silane concentration (SC) which determines the film crystallinity is defined as the ratio of the SiH_4 gas flow to the total gas flow of SiH_4 and H_2:

$$SC = \frac{[SiH_4]}{[SiH_4]+[H_2]}$$

Here, in the case of PECVD-prepared μc-SiO$_x$:H using SiH_4, CO_2 and H_2 as source gases, the silane plus carbon dioxide concentration (SOC), which is the key parameter to decide the material crystallinity, is calculated as follows:

$$SOC = \frac{[SiH_4]+[CO_2]}{[SiH_4]+[CO_2]+[H_2]}$$

Fig. 7.8 represents the ESR spectra for both *i*- and *n*-type μc-SiO$_x$:H series. All the spectra were normalized to the same maximum intensity for lineshape comparison. The first two spectra with SOC = 0.002 represent the highly crystalline μc-Si:H. In *i*-type μc-Si:H the dominant defect is the Si-db, while in *n*-type μc-Si:H is the CE resonance (g = 1.998).

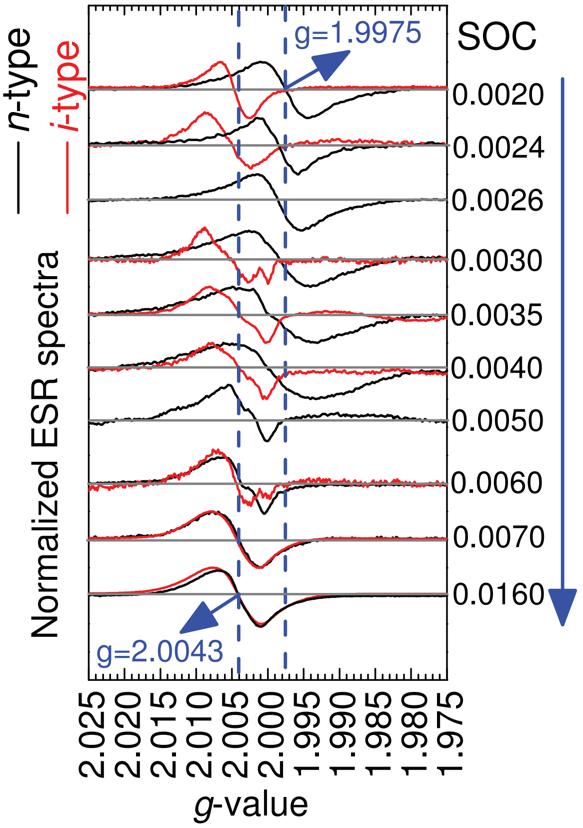

Figure 7.8 *ESR spectra measured at 40 K for both intrinsic (1/ 500/ CO$_2$/ 0%/ no seed, red) and PH$_3$-doped ((1/ 500/ CO$_2$/ 2%/ no seed, black) μc-SiO$_x$:H films with increasing SOC.*

At SOC = 0.002 – 0.007, PH$_3$-doping leads to the shift of the ESR resonance center towards a lower value; when SOC ≥ 0.007, *i*- and *n*-type μc-SiO$_x$:H show the same ESR spectra. In both series, with increasing SOC, a slight increase in H_{PP} from about 7 to 11 G, and a shift of the g-value from 2.005 to 2.0043 in *i*-type while 1.9975 to 2.0043 in *n*-type μc-SiO$_x$:H were observed. The spectra for samples with SOC = 0.003 – 0.006 suffer from the background signal of the glass substrates due to a relatively low N_S and limited volume of the thin-film samples.

The ESR spectra of *i*-type and *n*-type series at SOC ≥ 0.007 look identical despite of the doping, a featureless single resonance with a shape similar to the resonances in intrinsic a-Si:H [Stutzmann1989] and μc-Si:H [Finger1998] has been observed. In the PH$_3$-doped material, no P-related hyperfine structures were observed like in μc-Si:H (hyperfine splitting: *hf* = 110 G) [Müller1999], a-Si:H (*hf* = 245 G) [Stutzmann1987], silica (*hf* = 310 G) [Pawlak1999], or Si nanoparticles embedded in SiO$_2$ (*hf* = 80 G) [Makimura2002].

The corresponding ESR spin density N_S and *g*-values are presented in Fig. 7.9(c) and (d). N_S in *i*-type material increases from 10^{17} to 3×10^{19} cm^{-3} as SOC value increases from 0.002 to 0.016; in *n*-type material μc-SiO$_x$:H, N_S increases about 1 order of magnitude only, from few times 10^{18} cm^{-3} to about 6×10^{19} cm^{-3}.

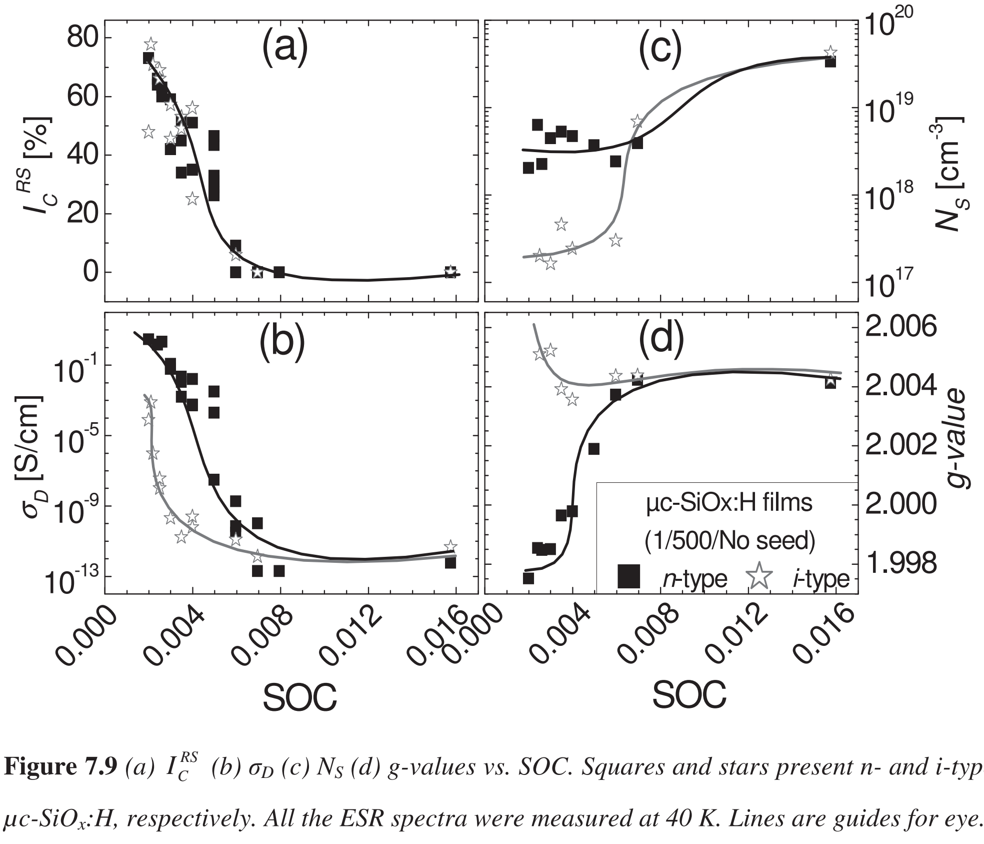

Figure 7.9 *(a)* I_C^{RS} *(b)* σ_D *(c)* N_S *(d) g-values vs. SOC. Squares and stars present n- and i-type μc-SiO$_x$:H, respectively. All the ESR spectra were measured at 40 K. Lines are guides for eye.*

Thin film crystallinity I_C^{RS} and electrical conductivity σ_D are plotted as a function of SOC in Fig. 7.9(a) and (b). In both *i*- and *n*- series, the crystallinity of the material decreases from 80 to 0% as SOC increases from 0.002 to around 0.007. In the same SOC range where a crystalline phase is present in the material, major changes in σ_D take place. σ_D decreases by 9 orders of magnitude in intrinsic and 13 orders of magnitude in doped material. From high crystallinity to medium crystallinity (I_C^{RS} = 20–50%), *n*-type μc-SiO$_x$:H is about 4 to 8 orders of magnitude more conductive than the *i*-type counterpart. At SOC ≥ 0.007, no crystallinity was observed (I_C^{RS} = 0%), and σ_D in both *i*-type and *n*-type samples has the same values between $10^{-10} – 10^{-12}$ S/cm.

Further conclusions can be made by combining the results of crystallinity, conductivity and ESR properties (spin density, *g*-value and lineshape). PH$_3$-doping is only effective at SOC < 0.007; when SOC ≥ 0.007, no μc-Si:H phase exists, and the PH$_3$-doping is not effective any more. It can be seen from Fig. 7.10 where (a) the optical bandgap E_{04} and (b) the electrical conductivity are plotted as a function of the film crystallinity for both *i*- and *n*-type μc-SiO$_x$:H samples.

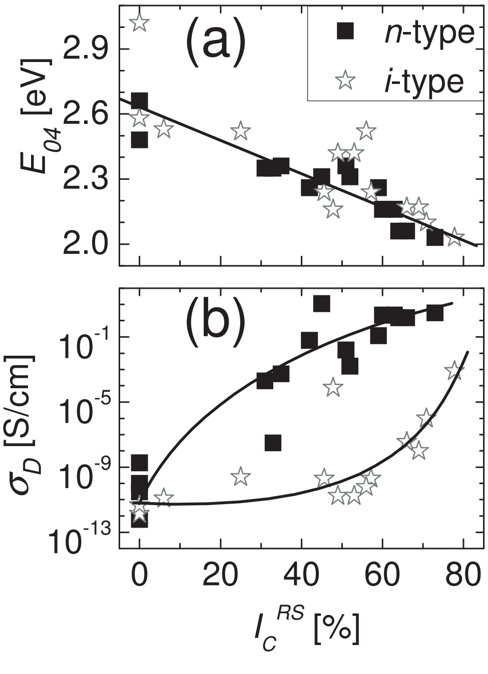

Figure 7.10 *Dependence of (a) optical bandgap E_{04} and (b) conductivity σ_D on material crystallinity I_C^{RS} for both i- (stars) and n-type (squares) μc-SiO$_x$:H. Lines guide for eyes.*

From Fig. 7.10(a) one can see that for both *i*- and *n*-type µc-SiO$_x$:H, the optical bandgap E_{04} gradually decreases in a linear way from about 2.6 to 2.0 eV as the material changes from a-SiO$_x$:H to highly crystalline µc-Si:H. As shown in Fig. 7.10(b), σ_D changes slightly within the range of 10^{-12} – 10^{-10} S/cm in undoped material with $I_C^{RS} < 50\%$. In this region, the electronic transport is likely dominated by the highly resistive a-SiO$_x$:H phase. For samples with $I_C^{RS} > 50\%$, σ_D increases sharply with the increase of crystallinity. In this region, the µc-Si:H fraction is expected to play a major role in the electronic transport. At $I_C^{RS} = 20\ldots60\%$, a difference in σ_D of *i*- and *n*-type material reaches 8 orders of magnitude is observed. This suggests an effective phosphorous doping.

7.3.3 Effect of hydrogen dilution ([SiH$_4$]:[H$_2$])

It's known that hydrogen plays a crucial role in formation of a-Si:H [Cabarrocas1999], µc-Si:H [Vetterl2000], and Si alloys like silicon carbide (SiC:H) [Henry2001], silicon oxide (SiO$_x$:H) [Quaresima1987; Lambertz2011] and silicon nitride (SiN$_x$:H) [Ueda1999]. In SiO$_x$, H has been reported to exist in different forms, such as H-termination of Si atoms on the surface, bonding with Si in SiH$_x$ (x = 0, 1, 2, 3.) radicals, and H$_2$ in voids [Janotta2004].

Extensive research into the influence of [SiH$_4$]:[H$_2$] gas ratio on the growth of hydrogenated silicon has been reported [Tsai1988; Houben1998; Moutinho2003]. It had been demonstrated that upon increasing the ratio of [SiH$_4$]:[H$_2$], µc-Si:H with a high degree of crystallinity changes towards amorphous films with small irregularly shaped grains.

This section focuses on the discussion of the effects of H$_2$ on the microstructure, electrical dark conductivity, ESR properties and optical absorption of µc-SiO$_x$:H material.

Fig. 7.11(a) and (b) shows the dependence of thin film crystallinity and electrical conductivity on SOC for different [SiH$_4$]:[H$_2$] gas ratio series. With increasing SOC, all the µc-SiO$_x$:H samples show the microstructure transition from highly crystalline µc-Si:H to amorphous silicon oxide ($I_C^{RS} \approx 0\%$, $\sigma_D \approx 10^{-13}$ S/cm).

Fig. 7.11(a) shows that for a higher SiH$_4$:H$_2$ dilution, the microcrystalline – amorphous transition happens at higher SOC values at a narrower SOC range. At the same SOC value, samples with higher [SiH$_4$]:[H$_2$] gas ratio have higher crystallinity. This trend is also observed for the electrical conductivity in Fig. 7.11(b)) and the ESR spin density (Fig. 7.11(c)). As the material changes from highly crystalline silicon (with $I_C^{RS} \approx 75\%$ for the [SiH$_4$]:[H$_2$] = 1/ 500 and 2/500 series, $I_C^{RS} \approx 50\%$ for the [SiH$_4$]:[H$_2$] = 1/1000 series) to a-SiO$_x$:H with $I_C^{RS} \approx 0\%$, for all three series, σ_D ranges from a few times 10^0 (10^{-7} for the [SiH$_4$]:[H$_2$] = 1/1000 series) to 10^{-13} S/cm, which is the detection limit of the conductivity system. N_S changes correspondingly from a few times 10^{18} to 10^{19} cm^{-3}, and the *g*-value (Fig. 7.16(d)) from 1.9977 to 2.0043.

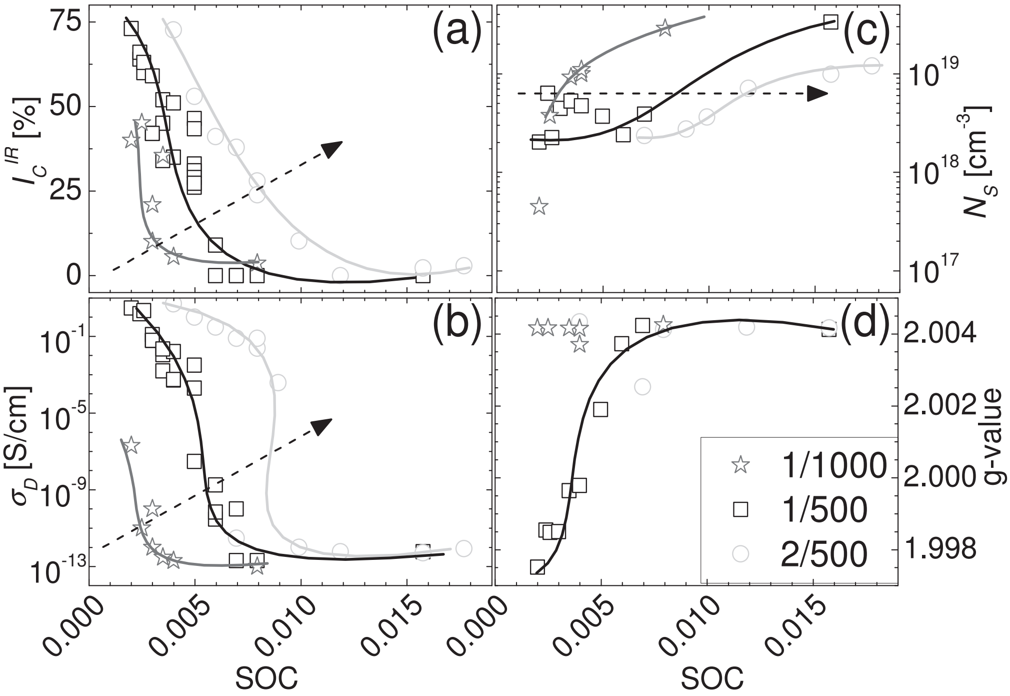

Figure 7.11 *(a)* I_C^{RS} *(b)* σ_D *(c)* N_S *and (d) g-values vs. SOC for n-type μc-SiO*$_x$*:H films with [SiH*$_4$*]:[H*$_2$*] = 2/500, 1/500 and 1/1000. Arrows indicate the increase of [SiH*$_4$*]:[H*$_2$*] ratio.*

The optical bandgap (E_{04}) is plotted versus the SOC values for different [SiH$_4$]:[H$_2$] gas ratio series in Fig. 7.12. Starting from the *n*-type μc-Si:H which has E_{04} = 2.0 eV, E_{04} increases with the oxygen incorporation.

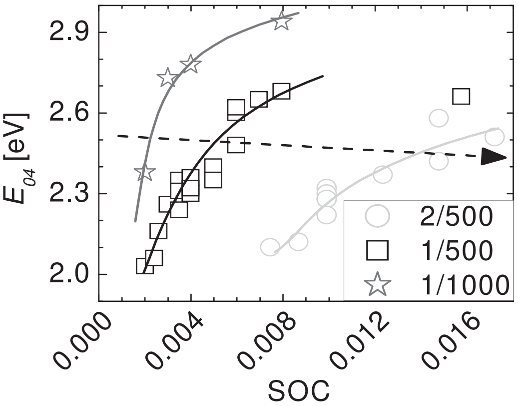

Figure 7.12 *Dependence of E_{04} on SOC. Circles, squares and stars represent n-type doped μc-SiO$_x$:H samples with the [SiH$_4$]:[H$_2$] ratios of 2/500, 1/500 and 1/1000, respectively. The arrow indicates the increase of the [SiH$_4$]:[H$_2$] ratio.*

All these results suggest that high H$_2$-gas flow promotes film nucleation and higher electrical conductivity. At the same time, the ESR spin density is reduced by less than one order of magnitude. As SOC increases, the ESR-detected paramagnetic defects evolve from the CE-resonance in highly crystalline *n*-type μc-Si:H (g = 1.998) to the Si-dbs in an a-SiO$_x$:H microstructural environment (g = 2.0043).

7.3.4 Effect of seed layer

For the use as both the window layer and the intermediate reflector layer in a-Si:H (top cell) /μc-Si:H (bottom cell) *p*-*i*-*n* tandem cells, μc-SiO$_x$:H is deposited on the amorphous *n*-layer during the solar cell fabrication. To promote nucleation of μc-SiO$_x$:H films, a highly crystalline μc-Si:H thin layer (thickness ≤ 30 nm) has been developed (by A. Lambertz) as a seed layer using PECVD at 13.56 MHz.

For material investigation, μc-SiO$_x$:H films (1/ 200/ CO$_2$ = 0.0…7.0 sccm/ 2%/ seed) with *i*-type, *n*-type or without μc-Si:H seed layers were grown on glass substrates. Films have a thickness of 600…1100 nm, while the thickness of the seed layer was around 30 nm. Fig. 7.13(a) shows the μc-SiO$_x$:H thin film crystallinity evaluated from Raman spectroscopy. No differences could be resolved in the general trend between films with and without seed layer, only a slightly higher crystallinity in the series with *i*-seed layer could be observed.

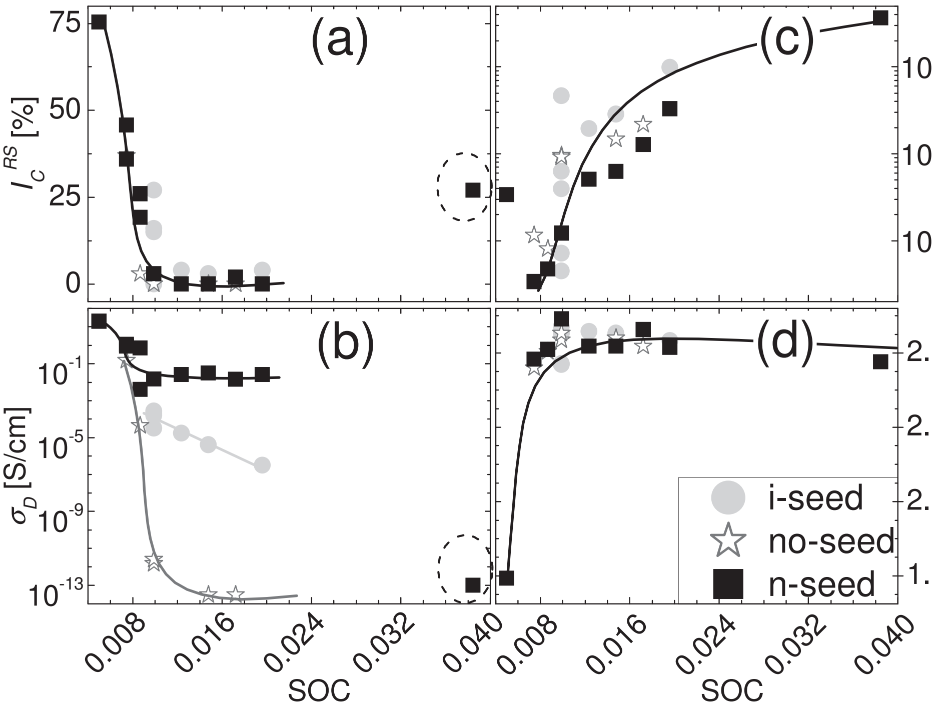

Figure 7.13 Seed layer effects: *(a)* I_C^{RS} *(b)* σ_D *(c)* N_S *and (d) g-values vs. SOC for μc-SiO*$_x$*:H films (1/ 200/ CO*$_2$ *= 0.0…7.0 sccm/ 2%/ seed) with i-, n-type or without μc-Si:H seed layers.*

In Fig. 7.13(b), a significant influence of the seed layers on the electrical conductivity is observed. Especially for those samples with SOC > 0.01 which turn out to be amorphous ($I_C^{RS} \approx$ 0%), films without seed layer have $\sigma_D < 10^{-13}$ S/cm, which is much lower than the counterparts with *i*- and *n*-type seed layer, which has $\sigma_D = 10^{-5}$ and 10^{-1} S/cm, respectively.

But for material close to the microcrystalline – amorphous transition region, the use of microcrystalline Si seed layers promotes the formation of the crystalline phase. Raman spectra are shown in Fig. 7.14. The μc-Si:H seed layer leads to an overestimation of crystallinity of the material which has the highest SOC = 0.0385 and is assumed to be a-SiO$_x$:H. The detected crystalline phase is due to the seed layer.

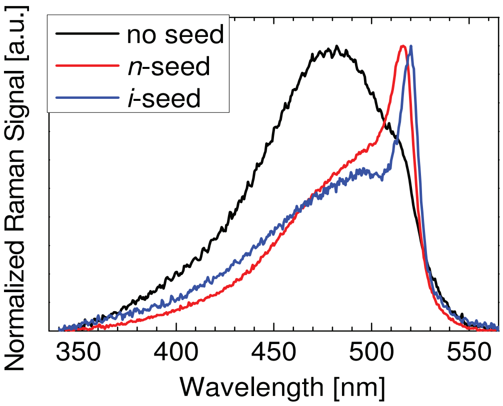

Figure 7.14 *Raman spectra for μc-SiO$_x$:H films deposited with SOC = 0.008 on standard glass substrate with i-type (blue), n-type (red) or without (black) seed layer.*

However, this conductivity also includes the conductivity of the seed layer. As is shown in Fig. 7.15, two pathways are available for the electrical current between two Ag contacts – One is through the conductive μc-Si:H crystallites in the phase-mixture μc-SiO$_x$:H film, the other is through the seed layer. The more amorphous the μc-SiO$_x$:H is, the less conductive it would be, the more dominant the seed layer is in the conductivity. Therefore, in this case, the influence of the seed layer on the electrical conductivity of the intermediate reflector material cannot be evaluated simply by planar conductivity measurements with two Ag contacts on the film surface. But when applied as the intermediated reflector layer in a-Si:H/μc-Si:H tandem solar cells, the improvement of cell performance from the seed layer has proven to be significant [Lambertz2007; Grundler2010; Lambertz2011].

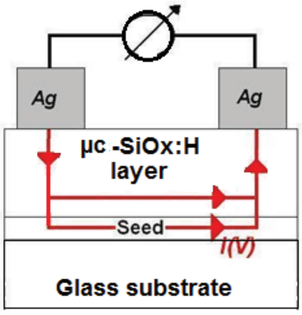

Figure 7.15 *Seed layer behaves as a short cut for electrical current in μc-SiO$_x$:H films.*

The 30 nm-thick highly crystalline μc-Si:H seed layer causes no differences in the ESR spin density or *g*-values of μc-SiO$_x$:H films in the whole CO_2 variation range as exhibited in Fig. 7.13(c) and (d).

Comparing N_S for μc-SiO$_x$:H samples in Fig. 7.13(c) with 1/ 200/ CO_2/ 2%/ no seed to Fig. 7.9(c) and Fig. 7.11(c) with 1/ 500/ CO_2/ 2%/ no seed, one may find a much lower N_S in the SiH_4 = 200 sccm series (a few times 10^{16} –10^{17} cm^{-3}) than in the SiH_4 = 500 sccm series (a few times 10^{18} cm^{-3}). This is in agreement with the discussion of the effects of SiH_4:H_2 dilution on the ESR spin density (shown in Fig. 7.11(c)) – when the SOC is the same, the higher the gas ratio of [SiH_4]:[H_2] is, the lower the spin density is.

7.4 Summary and conclusions

The primary aim of this chapter was to investigate PH_3-doped μc-SiO$_x$:H films that can possibly be used as both the window layer and the intermediate reflector layer in a-Si:H/μc-Si:H tandem cells. Films were prepared over a wide range of deposition parameters, such as oxygen incorporation (varying CO_2 gas glow), PH_3-doping, [SiH_4]:[H_2] gas ratio (1/1000, 1/500, 2/500) and different seed layers (no-, *i*-type, *n*-type highly crystalline μc-Si:H seed layer).

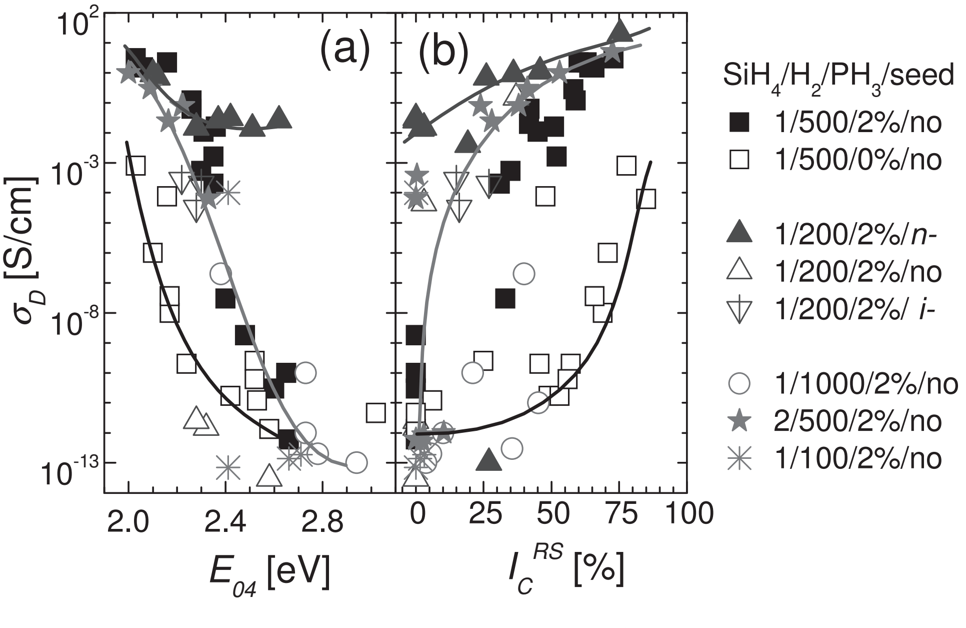

Figure 7.16 *Correlations between* σ_D *and* E_{04} *(a) and* I_C^{RS} *(b). Lines are guides for eye.*

Fig. 7.16 shows the dependence of σ_D on E_{04} and I_C^{RS} . As E_{04} increases from 2.0 to 3.0 eV, σ_D drops by 14 orders of magnitude from 10^1 to less than 10^{-13} S/cm. As the crystallinity increases from 0% (a-SiO$_x$:H) to 75% (μc-Si:H), the conductivity σ_D increases by 14 orders of magnitude from 10^{-13} to less than 10^1 S/cm..

Besides optical bandgap and material crystallinity, the third factor that would impact the electrical conductivity is the defect density, especially the paramagnetic defects within the band gap and/ or band-tail states. In Fig.7.17, σ_D is plotted as a function of paramagnetic spin density (N_S). In each series, a decreasing trend of σ_D with increasing N_S is observed.

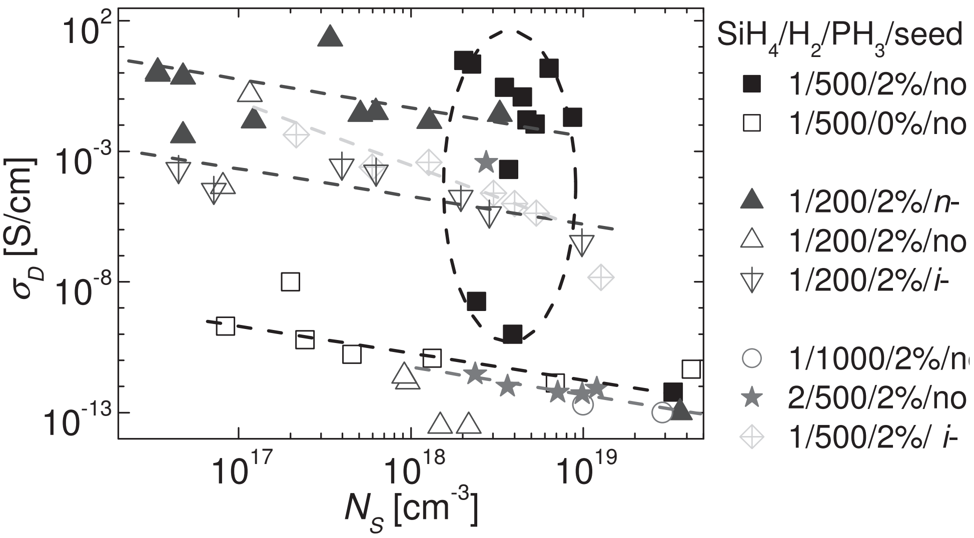

Figure 7.17 *Correlations between σ_D and N_S. Lines are guide for each series.*

One may notice that for the series of *n*-type μc-SiO$_x$:H samples with SiH$_4$:H$_2$ = 1/500 dilution without seed layer, N_S always keeps at a high level ($N_S = 2\times10^{18}\ldots10^{19}$ cm^{-3}), but still samples show a relatively high conductivity of $\sigma_D > 10^{-4}$ S/cm and a *g*-value close to 1.998 (CE-resonance). An efficient *n*-type doping can be concluded from this. The high spin density is due to the PH$_3$-doping induced free electrons [Janotta2004]. For a-SiO$_x$:H samples (I_C^{RS} ≈0%), the high spin density is attributed to the Si-dangling bonds in the disordered silicon oxide phase.

A plot of N_S on E_{04} and I_C^{RS} can be found in Fig. 7.18. One may notice that the data points in Fig. 7.18 and Fig. 7.16 are not always exactly corresponding to those in Fig. 7.17. This is due to the fact that for some very thin samples with low spin density, ESR signals from the glass substrates are even stronger than that of the material. This makes it very difficult to calculate N_S from the very noisy ESR signals. However, the electrical dark conductivity, Raman crystallinity and optical absorption are still available even for very thin samples.

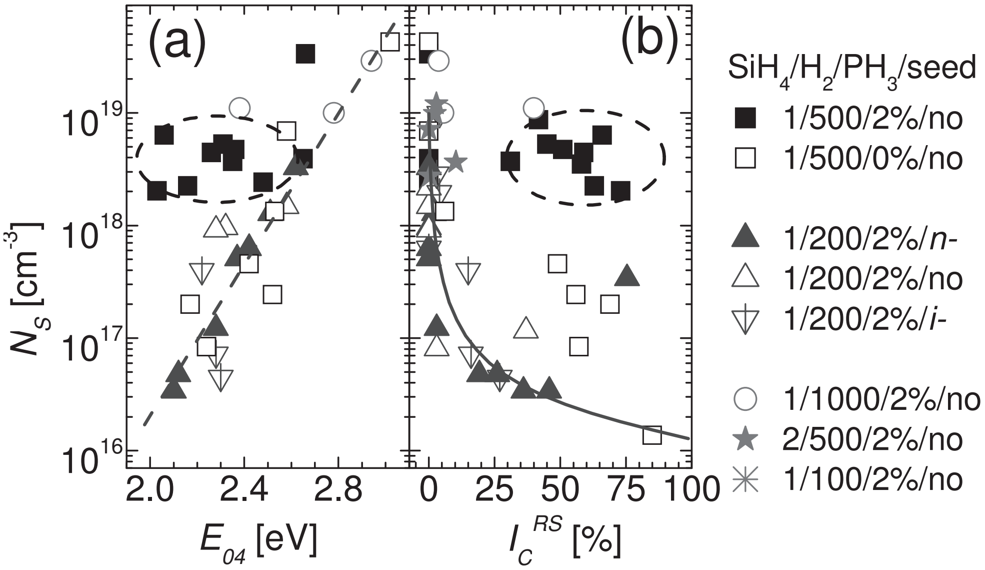

Figure 7.18 *Correlations between N_S and E_{04} (a) and I_C^{RS} (b). Lines are guide for eye.*

In Fig. 7.18(a) N_S increases by three orders of magnitude from a few times 10^{16} to 10^{19} cm^{-3} as E_{04} increases from 2.0 to 3.0 eV. A big data scattering is found when N_S is plotted as a function of I_C^{RS} in Fig. 7.18(b). A general trend shows a decrease of N_S as the material becomes more crystalline. As an exception, µc-SiO$_x$:H samples with 1/ 500/ CO$_2$ = 0…7 sccm/ 2%/ no seed always have a high N_S.The conductivity in µc-SiO$_x$:H critically depends on the crystallinity. At I_C^{RS} = 0%, the material is a-SiO$_x$:H with a very high spin density ($N_S = 10^{18} – 10^{19}$ cm^{-3}), high oxygen content ($x \approx 1.5$) and wide band gap ($E_{04} \approx 2.8$ eV) and is reported to be insensitive to doping [Janotta2004]. The increase of crystallinity is accompanied by a dramatic increase of conductivity. The most crystalline material is µc-Si:H deposited without CO$_2$, and the conductivity values are typical for *n*- and *i*-type μc-Si:H [Finger1998; Tzolov1997]. The transition between these extreme cases has different character for doped and intrinsic material. In undoped material at $I_C^{RS} < 50\%$, σ_D changes slightly within the range of $10^{-12}\ldots10^{-10}$ S/cm, which is likely related to a slight decrease of the bandgap. In this region the electronic transport is probably dominated by the resistive amorphous silicon oxide phase. In the region of $I_C^{RS} > 50\%$, the conductivity increases sharply with increasing crystalline volume fraction. In this region the μc-Si:H fraction is expected to play a major role in the electronic transport and increase in crystallinity to promote the electrical conductivity.

In contrast to undoped samples, strong variations of the *g*-value in the resonances of PH_3-doped material suggest a qualitative change in the type of paramagnetic centers observed. Without oxygen incorporation, the spectrum is a CE-resonance in *n*-type μc-Si:H, which was suggested to originate from conduction electrons and/or electrons located in the conduction band tail [Finger1994; Lips2002]. This is consistent with the high conductivity in these films. A reduction of crystallinity is accompanied by the decrease of conductivity and increase of the effective *g*-value of the ESR spectra. The more amorphous the material is, the more the ESR spectra of the doped material are identical to the spectra of intrinsic material with $g = 2.0043$. The shift of the *g*-value between 1.998 and 2.0043 is related to the shift of the Fermi level and the loss of crystallinity (CE-resonance is observed in μc-Si:H phase only [Finger1998]). In the transition region with moderate crystallinity the *g*-value is between 1.998 and 2.0043 and the peak to peak linewidth is significantly higher (20 G) than at high and zero crystallinity (both around 11 G). Interestingly, these spectra in the transition region cannot be satisfactorily represented by a superposition of the CE-resonance ($g = 1.998$) and the resonance of amorphous material at $g = 2.0043$, mostly because of a broad wing of the resonance from samples with moderate crystallinity. In this case, a relatively high σ_D suggests that the Fermi level in amorphous phase has its position above midgap.

All the data indicate that crystallinity determines doping efficiency and electrical conductivity of μc-SiO$_x$:H, which is in line with viewing μc-SiO$_x$:H as a mixture of μc-Si:H crystallites embedded in an a-SiO$_x$:H matrix.

Appendix A: Thin film deposition parameters

Deposition parameters for undoped μc-SiC:H thin films

(These samples are mostly from Dr. Stefan Klein, Dr. Yuelong Huang and Dr. Arup Dasgupta)

n-type SiC	Sample number	Filament tempearture	Substrate temperature	Deposition pressure	Monomethyl-silane concentration	Film thickness
Series		T_F [°C]	T_S [°C]	p [Pa]	c_{MMS} [%]	d [nm]
T_{F1}	06C030	1750	400	75	0.3	420
	06C173	1750	400	75	0.3	226
	06C195	1800	400	75	0.3	192
	06C040	1825	400	75	0.3	400
	06C036	1900	400	75	0.3	310
	06C178	1900	400	75	0.3	199
	06C047	2000	400	75	0.3	350
	06C163	2000	400	75	0.3	175
	06C039	2100	400	75	0.3	240
	06C172	2100	400	75	0.3	185
T_{F2}	07C362	1800	275	75	0.3	160
	08C092	1800	275	75	0.3	207
	07C375	1900	275	75	0.3	160
	08C088	1900	275	75	0.3	162
	07C358	2000	275	75	0.3	160
	08C086	2000	275	75	0.3	178
	08C102	2050	275	75	0.3	133
	07C385	2100	275	75	0.3	160
	08C094	2100	275	75	0.3	161
	08C110	2150	275	75	0.3	154
	08C093	2200	275	75	0.3	180
c_{MMS}	06C355	2000	275	75	0.3	69
	06C348	2000	275	75	0.6	97
	06C347	1900	200	75	1	279
	06C346	1900	200	75	1.5	550
	06C345	1900	200	75	2	669
	06C192	2000	225	75	0.3	154
T_S	06C053	2000	260	75	0.3	300
	07C358	2000	275	75	0.3	160
	08C086	2000	275	75	0.3	178
	06C050	2000	340	75	0.3	367

	06C184	2000	350	75	0.3	195
	06C047	2000	400	75	0.3	350
	06C058	2000	440	75	0.3	260
	06C062	2000	440	75	0.3	241
	06C054	2000	480	75	0.3	264
	06C074	2000	480	75	0.3	245
	06C175	2000	480	75	0.3	188
	06C057	2000	550	75	0.3	257
p	06C356	2000	400	2	0.3	100
	06C357	2000	400	5	0.3	200
	06C358	2000	400	10	0.3	300
	06C359	2000	400	20	0.3	200
	06C163	2000	400	75	0.3	175

Deposition parameters for Al-doped μc-SiC:H thin films

(These samples are mostly from Dr. Tao Chen)

p-type SiC	Sample number	Filament temperature	Substrate temperature	Deposition pressure	Monomethyl-silane concentration	Al-doping ratio
Series		T_F [°C]	T_S [°C]	p [Pa]	c_{MMS} [%]	p_{TMAl}/p_{MMS}
$\frac{p_{TMAl}}{p_{MMS}}$	08H014	2200	300	75	0.6	0.0000
	08H026	2170	300	75	0.6	0.0077
	08H017	2170	300	75	0.6	0.0155
	08H016	2170	300	75	0.6	0.0309
	08H019	2170	300	75	0.6	0.0464
	08H015	2170	300	75	0.6	0.0619
	08H018	2170	300	75	0.6	0.0928
	08H020	2170	300	75	0.6	0.1237
	08H022	2170	300	75	0.6	0.1547
T_F	08O110	2080	347	200	0.3	0.0495
	08O112	2140	350	200	0.3	0.0495
	09O001	2170	345	200	0.3	0.0495
	09O005	2150	343	200	0.3	0.0495
	09O006	2200	349	200	0.3	0.0495
	09O002	2220	347	200	0.3	0.0495
T_S	08H030	2170	365	75	0.6	0.0309
	08H032	2170	340	75	0.6	0.0309
	08H033	2170	391	75	0.6	0.0309
	08H034	2170	329	75	0.6	0.0309
	08H035	2170	319	75	0.6	0.0309
	08H037	2170	272	75	0.6	0.0309
p	08H097	2300	322	30	0.3	0.0619
	08H100	2180	330	75	0.3	0.0619

	08H102	2415	316	10	0.3	0.0619
	08H103	2155	332	100	0.3	0.0619
	08H104	2120	348	150	0.3	0.0619
	08H105	2100	346	200	0.3	0.0619
	08H106	2090	342	280	0.3	0.0619
	08H107	2090	343	250	0.3	0.0619

Deposition parameters for μc-SiO$_x$:H thin films

(These samples are mostly prepared by Andreas Lambertz and Lihong Xiao)

Groups	Sample number	SiH_4	H_2	CO_2	Thickness	Seed
		[sccm]	[sccm]	[sccm]	[nm]	[Min]
Group 1	08b130	1	500	1	638	3.5 /VHF *i*
	08b148	1	500	1.5	869	3.5 /VHF *i*
	08b245	1	500	1.5	30	3.5 /VHF *i*
	08b234	1	500	1.5	41	3.5 /VHF *i*
	08b252	1	500	1.5	68	3.5 /VHF *i*
	08b248	1	500	1.5	97	3.5 /VHF *i*
	08b134	1	500	2	796	3.5 /VHF *i*
	08b151	1	500	2.5	818	3.5 /VHF *i*
	08b132	1	500	3	759	3.5 /VHF *i*
	08b152	1	500	3.5	774	3.5 /VHF *i*
	08b136	1	500	4	906	3.5 /VHF *i*
	08b162	1	500	5	753	3.5 /VHF *i*
	08b164	1	500	7	798	3.5 /VHF *i*
Group 2	08B523	1	500	0	500	0
	08B521	1	500	0.2	421	0
	08B528	1	500	0.2	1137	0
	08B522	1	500	0.3	439	0
	08B529	1	500	0.3	1536	0
	08b033	1	500	0.5	326	0
	09B037	1	500	0.5	874	0
	10B428	1	500	0.5	powder	0
	07b137	1	500	0.75	255	0
	09B038	1	500	0.75	1055	0
	07b142	1	500	1	270	0
	09B039	1	500	1	890	0
	07b141	1	500	1.5	325	0
	09B043	1	500	1.5	772	0
	10B429.I	1	500	1.5	powder	0
	10B429.II	1	500	1.5	powder	0
	07b144	1	500	2	407	0
	09B044	1	500	2	935	0

	07b146	1	500	2.5	428	0
	09B047	1	500	7.0	600	0
Group 3	09B383	1	200	0	912	3.5/VHF *n*
	08b048	1	200	0.5	907	3.5/VHF *n*
	09B380	1	200	0.5	734	3.5/VHF *n*
	08b047	1	200	0.75	804	3.5/VHF *n*
	09B382	1	200	0.75	756	3.5/VHF *n*
	07b261	1	200	1	836	3.5/VHF *n*
	07b264	1	200	1.5	704	3.5/VHF *n*
	07b278	1	200	2	1038	3.5/VHF *n*
	08b044	1	200	2.5	1031	3.5/VHF *n*
	07b281	1	200	3	1060	3.5/VHF *n*
	09B379	1	200	7	1334	3.5/VHF *n*
Group 4	08b025	1	200	0.5	630	0
	08b026	1	200	0.75	634	0
	07b292	1	200	1	694	0
	07b310	1	200	1	756	0
	07b319	1	200	2	794	0
	08b023	1	200	2.5	986	0
Group 5	08b120	1	200	1	635	3.5 /VHF *i*
	08b207	1	200	1	70	3.5 /VHF *i*
	08b215	1	200	1	93	3.5 /VHF *i*
	08b213	1	200	1	101	3.5 /VHF *i*
	08b122	1	200	2	927	3.5 /VHF *i*
	08b128	1	200	1.5	777	3.5 /VHF *i*
	08b119	1	200	3	1126	3.5 /VHF *i*
Group 6	08B519	1	500	0.0	powder	0
	07B011	1	500	0.0	1341	0
	09B128	1	500	0.05	880	0
	09B120	1	500	0.10	950	0
	09B017	1	500	0.25	930	0
	09B130	1	500	0.25	1030	0
	07B013	1	500	0.5	626	0
	09B033	1	500	0.5	831	0
	09B014	1	500	0.75	1684	0
	09B022	1	500	0.75	522	0
	07B018	1	500	1.0	556	0
	09B013	1	500	1.0	666	0
	07B015	1	500	2.0	832	0
	09B016	1	500	2.5	912	0
	09B018	1	500	7.0	750	0

Group 7	09b241	1	1000	0.00	0	0
	09b225	1	1000	1.00	235	0
	09B371	1	1000	1.00	431	0
	09b295	1	1000	1.50	315	0
	09b364	1	1000	1.50	388	0
	09b235	1	1000	2.00	341	0
	09b230	1	1000	2.00	339	0
	09b303	1	1000	2.50	375	0
	09B368	1	1000	2.50	772	0
	09B374	1	1000	3.00	600	0
	09b239	1	1000	3.00	447	0
	09b244	1	1000	7.00	537	0
Group 8	09b344	2	500	0.00	588	0
	09b325	2	500	0.50	598	0
	09b322	2	500	1.00	560	0
	09b541	2	500	1.00	370	0
	09b328	2	500	1.50	560	0
	09b316	2	500	1.50	1652	0
	09b358	2	500	2.00	407	0
	09b318	2	500	2.00	311	0
	09b376	2	500	2.50	452	0
	09B378	2	500	2.75	555	0
	09b337	2	500	3.00	305	0
	09b340	2	500	4.00	401	0
	09b343	2	500	6.00	431	0
Group 9	09B546	1	100	0.00	1326	0
	09B563	1	100	0.25	440	0
	09B435	1	100	0.50	481	0
	09B558	1	100	0.75	486	0
	09B426	1	10	1.00	550	0
	09B430	1	100	2.00	620	0
	09B434	1	100	3.00	720	0

Appendix B: ESR spectra of μc-SiO$_x$:H thin films

In this section, ESR spectra for all the 9 groups of μc-SiO$_x$:H thin films that suffered from the glass substrates influences are given. Both the raw data (As-measured spectra) and spectra after glass signal subtraction are presented.

Group 1: 1/ 500/ CO$_2$ = 0…7.0 sccm/ 2%/ *i*-type seed

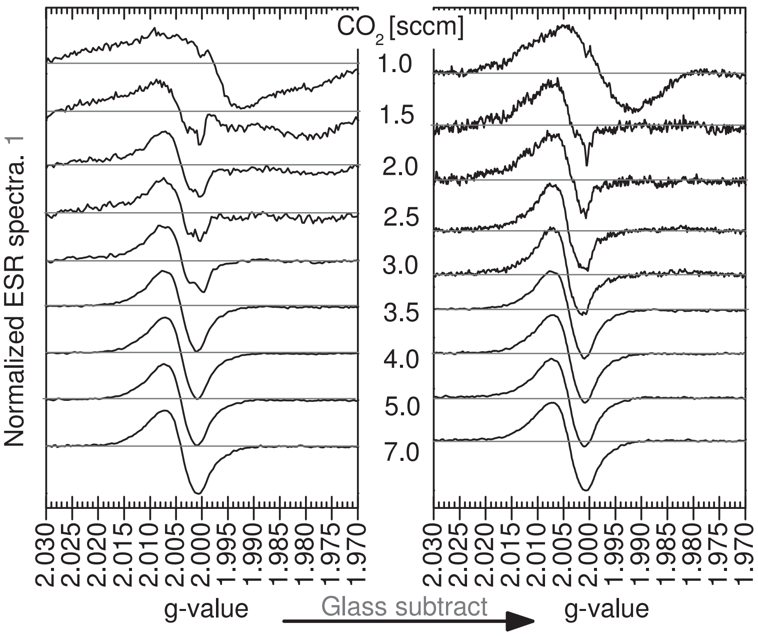

Group 2: 1/ 500/ CO_2 = 0…7.0 sccm/ 2%/ no seed layer

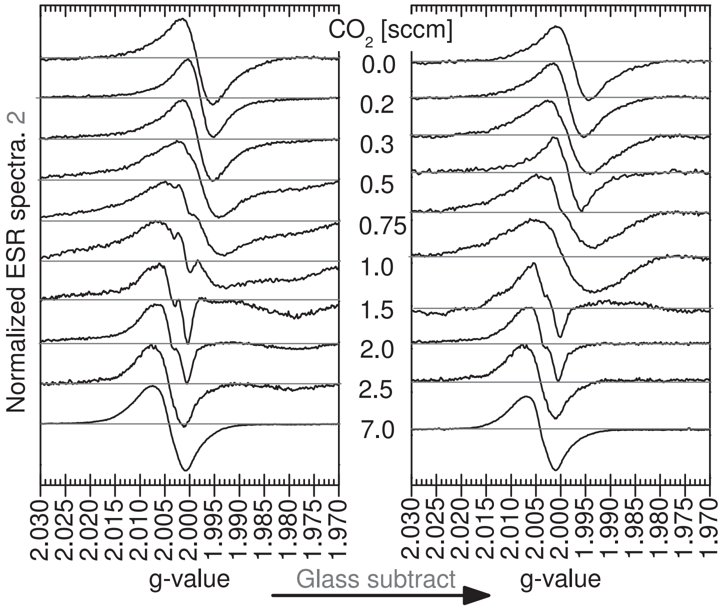

Group 3: 1/ 200/ CO_2 = 0…7.0 sccm/ 2%/ *n*-type seed

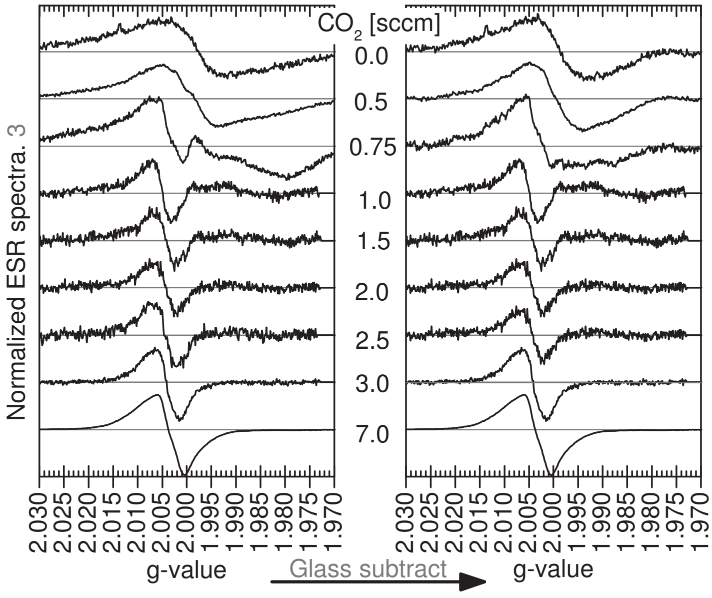

Group 4: 1/ 200/ CO$_2$ = 0.5…2.5 sccm/ 2%/ no seed layer

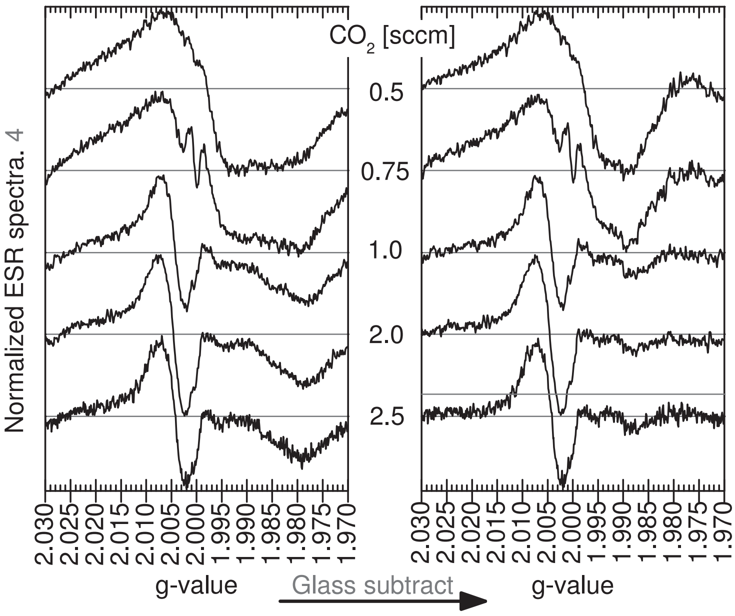

Group 5: 1/ 200/ CO$_2$ = 1.0…3.0 sccm/ 2%/ *i*-type seed

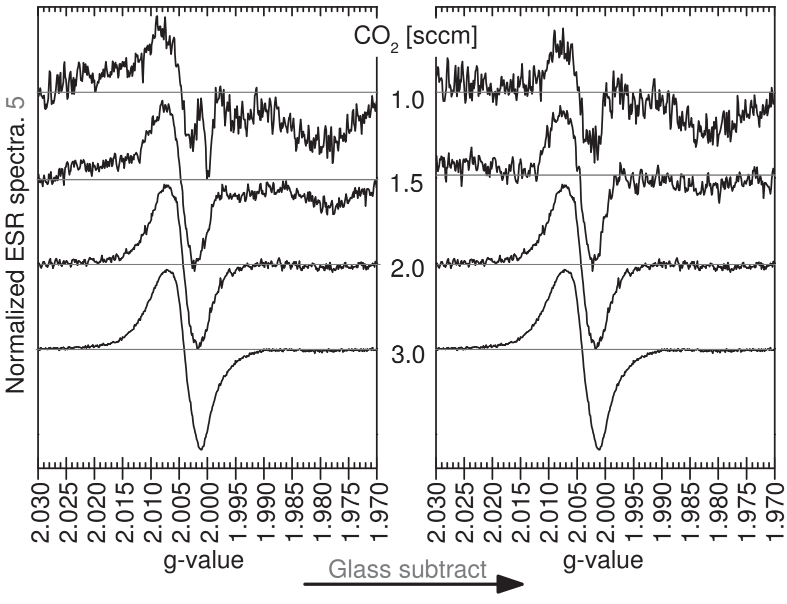

Group 6: 1/ 500/ CO$_2$ = 0…7.0 sccm/ 0% /no seed layer

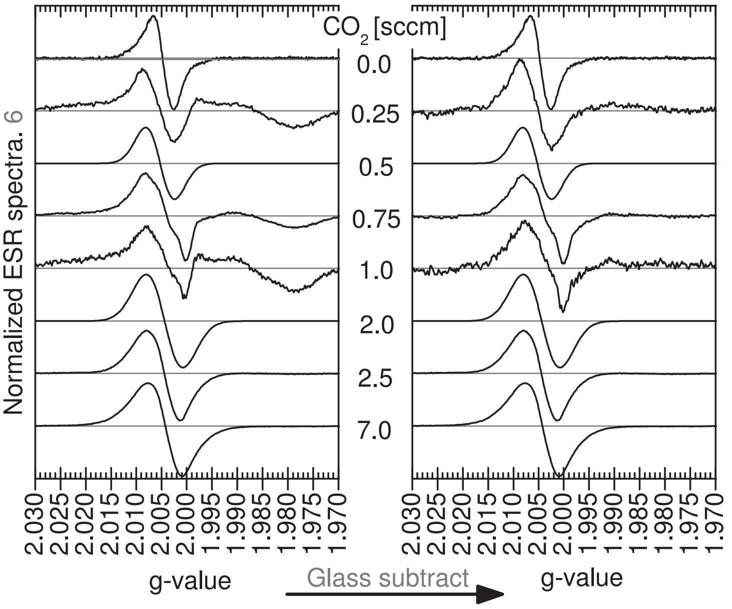

Group 7: 1/ 1000/ CO$_2$ = 1.0…7.0 sccm/ 2%/ no seed layer

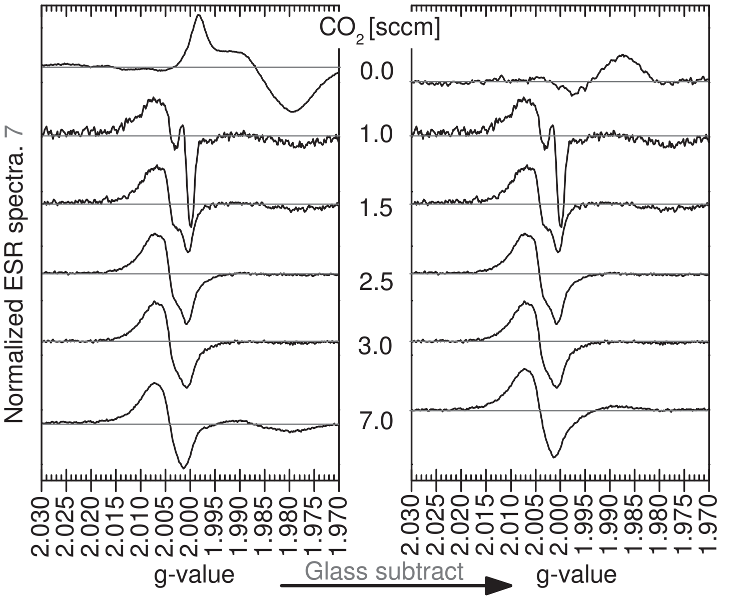

Group 8: 2/ 500/ CO_2 = 1.5…7.0 sccm/ 2%/ no seed layer

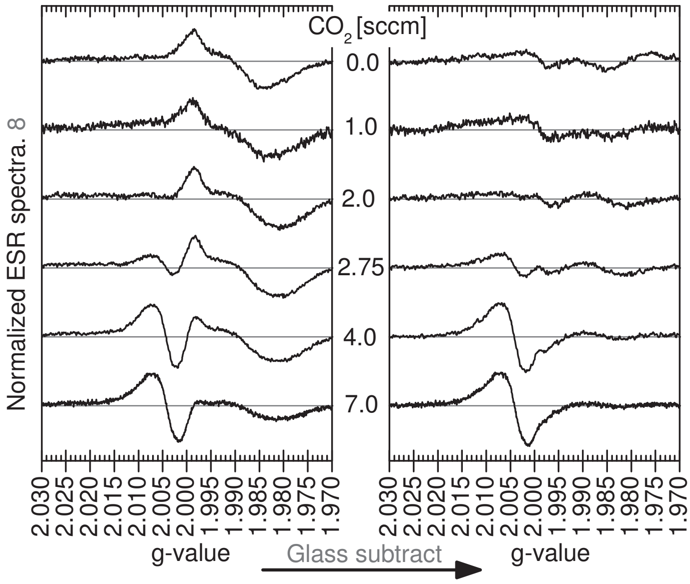

Group 9: 1/ 100/ CO_2 = 0.25…3.0 sccm/ 2%/ no seed layer

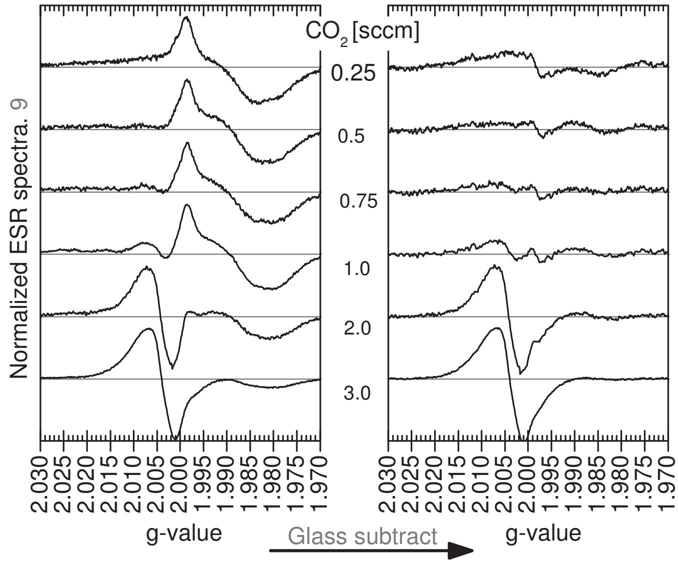

List of Symbols and Abbreviations

acronym	meaning	acronym	meaning
a-	amorphous	MMS	Monomethylsilane
Al	Aluminum	*n*-type	Negatively doped with donors
AFM	Atomic force microscopy	PDS	Photothermal deflection spectroscopy
AM1.5	Solar spectrum at an air mass of 1.5	p	Deposition ressure
c-	Crystalline	PECVD	Plasma enhanced chemical vapor deposition
C_{MMS}	Monomethylsilane concentration	*p*-type	Positively doped with acceptors
CO_2	Carbon dioxide	RBS	Rutherford backscattering spectroscopy
cw-	Continuous wave	SiH_4	Silane
DOS	Density of states	SIMS	Secondary ion mass spectrometry
db	Dangling bond	SC	Silane concentration: Gas ratio of SiH_4 to total source gas (SC = $[SiH_4] / ([SiH_4] + [H_2])$
ESR	Electron spin resonance	sccm	Standard cubic centimeters per minute, a unit of a gas flow
FTIR	Fourier transformed infrared spectroscopy	SOC	Gas ratio of SiH_4 plus CO_2 to the total source gases. (SOC = $[SiH_4] + [CO_2] / ([SiH_4] + [CO_2] + [H_2])$)
FWHM	Full width at the half maximum	T	Temperature,e.g. T_F, T_S and RT are the filament, substrate and room temperatures
i-type	Intrinsic (not doped)	TCO	Transparent conductive oxide
hf	Hyperfine	TEM	Transmission electron Microscopy
H_2	Hydrogen	μc-	microcrystalline
HWCVD	Hot wire chemical vapor deposition		

List of Figures

References

[Abragam1951] A. Abragam and M.H.L. Pryce: *Proc. R. Soc. London, Ser. A* **205** (1951) 135.

[Astakhov2009] O. Astakhov, R. Carius, F. Finger, Y. Petrusenko, V. Borysenko and D. Barankov: *Phys. Rev. B* **79** (2009) 104205.

[Atherton1993] N.M. Atherton: *Principles of Electron Spin Resonance*, Ellis Horwood, PTR Prentice Hall, Chichester (1993).

[Awazu1993] K. Awazu, W. Watanabe and H. Kawazoe: *J. Appl. Phys.* **73** (1993) 8519.

[Bailat2002] J. Bailat, E. Vallat-Sauvain, L. Feitknecht, C. Droz and A. Shah: *J. Non-Cryst. Solids* **299–302** (2002) 1219.

[Barklie2001] R.C. Barklie, M. Collins, M. Richardson and I. Borde: *J. Mater. Sci. – Mater. El* **12** (2001) 231.

[Benninghoven1987] A. Benninghoven, F.G. Rüdenauer and H.W. Werner: *Secondary ion mass spectrometry: basic concepts, instrumental aspects, applications, and trends*, published by John Wiley (1987).

[Biswas1987] R. Biswas and D.R. Hamann: *Phys. Rev. B* **36** (1987) 6434.

[Böer1990] K.W. Böer: *Survey of Semiconductor Physics*, Van Nostrand Reinhold, New York (1990), pp 910

[Brodsky1969] M.H. Brodsky and R.S. Title: *Phys. Rev. Lett.* **23** (1969) 581.

[Brower1983] K.L. Brower: *Appl. Phys. Lett.* **43** (1983) 1111.

[Bühlmann2007] P. Bühlmann, J. Bailat, D. Dominé, A. Billet, F. Meillaud, A. Feltrin and C. Ballif: *Appl. Phys. Lett*. **91** (2007) 143505.

[Buscarino2007] G. Buscarino, PhD thesis: *Experimental investigation on the microscopic structure of intrinsic paramagnetic point defects in amorphous silicon dioxide*. At Ministero dell' Istruzione, dell' Università e della Ricerca (2007).

[Cabarrocas1995] P. Roca i Cabarrocas, N. Layadi, T. Heitz, B.D. Villon and I. Solomon: *Appl. Phys. Lett.* **66** (1995) 3609.

[Cabarrocas1999] P.Roca i Cabarrocas and S. Hamma: *Thin Solid Films* **337** (1999) 23.

[Calcagno2001] L. Calcagno, P. Musumeci, F. Roccaforte, C. Bongiorno and G. Foti: *Appl. Surface Sci.* **184** (2001) 123.

[Caplan1979] P.J. Caplan, E.H. Poindexter, B.E. Deal and R.R. Razouk: *J. Appl. Phys.* **50** (1979) 879.

[Carlson1976] D.E. Carlson and C.R. Wronski: *Appl. Phys. Lett*. **28** (1976) 671.

[Carlos1984] W.E. Carlos: *Nucl. Instrum. Methods Phys. Res. B* (1984) 383.

[Cartier1995] E. Cartier and J.H. Stathis: *Microelectron. Eng*. **28** (1995) 3.

[Chapin1954] D.M. Chapin, C.S. Fuller and G.L. Pearson: *J. Appl. Phys.* **25** (1954) 645.

[Chen2009] T. Chen, Y. Huang, H. Wang, D. Yang, A. Dasgupta, R. Carius and F. Finger: *Thin Solid Films* **517** (2009) 3513.

[Chen2010(1)] T. Chen, D. Yang, R. Carius and F. Finger: *Jpn. J. Appl. Phys*. **49** (2010) 041303.

[Chen2010(2)] T. Chen, A. Schmalen, J. Wolff, D. Yang, R. Carius and F. Finger: *Physica Status Solidi (c)* (2010) 1.

[Chen2011] T. Chen, Y. Huang, D. Yang, R. Carius and F. Finger: *Thin Solid Films* **519** (2011) 4523.

[Chen2012] T. Chen, Y. Huang, A. Dasgupta, M. Luysberg, L. Houben, D. Yang, R. Carius and F. Finger: *Sol. Energ. Mat. Sol*. **98** (2012) 370.

[Choyke2004] W.J. Choyke, H. Matsunami and G. Pensl: *Silicon Carbide: Recent Major Advances*, Springer-Verlag Berlin and Heidelberg (2004).

[Combrisson1954] J. Combrisson and J. Uebersfeld: *Compte. Rend.* **238** (1954) 572.

[Cousins2010] P.J. Cousins, D.D. Smith, H.C. Luan, J. Manning, T.D. Dennis, A. Waldhauer, K.E. Wilson, G. Harley and G.P. Mulligan: *Improved performance at lower cost*. 35th IEEE PVSC (2010).

[Cuony2010] P. Cuony, M. Marending, D.T.L. Alexander, M. Boccard, G. Bugnon, M. Despeisse and C. Ballif: *Appl. Phys. Lett*. **97** (2010) 213502.

[Dalibor1998] T. Dalibor, G. Pensl, T. Yamamoto, T. Kimoto, H. Matsunami, S.G. Sridhara, D.G. Nizhner, R.P. Devaty and W.J. Choyke: *Mater. Sci. Forum.* **264 – 268** (1998) 553.

[Dasgupta2008(1)] A. Dasgupta, Y. Huang, L. Houben, S. Klein, F. Finger, R. Carius and M. Luysberg: *Thin Solid Films* **516** (2008) 618.

[Dasgupta2008(2)] A. Dasgupta, Y. Huang, L. Houben, S. Klein, F. Finger, R. Carius and M. Luysberg: *Thin Solid Films* **516** (2008) 622.

[Dersch1981] H. Dersch, J. Stuke and J. Beichler: *Phys. Stat. Sol. (b)* **106** (1981) 265.

[Dirani2000] E.A.T. Dirani, A.M. Andrade, L.K. Noda, F.J. Fonseca and P.S. Santos: *J. Non-Cryst. Solids* **273** (2000) 307.

[Dkaki2001] M. Dkaki, L. Calcagno, A.M. Makthari and V. Raineri: *Mater. Sci. Semicond. Proc.* **4** (2001) 201.

[Dylla2003] T. Dylla, F. Finger and R. Carius: *Mater. Res. Soc. Symp. Proc.* **762** (2003) 81.

[Dylla2004] T. Dylla. PhD thesis: *Electron Spin Resonance and Transient Photocurrent Measurements on Microcrystalline Silicon*, Forschunszentrum Jülich GmbH Institue für Photovoltaik (2004).

[Economou1987] E.N. Economou and N. Bacalis: *J. Non-Cryst. Solids* **97 – 98** (1987) 101.

[Efros1972] A.L. Efros, B.I. Shklovskii and I.Y. Yanchev: *Physica Status Solidi (b)* **50** (1972) 45.

[Fehr2011] M. Fehr, PhD thesis: *Paramagnetic Defects in hygrogenated amorphous silicon: an advanced Electron Paramagnetic Resonance study*, Institut für Experimentalphysik der Freien Universität Berlin (2011).

[Finger1994] F. Finger, C. Malten, P. Hapke, R. Carius, R. Fluckiger and H. Wagner: *Philos. Mag. Lett.* **70** (1994) 247.

[Finger1998] F. Finger, J. Müller, C. Malten and H. Wagner: *Philos. Mag. B* **77** (1998) 805.

[Finger2003] F. Finger, R. Carius, T. Dylla, S. Klein, S. Okur and M. Günes: *IEEE Proc. – Circuits Devices Syst.* **150** (2003) 300.

[Finger2009] F. Finger, O. Astakhov, T. Bronger, R. Carius, T. Chen, A. Dasgupta, A. Gordijn, L. Houben, Y. Huang, S. Klein, M. Luysberg, H. Wang and L. Xiao: *Thin Solid Films* **517** (2009) 3507.

[Fuhs2000] W. Fuhs, P. Kanschat and K. Lips: *J. Vac. Sci. Technol. B* **18** (2000) 1792.

[Götz1994] W. Götz, A. Schöner, W. Suttrop, G. Pensl, W.J. Choyke, R.A. Stein and S. Leibenzender: *Mater. Sci. Forum.* **143-147** (1994) 69.

[Green2011] M.A. Green, K. Emery, Y. Hishikawa and W. Warta: *Prog. Photovolt.: Res. Appl.* **19** (2011) 84.

[Griscom1976] D.L. Griscom, E.J. Friebele, K.J. Long and J.W. Fleming: *J. Appl. Phys*. **43** (1976) 960.

[Griscom1983] D.L. Griscom, G.H. Sigel. Jr. and R.J. Ginther: *J. Appl. Phys*. **54** (1983) 3743.

[Grundler2010] T. Grundler, A. Lambertz and F. Finger: *Physica Status Solidi (c)* **7** (2010) 1085.

[Hack1985] M. Hack and M. Schur: *J. Appl. Phys*. **58** (1985) 997.

[Hasegawa1983] S. Hasegawa, S. Narikawa and Y. Kurata: *Philos. Mag. B* **48** (1983) 431.

[Henry2001] A. Henry, B. Magnusson, M.K. Linnarsson, A. Ellison, M. Syväjärvi, R. Yakimova and E. Janzén: *Mater. Sci. Forum* **353 – 356** (2001) 373.

[Holzenkampfer1979] E. Holzenkampfer, F.W. Richter, J. Stuke and U. Voget-Grote: *J. Non-Cryst. Solids* **32** (1979) 327.

[Hosono1994] H. Hosono, H. Kawazoe, K. Oyoshi and S. Tanaka: *J. Non-Cryst. Solids* **179** (1994) 39.

[Houben1998] L. Houben, M. Luysberg, P. Hapke, R. Carius, F. Finger and H. Wagner: *Philos. Mag. A* **77** (1998) 1447.

[] *J. Non-Cryst. Solids*. **354** (2008) 2430[Ichikawa1996] Y. Ichikawa, K. Tabuchi, A. Takano, S. Fujikake, T. Yoshida and H. Sakai: *J. Non-Cryst. Solids.* **198 – 200** (1996) 1081.

[Itoh1990] H. Itoh, M. Yoshikawa, I. Nashiyama, S. Misawa, H. Okumura and S. Yoshida: *IEEE Trans. Nucl. Sci.* **37** (1990) 1732.

[Jackson1981] W.B. Jackson, N.M. Amer, A.C. Boccara and D. Fournier: *Appl. Optics* **20** (1981) 1333.

[Jadkar2000] S.R. Jadkar, J.V.Sali, M.G. Takwale, D.V. Musale and S.T. Kshirsagar: Extended Abstract of 1st International Conference on HWCVD Process (2000) Japan, pp 177.

[Jana2000] T. Jana and S. Ray: *Thin Solid Films* **376** (2000) 241.

[Janotta2004] A. Janotta, R. Janssen, M. Schmidt, T. Graf and M. Stutzmann: *Phys. Rev. B* **69** (2004) 115206.

[Janzén2003] E. Janzén, I.G. Ivanov, N.T. Son, B. Magnusson, Z. Zolani, A. Henry, J.P. Bergman, L. Storasta and F. Carlsson: *Physica B* **340 – 342** (2003) 15.

[Jivănescu2010] M.A. Jivănescu, PhD thesis: *Intrinsic Point Defects in a-SiO$_2$ with Embedded Si Nanoparticles Probed by ESR*. Katholieke Universiteit Leuven (Belgium) (2010).

[Joannopoulos1984] J.D. Joannopoulos and G. Lucovsky (Ed.): The Physics of Hydrogenated Amorphous Silicon I, II, Springer – Verlag, Berlin (1984).

[Kanschat2000] P. Kanschat, H. Mell, K. Lips and W. Fuhs: *Mater. Res. Soc. Proc. A* **27.3** (2000) 609.

[Karna1999] S.P. Karna, H.A. Kurtz, W.M. Shedd, R.D. Pugh and B.K. Singaraju: *IEEE Trans. Nucl. Sci.* **46** (1999) 1544.

[Kerdiles2000] S. Kerdiles, A. Berthelot, F. Gourbilleau and R. Rizk: *Appl. Phys. Lett.* **76** (2000) 2373.

[Kerdiles2002] S. Kerdiles and R. Rizk: *Philosophical Magazine A* **82** (2002) 601.

[Keunen2011] K.Keunen, A. Stesmans and V.V. Afanas'ev: *Appl. Phys. Lett.* **98** (2011) 213503.

[Klein2003] S. Klein, PhD thesis: *Microcrystalline Silicon Prepared by Hot Wire CVD – Preparation and Characterisation of Material and Solar Cells*, Technische Universität München (2003).

[Klein2005] S. Klein, R. Carius, L Houben and F. Finger: *Mater. Res. Soc. Symp. Proc*. **862** (2005) 145.

[Klein2006] S. Klein, L. Houben, R. Carius, F. Finger and W. Fischer*: J. Non-Cryst. Solids*. **352** (2006) 1376.

[Klein2008] S. Klein, R. Carius, F. Finger and L Houben: *Thin Solid Films*. **516** (2008) 630.

[Kluth2001] O. Kluth, PhD thesis: *Texturierte Zinkoxidschichten für Silizium – Dünnschichtsolarzellen*, Rheinisch-Westfälische Technische Hochschule Aachen (2001).

[Knights1979] J.C. Knights: *Jpn. J. Appl. Phys.* **18** (1979) 101.

[Köhler2011] F. Köhler, T. Chen, M. Nuys, A. Heidt, M. Luysberg, F. Finger and R. Carius: *J. Non-Cryst. Solids (2012)*, doi: 10.1016/j.jnoncrysol.2011.12.057

[Kondo1996] M. Kondo, Y. Toyoshima, A. Matsuda and K. Ikuta: *J. Appl. Phys.* **80** (1996) 6061.

[Lambertz2007] A. Lambertz, A. Dasgupta, W. Reetz, A. Gordijn, R. Carius and F. Finger, in: *Proceedings of 22nd EUPVSEC* (2007) 1839.

[Lambertz2011] A. Lambertz, T. Grundler and F. Finger: *J. Appl. Phys.* **109** (2011) 113109.

[Lambertz2012] A. Lambertz, F. Finger, B. Holländer, J.K. Rath and R.E.I. Schropp: *J. Non-Cryst. Solids (2012)*, doi: 10.1016/j.jnoncrysol.2011.12.047.

[Larkins2011] Peter Larkin: *Infrared and Raman Spectroscopy – Principles and Spectral Interpretation*. Copyright © 2011 Elsevier Inc. ISBN-10: 0123869846, ISBN-13: 978-0123869845.

[Lenahan1982] P.M. Lenahan and P.V. Dressendorfer: *Appl. Phys. Lett*. **41** (1982) 542.

[Lenahan1998] P.M. Lenahan and J.F. Conley, Jr.: *J. Vac. Sci. Technol. B* **16**(1998) 2134.

[Lips2002] K. Lips, P. Kanschat, S. Brehme and W. Fuhs: *J. Non-Cryst. Solids* **299 – 302** (2002) 350.

[Lips2003] K. Lips, R. Kanschat and W. Fuhs: *Solar Energ. Mater.& Solar Cell.* **78** (2003) 513.

[Maier1997] D.C. Maier: *Bruker Reports* **114** (1997) 13.

[Makimura2002] T. Makimura, Y. Yamamoto, S. Mitani, T. Mizuta, C.Q. Li, D. Takeuchi and K. Murakami: *Appl. Surf. Sci.* **197 – 198** (2002) 670.

[Malten1999] C. Malten, F. Finger, J. Muller and S. Yamasaki: *Mater. Res. Soc. Symp. Proc.* **507** (1999) 757.

[Matsumoto2008] Y. Matsumoto, V. Sanchez R. and A. Avila G.: *Thin Solid Films* **516** (2008) 593.

[Mcinnes1979] J.A. Mcinnes and P.N. Butcher: *Philos. Mag. B* **39** (1979) 1.

[Miyajima2006] S. Miyajima, A. Yamada and M. Konagai: *Thin Solid Films* **501** (2006) 186.

[Miyajima2007] S. Miyajima, A. Yamada and M. Konagai: *Jpn. J. Appl. Phys.* **46** (2007) 1415.

[Mizuguchi1998] M. Mizuguchi, H. Hosono and H. Kawazoe: *Mater. Sci. Eng. B* **54** (1998) 38.

[Mizuochi2005] N. Mizuochi, S. Yamasaki, H. Takizawa, N. Morishita, T. Ohshima, H. Itoh, T. Umeda and J. Isoya: *Phys. Rev. B* **72** (2005) 235208.

[Morris1990] J. Morris, R.R. Arya, J.G. O'Dowd and S. Wiedemann: *J. Appl. Phys.* **67** (1990) 1079.

[Mott1968] N.F. Mott: *J. Non – Cryst. Solids.* **1** (1968) 1.

[Mott1979] N.F. Mott and E.A. Davis. *Electronic Processes in Non-crystalline Materials* (2^{nd} edition), Oxford University Press (1979).

[] [Müller1998] J. Müller, F. Finger, C. Malten and H. Wagner: *J. Non-Cryst. Solids* **227 – 230** (1998) 1026.

[Müller1999] J. Müller, F. Finger, R. Carius and H. Wagner: *Phys. Rev. B* **60** (1999) 11666.

[Murphy1966] J. Murphy: *Phys. Rev.* **145** (1966) 241.

[Nakashima1997] S. Nakashima and H. Harima: *Physica Status Solidi (a)* **162** (1997) 39.

[Nelson1960] C.M. Nelson and R.A. Weeks: *J. Am. Ceram. Soc.* **43** (1960) 396.

[Nelson2003] J. Nelson: *The Physics of Solar Cells*, Imperial College Press (2003).

[Nishi1971] Y. Nishi: *Jpn. J. Appl. Phys.* **10** (1971) 52.

[Owen2011] J.I. Owen, PhD thesis: *Growth, Etching, and Stability of Sputtered ZnO:Al for Thin-Film Silicon Solar Cells*, Rheinisch-Westfälische Technische Hochschule Aachen (2011).

[Palmetshofer2011] L. Palmetshofer: *Rutherford Backscattering Spectroscopy (RBS) in Surface and Thin Film Analysis: A Compendium of Principles, Instrumentation, and Applications*, published by Wiley-VCH Verlag GmbH & Co. KGaA, Weinheim, Germany (2011).

[Pauli1927] W. Pauli: *Über Gasentartung und Paramagnetismus*, Zeitschrift für Physik **41** (1927) 81.

[Pawlak1999] B.J. Pawlak, T. Gregorkiewicz and C.A.J. Ammerlaan: *Physica B* **273 – 274** (1999) 938.

[Poole1971] C.P. Poole and H.A. Farach: *Relaxation in magnetic Resonance*, Academic Press, New York, London (1971).

[Poortmans2006] J. Poortmans and V. Arkhipov: *Thin Film Solar Cells*: *Fabrication, Characterization and Applications*, Wiley Series in Materials for Electronic & Optoelectronic Applications (2006).

[Quaresima1987] C. Quaresima, P. Perfetti, E. Paparazzo, M. Capozi, C. Vaccarezza, B. Russo and C. Coluzza: *J. Non-Cryst. Solids* **97 – 98** (1987) 979.

[Rajagopalan2003] T. Rajagopalan, X. Wang, B. Lahlouh, C. Ramkumar, P. Dutta and S. Gangopadhyay: *J. Appl. Phys*. **94** (2003) 5252.

[Rech1997] B. Rech, C. Beneking, S. Wieder and H. Wagner: *Proceeding of 14th EUPVSEC* (1997) 574.

[Reynolds2003] S. Reynolds, V. Smirnov, C. Main, R. Carius and F. Finger: *Mater. Res. Soc. Proc.* **762** (2003) 327.

[Sarker2002] A. Sarker, C. Banerjee, and A.K. Barua: *J. Phys. D: Appl. Phys.* **35** (2002) 1205.

[Schneider1993] J. Schneider and K. Maier: *Physica B* **185** (1993) 199.

[Schropp2008] R.E.I. Schropp, J.W.A. Schüttauf, C.H.M. van der Werf and W. Arnoldbik: *Proceeding of the 23rd EUPVSEC* (2008) pp 2109–2112.

[Shendrik1985] A.V. Shendrik and D.M. Yudin: *Physica Status Solidi (b)* **85** (1985) 343.

[Shockley1961] W. Shockley and H.J. Queisser: *J. Appl. Phys*. **32** (1961) 510.

[Sichanugrist1993] P. Sichanugrist, T. Yoshida, Y. Ichikawa and H. Sakai: *J. Non-Cryst. Solids* **164 – 166** (1993) 1081.

[Silva2006] A.F. da Silva, J. Pernot, S. Contreras, B.E. Sernelius, C. Persson and J. Camassel: *Phys. Rev. B* **74** (2006) 245201.

[Skuja2008] L. Skuja, K. Kajihara, M. Hirano and H. Hosono: *Nucl. Instrum. Meth. B* **266** (2008) 2971.

[Smirnov2004] V. Smirnov, S. Reynolds, C. Main, F Finger and R. Carius: *J. Non-Cryst. Solids.* **338** (2004) 421.

[Smirnov2006] V. Smirnov, S. Reynolds, F. Finger, R. Carius and C. Main: *J. Non-Cryst. Solids.* **352** (2006) 1075.

[Smirnov2010] V. Smirnov, W. Böttler, A. Lambertz, H. Wang, R. Carius and F. Finger: *Physica Status Solidi (c)* **7** (2010) 1053.

[Smith1971] J.E. Smith. Jr., M.H. Brodsky, B.L. Crowder, M.I. Nathan and A. Pinczuk: *Phys. Rev. Lett.* **26** (1971) 642.

[Son2010] N.T. Son, J. Isoya, T. Umeda, I.G. Ivanov, A. Henry, T. Ohshima and E. Janzén: *Appl. Magn. Reson.* **39** (2010) 49.

[Sörman2000] E. Sörman, N.T. Son, W.M. Chen, O. Kordina, C. Hallin and E. Janzén: *Phys. Rev. B* **61** (2000) 2613.

[Soukoulis1985] C.M. Soukoulis, M.H. Cohen, E.N. Economou and A.D. Zdetsis: *J. Non-Cryst. Solids* **77 – 78** (1985) 47.

[Spitzer1959] W.G. Spitzer, D.A. Kleinman and C.J. Frosch: *Phys. Rev. B* **113** (1959) 133.

[Sritharathikhun2009] J. Sritharathikhun, F. Jiang, S. Miyajima, A. Yamada and M. Konagai: *Jpn. J. Appl. Phys.* **48** (2009) 101603.

[Staebler1977] D.L. Staebler and C.R. Wronski: *Appl. Phys. Lett.* **31** (1977) 292.

[Stathis1991] J.H. Stathis and L. Dori: *Appl. Phys. Lett.* **58** (1991) 1641.

[Stesmans1990] A. Stesmans and G. van Gorp: *Phys. Rev. B* **42** (1990) 3765.

[Stesmans1991] A. Stesmans and G.van Gorp: *Physica B* **170** (1991) 507.

[Stesmans1996] A. Stesmans and V.V. Afanas'ev: *Appl. Phys. Lett.* **69** (1996) 2056.

[Stesmans1998] A. Stesmans, B. Nouwen and V. V. Afanas'ev: *Phys. Rev. B* **58** (1998) 15801.

[Stesmans2002] A. Stesmans, B. Nouwen and V.V. Afanas'ev: *Phys. Rev. B* **66** (2002) 045307.

[Stesmans2008] A. Stesmans, M. Jivanescu, S. Godefroo and M. Zacharias: *Appl. Phys. Lett.* **93** (2008) 023123.

[Stirling2002] A. Stirling and A. Pasquarello: *Phys. Rev. B* **66** (2002) 245201.

[Street1980] R.A. Street and D.K. Biegelsen: *Solid State Commun.* **33** (1980) 1159.

[Street1981] R.A. Street, D.K. Biegelsen and J.C. Knights: *Phys. Rev. B* **24** (1981) 969.

[Street1991] R.A. Street: *Hydrogenated Amorphous Silicon*. Cambridge University Press (1991).

[Stutzmann1983] M. Stutzmann and J. Stuke: *Solid State Commun*. **47** (1983) 635.

[Stutzmann1985] M. Stutzmann, W.B. Jackson and C.C. Tsai: *Phys. Rev. B* **32** (1985) 23.

[Stutzmann1987] M. Stutzmann, D.K. Biegelsen and R.A. Street: *Phys. Rev. B* **35** (1987) 5666.

[Stutzmann1988] M. Stutzmann and D.K. Biegelsen: The microscopic structure of defects in a-Si:H and related materials, in:H. Fritzsche (ed.), *Amorphous Silicon and Related Materials*, pp 557 – 594, World Scinetific, Singapore (1988).

[Stutzmann1989] M. Stutzmann and D.K. Biegelsen: *Phys. Rev. B* **40** (1989) 9834.

[Stutzmann1991] M. Stutzmann and J. Stuke: *Philos. Mag. B* **63** (1991) 151.

[Takahashi1987] T. Takahashi, B.B. Triplett, K. Yokogawa and T. Sugano: *Appl. Phys. Lett.* **26** (1987) 1339.

[Tanielian1980] M. Tanielian, M. Chatani, H. Fritzsche, V. Smid and P.D. Persans: *J. Non-Cryst. Solids* **35 – 36** (1980) 575.

[Tanielian1982] M. Tanielian: *Philos. Mag. B* **45** (1982) 435.

[Thomas1978] P.A. Thomas, M.H. Brodsky, D. Kaplan and D. Lepine: *Phys. Rev. B* **18** (1978) 3059.

[Tsai1988] C.C. Tsai, R. Thompson, C. Doland, F.A. Ponce, G.B. Anderson and B. Wacker: *Mater. Res. Soc. Symp. Proc.* **118** (1988) 49.

[Tzolov1997] M. Tzolov, F. Finger, R. Carius and P. Hapke: *J. Appl. Phys.* **81** (1997) 7376.

[Ueda1999] K. Ueda, T. Ushirosako and M. Yoshimura: *Thin Solid Films* **343 – 344** (1999) 612.

[Vepřek1983] S. Vepřek, Z. Iqbal, R.O. Kühne, P. Capezzuto, F.-A. Sarott and J.K. Gimzewski: *J. Phys. C: Solid State Phys.* **16** (1983) 6241.

[Vetterl2000] O. Vetterl, F. Finger, R. Carius, P. Hapke, L. Houben, O. Kluth, A. Lambertz, A. Mück, B. Rech and H. Wagner: *Sol. Energy Mater. Sol. Cells* **62** (2000) 97.

[Vetterl2001] O. Vetterl, PhD thesis: *On the Physics of Microcrystalline silicon Thin Film Soar Cells – From the Material to Devices with High Conversion Efficiencies.* In Berichte des Forschungszentrum Jülich 3897 (2001).

[Weber2005] Ralph T. Weber: *Bruker Elexsys E 580 User's manual*, Bruker BioSpin Corporation Billerica, MA USA (2005).

[Weeks1956] R.A. Weeks: *J. Appl. Phys*. **27**(1956) 1376.

[Weeks2008] R.A. Weeks, R.H. Magruder III and A. Stesmans: *J. Non-Cryst. Solids* **354** (2008) 208.

[Weil2007] John A. Weil and James R. Bolton: *Electron paramagnetic resonance: elecmentary theory and preactical applications* (2nd edtion). Published by John Wiley & Sons, Inc., Hoboken, New Jersey, USA (2007) pp 316.

[Wieringen1958] J.S. van Wieringen, in: *Semiconductors and Phosphors*, edited by M. Schön and H. Welker (Interscience Publishers, Inc., New York, 1958) pp 367.

[Windle1964] J.J. Windle and A.K. Wiersema: *J. Appl. Polym. Sci*. **8** (1964) 1531.

[Wördenweber2011] J. Wördenweber, PhD thesis: *Impact of contamination of hydrogenated amorphous silicon thin films & solar cells.* In Berichte des Forschungszentrum Jülich, Band/ Volume **103** (2011).

[Xiao2010(1)] L. Xiao, O. Astakhov, R. Carius, T. Chen, H. Wang, M. Stutzmann and F. Finger: *Physica Status Solidi (c)* **7** (2010) 778.

[Xiao2010(2)] L. Xiao, O. Astakhov, R. Carius, A. Lambertz, T. Grundler and F. Finger: *Physica Status Solidi (c)* **7** (2010) 941.

[Yam1986] Y. Bar-Yam and J.D. Joannopoulos: *Phys. Rev. Lett.* **56** (1986) 2203.

[Yilmaz2010] G. Yilmaz, E. Turan, M. Günes, V. Smirnov, F. Finger and R. Brüggemann: *Physica Status Solidi (c)* **7** (2010) 700.

[Zavoisky1945] E. Zavoisky: *J. Phys, U. S. S. R.* **9** (1945) 211.

List of Publications

1. Lihong Xiao, Oleksandr Astakhov, Friedhelm Finger and Martin Stutzmann: *Determination of the defect density in thin film amorphous and microcrystalline silicon from ESR measurements: The influence of the sample preparation procedure*. Journal of Non-Crystalline Solids (Tentatively by June of 2012), doi: 10.1016/j.jnoncrysol.2012.01.039.
2. Lihong Xiao, Oleksandr Astakhov, Tao Chen, Martin Stutzmann and Friedhelm Finger: *Aluminum Doped Silicon Carbide Thin Films Prepared by Hot-Wire CVD: Investigation of Defects with Electron Spin Resonance*. Thin Solid Films **519** (2011) 4519.
3. Lihong Xiao, Oleksandr Astakhov and Friedhelm Finger: *Si powder samples for Electron Spin Resonance investigation: Roles of substrate and preparation procedure*. Japanese Journal of Applied Physics **50** (2011) 071301.
4. Lihong Xiao, Oleksandr Astakhov, Reinhard Carius, Tao Chen, Haiyan Wang, Martin Stutzmann and Friedhelm Finger: *Paramagnetic states in μc-SiC:H thin films prepared by Hot-Wire CVD at low temperatures*. Physica Status Solidi (c) **7** (2010) 778.
5. Lihong Xiao, Oleksandr Astakhov, Reinhard Carius, Andreas Lambertz, Thomas Grundler and Friedhelm Finger: *Defects and structure of μc-SiO_x:H deposited by PECVD*. Physica Status Solidi (c) **7** (2010) 941.
6. Friedhelm Finger, Oleksandr Astakhov, Torsten Bronger, Reinhard Carius, Tao Chen, Arup Dasgupta, Aad Gordijn, Lothar Houben, Yuelong Huang, Stefan Klein, Martina Luysberg, Haiyan Wang and Lihong Xiao: *Microcrystalline silicon carbide alloys prepared with HWCVD as highly transparent and conductive window layer for thin film solar cells*. Thin Solid Films **517** (2009) 3507.

Danksagung

Ich möchte mich zunächst bei allen bedanken, die mich bei der Durchführung meiner Doktorarbeit unterstützt haben. Ich konnte bei der Anfertigung meiner Doktorarbeit am IEK-5 des Forschungszentrums Jülich auf die Hilfe und Unterstützung vieler Kollegen und Freunde zurückgreifen.

Herrn Prof. Dr. Martin Stutzmann, meinem Doktorvater, danke ich für seine gute Betreuung und Unterstützung, sein unerschöpfliches Wissen über Halbleiterphysik und seine Geduld bei der Beantwortung meiner Fragen.

Herrn Prof. Dr. Uwe Rau danke ich für die Möglichkeit, meine Doktorarbeit an seinem Institut durchführen zu können, für sein Interesse an der Arbeit und die Übernahme des Zweitgutachtens. Des Weiteren danke ich ihm für die ebenfalls gute Betreuung meiner Arbeit, für die wissenschaftliche wie persönliche Unterstützung, sowie für das in mich gesetzte Vertrauen.

Herrn Dr. Friedhelm Finger, meinem Betreuer, gilt mein Dank für die Betreuung während der gesamten Zeit meiner Doktorarbeit, sowie für das in mich gesetzte Vertrauen. Seine zahlreichen Anregungen und seine unkomplizierte Art der Betreuung ermöglichten es mir, viele meiner Ideen in die Tat umzusetzen. Er zeigte mir, was es bedeutet, ein guter Wissenschaftler zu sein.

Danken möchte ich des Weiteren Herrn Dr. Oleksandr Astakhov, meinem zweiten Betreuer, für die Einführung insbesondere in das komplexe Themengebiet der Elektronenspinresonanz sowie die kontinuierliche Betreuung und Möglichkeiten zur Diskussion während der gesamten Zeit meiner Arbeit. Ich habe sehr von seinem großen Wissen im Bereich der ESR profitiert.

Mein Dank gilt zudem Herrn Prof. Dr. Reinhard Carius für die fruchtbaren Diskussionen insbesondere zur Ramananalyse von Silizium sowie von Silziumcarbid und Siliziumoxid. In

diesem Zusammenhang danken möchte ich auch den Herren Florian Köhler und Markus Hülsbeck, ohne die eine Ramananalyse an meinen Proben ebenfalls nicht möglich gewesen wäre.

Bei Herrn Dr. Wolfhard Beyer, Herrn Dr. Arjan Flikweert, Herrn Dr. Stefan Haas, Herrn Dr. Etienne Moulin, Herrn Dr. Jorj Owen, Herrn Dr. Bart Pieters, und Herrn Dr. Vladimir Smirnov möchte ich mich für viele hilfreiche, informative Diskussionen sowie das Einbringen ihrer wissenschaftlichen Erfahrung bedanken. Zudem möchte ich mich bei Ihnen für die Korrektur vor allem sprachlicher Fehler in meiner Arbeit bedanken.

Zudem gilt mein Dank Herrn Andreas Lambertz. Er führte mich in die Tiefen der Dünnschichtdepositionstechnik sowie die Eigenheiten der von mir genutzten PECVD Anlage ein. Herrn Dr. Tao Chen gilt mein Dank für die Siliziumcarbiddepositionen an der HWCVD Anlage, sowie für viele hilfreiche und informative Diskussionen.

Herrn Josef Klomfaß gilt mein Dank für die Wartung zahlreicher von mir genutzter Charakterisierungssysteme und für das stets offene Ohr bei maschinenspezifischen Fragestellungen. Herrn Gunnar Schöpe danke ich für die Durchführung der Laserstrukturierung. Für die Substratvorbereitung sowie für die Herstellung vieler Proben bedanke ich mich bei Frau Rebbeca van Aubel, Frau Sandra Moll, und Frau Janine Worbs. Herrn Uwe Zastrow gilt mein Dank für die Durchführung und Bewertung von SIMS-Analysen.

Für die äußerst erfolgreiche Zusammenarbeit im EPR-Solar Projekt bedanke ich mich bei Herrn Prof. Dr. Martin Brandt und Herrn Konrad Klein von der Technischen Universität München, Herrn Dr. Klaus Lips, Herrn Dr. Matthias Fehr und Herrn Benjamin George vom Helmholtz-Zentrum Berlin, Herrn Prof. Dr. Robert Bittl, Herrn Dr. Christian Teutloff und Herrn Christoph Meier von der Freien Universität Berlin.

Für die Hilfe bei organisatorischen Angelegenheiten möchte ich mich bei Frau Inge Klaus, Frau Andrea Mülheims, Astrid Nogga, Frau Susanne Griesen, Frau Natalie Krapp und Frau Eugenia Papst bedanken. Allen Mitarbeitern des Institut für Energie- und Klimaforschung (IEK-5) – Photovoltaik danke ich für die nette Arbeitatmosphäre, für ihre stetige Hilfsbereitschaft, die lustigen Lernabende und das Teilen gemeinsamer Glücksgefühle.

Mein Dank geht zudem an das Chinese Scholarship Council (CSC) für die finanzielle Unterstützung von September 2007 bis September 2010.

Last but not least danke ich meinen Eltern, meinen geliebten Brüdern und meinem besten Freund P.P. Yang für ihre Unterstützung und Motivation.

Curriculum vitae

Name	Lihong XIAO
Date and place of birth	23rd July, 1982 @ Wuhan, Hubei province, P. R. China
October 2008 to June 2012	**PhD student** at Walter Schottky Institut – Zentralinstitut für physikalische Grundlagen der Halbleiterelektronik der Technische Universität München and at Institut für Energie- und Klimaforschung (IEK-5) – Photovoltaik, Forschungszentrum Jülich GmbH, Deutschland. **Thesis**: Electron Spin Resonance investigation of semiconductor materials for application in thin-film silicon solar cells
October 2007 to September 2008	**Guest scientist** at Institut für Energie- und Klimaforschung (IEK-5) – Photovoltaik, Forschungszentrum Jülich GmbH, Deutschland.
September 2004 to March 2007	**Master** at condensed matter physics at Pohl Institute of Solid State Physics of Tongji University, Shanghai, P. R. China. **Thesis**: Preparation and doping mechanism research into $GdTaO_4:Eu^{3+}$ photoluminescent and transparent thin films
September 2000 to July 2004	Studies for a **Bachelor** degree at Electronic Information Engineering Department of at Hubei University, Wuhan, P. R. China. Major: Electronic Science and Technology **Thesis**: Preparation and characterization of $BaTiO_3$ ferroelectric ceramic

Band / Volume 132
Rauchgasseitige Korrosion Nickelbasislegierungen für zukünftige 700°C-Dampfkraftwerke
F. Lüttschwager (2012), 145 pp.
ISBN: 978-3-89336-773-3

Band / Volume 133
In-Situ Raman Spectroscopy: A Method to Study and Control the Growth of Microcrystalline Silicon for Thin-Film Solar Cells
S. Muthmann (2012), x, 134 pp.
ISBN: 978-3-89336-774-0

Band / Volume 134
Remote sensing of sun-induced fluorescence for improved modeling of gross primary productivity in a heterogeneous agricultural area
A. Schickling (2012), xvi, 135 pp.
ISBN: 978-3-89336-775-7

Band / Volume 135
Untersuchung der Ladungsträgerkonzentration und -beweglichkeit in mikrokristallinen Siliziumlegierungen mit Hall-Effekt undThermokraft
C. Sellmer (2012), 159 pp.
ISBN: 978-3-89336-778-8

Band / Volume 136
Development of thin film inorganic membranes for oxygen separation
H. J. Moon (2012), XII, 118 pp.
ISBN: 978-3-89336-781-8

Band / Volume 137
Influence of Material and Testing Parameters on the Lifetime of TBC Systems with MCrAlY and NiPtAl Bondcoats
P. Song (2012), V, 126 pp.
ISBN: 978-3-89336-783-2

Band / Volume 138
Strömungsmechanische Modellierung eines Brenngaserzeugungssystems
F. Scharf (2012), vi, 223 pp.
ISBN: 978-3-89336-784-9

Band / Volume 139
Clouds and aerosol in infrared radiative transfer calculations for the analysis of satellite observations
S. Grießbach (2012), viii, 169 pp.
ISBN: 978-3-89336-785-6

Band / Volume 140
Untersuchung zum Thin Film Low Pressure Plasma Spraying (LPPS-TF) Prozess
A. Hospach (2012), 165 pp.
ISBN: 978-3-89336-787-0

Band / Volume 141
Development of thermal spray processes with liquid feedstocks
A. Guignard (2012), 128 pp.
ISBN: 978-3-89336-788-7

Band / Volume 142
Herstellung uranbasierter Keramiken mittels interner Gelierung zur Konversion trivalenter Actinoiden
H. Daniels (2012), 154 pp.
ISBN: 978-3-89336-794-8

Band / Volume 143
Experimental and numerical studies on solute transport in unsaturated heterogeneous porous media under evaporation conditions
M. Bechtold (2012), xviii, 131 pp.
ISBN: 978-3-89336-795-5

Band / Volume 144
Konzept und Kosten eines Pipelinesystems zur Versorgung des deutschen Straßenverkehrs mit Wasserstoff
D. Krieg (2012), 228 pp.
ISBN: 978-3-89336-800-6

Band / Volume 145
Mechanistic studies on the OH-initiated atmospheric oxidation of selected aromatic hydrocarbons
S. Nehr (2012), viii, 129 pp.
ISBN: 978-3-89336-804-4

Band / Volume 146
Electron Spin Resonance Investigation of Semiconductor Materials for Application in Thin-Film Silicon Solar Cells
L. Xiao (2012), VIII, 147 pp.
ISBN: 978-3-89336-805-1

Weitere ***Schriften des Verlags im Forschungszentrum Jülich*** unter
http://wwwzb1.fz-juelich.de/verlagextern1/index.asp

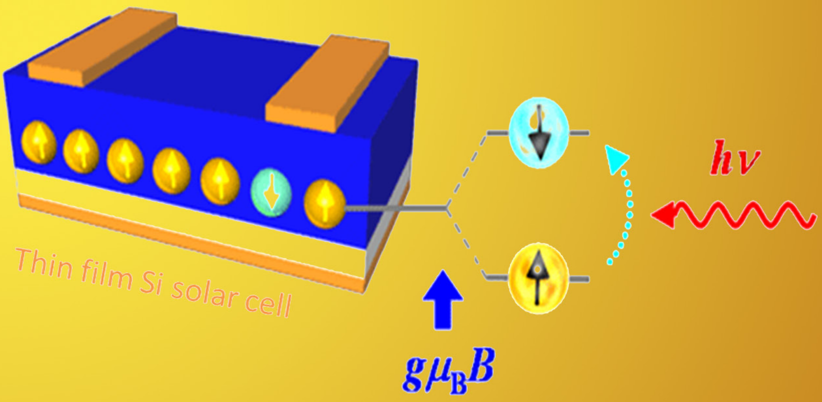

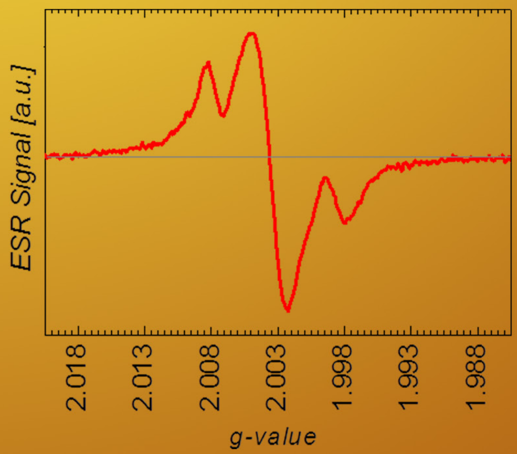

Energie & Umwelt / Energy & Environment
Band / Volume 146
ISBN 978-3-89336-805-1

JÜLICH
FORSCHUNGSZENTRUM